STUDY OF LIVER SURFACE IMAGING MARKER TO MONITOR CHRONIC LIVER DISEASE PROGRESSION

YAN JIE

(B.Eng. SHANGHAI JIAO TONG UNIVERSITY)

A THESIS SUBMITTED

FOR THE DEGREE OF DOCTOR OF PHILOSOPHY

DEPARTMENT OF PHYSIOLOGY

NATIONAL UNIVERSITY OF SINGAPORE

2015

DECLARATION

I hereby declare that this thesis is my original work and it has been written by me in its entirety.

I have duly acknowledged all the sources of information which have been used in the thesis.

This thesis has also not been submitted for any degree in any university previously.

Yan Jie
25 Apr 2015

Acknowledgements

First of all, I would like to give my utmost gratitude to my supervisor Prof. Hanry Yu, who ignored my ignorance and offered me the chance of coming to Singapore. He is a smart, knowledgeable and patient mentor, who has tried his best to not only shape my scientific thinking, but also teach me the philosophy of life. I am deeply motivated by his passion in science and inspired by his boundless ideas. I am also grateful for all the opportunities he has provided for me in the past four years. The four year study in Singapore has been the most rewarding and memorable period in my life that will shape my whole life. It has been a great pleasure to study in his lab because of the great group and working environment that Prof. Yu has put together.

I will also extend my gratitude to my co-supervisor Prof. Peter So. He has given me a lot of guidance especially during my half-year residence at MIT. His scientific expertise stimulated me so much that my project would have been impossible to move forward smoothly without his valuable advice. I enjoyed every discussion with him and will never forget his humor and laughter. Besides, I will thank Singapore-MIT Alliance Research and Technology (SMART) who has provided me with my scholarship and the precious opportunity to do research in both Singapore and MIT. SMART to me is a big family where all members work together to create an atmosphere conducive to scientific discussion. I have learned a lot and enjoyed every gathering with them.

Also importantly, I am grateful to my beloved parents who have constantly given me spiritual support and my husband who has given me a lot of encouragement, especially in my later part of PhD life. Whenever I felt lost,

bored and depressed, his unconditional support gave me the courage to brave out whatever hardship I faced in my studies.

Many thanks to all my colleagues: Mr. Yuzhan Kang and Dr Junjun Fan, who have patiently helped me gained the essential techniques for animal experiments; Dr. Shuangmu Zhuo and Ms Qiwen Peng, who have patiently taught me techniques of optical path adjustment; Dr. Huipeng Li, Dr. Junjie Wang and Dr. Shuoyu Xu, who have kindly instructed me on the skills of imaging processing and statistics analysis. My sincere gratitude is also given to Dr. Lei Xia, Dr. Toh Yi-Chin who has kindly provided scientific input to help me define my PhD qualification exams. Besides, I have been always enjoying my office time with Ms Jiangwa Xing, Ms Wenhao Tong and Ms Qiwen Peng. They are three wonderful optimistic happy Sagittarius girls who can always find a way to dispel vexation. It was so much fun to stay in lab because of them.

Last but not least, my thanks goes to my examine committee members, who will most directly determine if I could finally complete my life as a student. I am grateful not just for their precious time, but also the guidance and suggestions they will provide during my defense.

Table of Contents

Summary

Chronic liver disease, especially non-alcoholic fatty liver disease (NAFLD), is affecting increasing number of people worldwide. However, until today the progression mechanism of chronic liver disease is not yet fully understood. Looking for imaging markers from liver surface is an important step for understanding disease progression mechanism and possibly systematically monitoring chronic liver disease progression in the future. This thesis presents a study of imaging markers from liver surface using different optical microscopic techniques. The hypothesis driving the whole study is that hepatic microcirculation is a meaningful marker for chronic liver disease, and triggers the progression of the disease. Since chronic liver disease is usually composed of complex histological spectra, we isolated two important histological spectra of chronic liver disease, i.e. fibrosis and steatosis, and searched imaging markers from these aspects.

To begin the study, we designed and developed an intra-vital imaging window for live imaging of rodent liver. On this animal investigation platform, we established a quantitative method to characterize the hepatic microvasculature related features during the fibrosis progression and correlated the change of features with the staging of the fibrosis. We discovered that the drastic change of the hepatic microcirculation took place in the early to middle stage of the fibrosis. From the result, we inferred that the microcirculation lesion drove the progression of fibrosis by advancing the changes of the other features such as collagen accumulation.

In the second part of the work presented in this thesis, we kept on looking for structural features of liver surface that related to hepatic fibrosis. Nonlinear

two photon microscope was used to take images from liver surface of both normal rat and fibrotic rat. Five features about the collagen/elastin morphology and redox status of hepatocytes were extracted and quantified. They were found to be related with the fibrotic status.

The third part of this work is devoted to studying the imaging marker of steatosis. We delineated the structural feature changes using the Raman micro-spectroscopy, and recognized the dominant role that fatty acid is playing in disease progression. We envision the integration of all the imaging markers we studied in this thesis and the comparison of the significant onset of structural feature change and the microcirculation feature change to further prove the hypothesis.

Current thesis work is based mainly on the publication 1 and 2 in the list of publications on page iii.

List of Publications

1. **Jie Yan**, Yuzhan Kang, Shuoyu Xu, Lee-Ling S.Ong, Shuangmu Zhuo, Ralph M Bunte, Nanguang Chen, H. Harry Asada, Peter T.C. So, Ian R. Wanless, Hanry Yu. In vivo, label-free quantification of liver microcirculation using dual modality microscopy. *Journal of Biomedical Optics* 2014; 19(11):116006.
2. Shuangmu Zhuo*, **Jie Yan***, Yuzhan Kang, Shuoyu Xu, Qiwen Peng, Peter T.C. So, Hanry Yu. In vivo, label-free, three-dimensional quantitative imaging of liver surface using multiphoton microscopy. *Applied Physics Letter* 2014; 105(2): 023701. (*Shuangmy Zhuo and Jie Yan contribute equally)
3. Wen Hao Tong, **Jie Yan**, Xin Hong, Nisha Hari Singh, Shu Rui Wang, Bramasta Nugraha, Lei Xia, Ciprian Iliescu, Hanry Yu. Perfusion sandwich-constrained hepatocyte spheroid culture. Submitted to *Biomaterials.*
4. Wai Jin Tan, **Jie Yan**, Shuoyu Xu, Aye Aye Thike, Boon Huat Bay, Hanry Yu, Min-Han Tan, Puay Hoon Tan. Second harmonic generation microscopy is a novel technique for differential diagnosis of breast fibroepithelial lesions. *Submitted to Breast Cancer Research.*
5. Stefan Stanciu, Shuoyu Xu, Qiwen Peng, **Jie Yan**, George A. Stanciu, Roy E. Welsch, Peter T. C. So, Gabor Csucs & Hanry Yu. Experimenting Liver Fibrosis Diagnostic by Two Photon Excitation Microscopy and Bag-of-Features Image Classification. *Scientific Report* 2014; 4: 4636.
6. Shuoyu Xu, Chiang Huen Kang, Xiaoli Gou, Qiwen Peng, **Jie Yan**, Shuangmu Zhuo, Chee Leong Cheng, Yuting He, Yuzhan Kang, Wuzheng Xia, Peter So, Roy Welsch, Jagath Rajapakse, Hanry Yu. Quantification of liver fibrosis via surface imaging of the Glisson's capsule. Submitted to *PLoS ONE.*
7. Shuoyu Xu, Yan Wang, Dean C.S. Tai, Shi Wang, Chee Leong Cheng, Qiwen Peng, **Jie Yan**, Yongpeng Chen, Jian Sun, Xieer Liang, Youfu Zhu, Jagath C. Rajapakse, Roy E. Welsch, Peter T.C. So, Aileen Weeemail, Jinlin Houemail, Hanry Yu. qFibrosis: Quantitative Biopsy-based Liver Fibrosis Assessment in Animal Model and Chronic Hepatitis B Patients. *Journal of Hepatology* 2014; 61(2): 260-269.

List of Tables

List of Figures

List of Abbreviations

Acousto-optic modulator	AOM
Area under the curve	AUC
Bile duct ligation	BDL
Biliary epithelial cell	BEC
Coherent anti-Stokes Raman scattering	CARS
Charge-coupled Device	CCD
Collagen proportionate area	CPA
Continuous wave	CW
Extracellular matrix	ECM
Flavo proteins	Fp
Fluorescence-to-signal	F/S
Full width at half maximum	FWHM
Hepatitis B virus	HBV
Hepatocellular carcinoma	HCC
Hepatitis C virus	HCV
Hematoxylin & eosin	H&E
Hepatic stellate cells	HSC
Inhibitor of NF-κB	IκB
IκB kinase	IKK
Insulin resistance	IR
Infrared	IR
Laser speckle contrast imaging	LSCI
Medial axis transform	MAT
Mean free path	MFP
Matrix metalloproteinase	MMP
Magnetic resonance spectroscopy	MRS

Metabolic syndrome	MS
Masson trichrome	MT
Nicotinamide adenine dinucleotide reduced	NADH
Nicotinamide adenine dinucleotide phosphate reduced	NADPH
Non-alcoholic fatty liver disease	NAFLD
Non-alcoholic steatohepatitis	NASH
NF-κB essential modifier	NEMO
Nuclear factor κB	NF-κB
Photomultiplier tube	PMT
Red blood cell	RBC
Residual mean square	RMS
Receiver operating characteristic curve	ROC
Reactive oxygen species	ROS
Second harmonic generation	SHG
Transforming growth factor–β1	TGF-β1
Thrombosponding-1	TSP1
Two-photon excited fluorescence	TPEF

Chapter 1 Introduction

1.1 Motivation

The liver, as the second largest organ of the body, is indispensable to human body because of its synthetic, metabolic and detoxicating functions. Chronic liver disease, including its complications (such as liver cirrhosis and liver cancer), has become the major cause of mortality and morbidity across the world (1, 2). According to the data provided by Centers for Disease Control and Prevention, the death from chronic liver disease and liver cancer accounted for 2.19% of all deaths in USA in the year of 2011. The report published by the European Association for the Study of the Liver in the year 2013, suggests that approximately 29 million people in EU are suffering from the chronic liver disease. Although alcohol consumption, Hepatitis B and C virus are still the leading causes for the cirrhosis and liver cancer, Non-alcoholic fatty liver disease (NAFLD) is becoming the main driver for the increased prevalence of the liver disease due to the increasing incidence of metabolic syndrome (3).

Chronic liver disease, known as a disease procedure involving progressive destruction and regeneration of liver parenchyma, is still not fully understood in terms of its progressing mechanisms. Some researchers agrees to the concept that extracellular matrix (ECM) remodeling is a pivotally important step because it affects both hepatocytes and sinusoidal cell functions (4, 5). Meanwhile, advancing fibrosis, which usually leads to cirrhosis, is the most common risk factor of liver cancer and liver failure. Therefore, the biochemical cascades that are directly or indirectly linked to fibrogenesis, are considered to explain the mechanism of chronic liver disease. Specifically, the

fibrogenesis involves mainly the activation of Hepatic stellate cells (HSC) and myofibroblast meditated by transforming growth factor–β1 (TGF-β1) and other mediators (6). The pathogenesis of fibrosis will be reviewed in the next chapter.

However, we believe that chronic liver disease is closely associated with hepatic vascular lesion. Liver is unique in dual blood perfusion with both portal vein and hepatic artery receiving cardiac output (7). The inflow blood from inferent vessels flows through sinusoids, where the metabolic exchange with hepatic cells is performed, and then exit the liver through the hepatic vein. This structure forms the macrocirculation and microcirculation of the liver. In macro-perspective, the hepatic vascular lesion leads to the imbalance between the blood inflow and outflow. The imbalance deprives the parenchymal cells of proper perfusion by microcirculation and thus leads to atrophy of hepatic cells and parenchymal extinction. Because parenchymal extinction would deform the microvasculature and aggravate the underperfusion of hepatic cells, a positive feedback loop is formed (8, 9) to trigger the progressing of chronic liver disease. Besides, microcirculation of the liver is responsible for transporting hormones and released cytokines. Our group's previous discovery of switch-like bi-stable transition between two levels of active TGF-β1, resulting from the competition between thrombospondin-1 (TSP1) meditated activation and Plasmin meditated activation (10), also suggests the importance of blood circulation in spatial distribution of regulators in ECM production.

Based on the findings above, we therefore propose a hypothesis that the hepatic microcirculation is a meaningful marker for progression of chronic liver disease and triggers the disease progression. This hypothesis drives the whole thesis study about imaging marker of chronic liver disease. Since

chronic liver disease usually encompasses of multiple histological spectra, in this study, we focus on three most common spectra: fibrosis and steatosis.

1.2 Objective and specific aims

The whole study is composed of three parts. Each part focuses on different imaging markers. These parts form the three specific aims in this thesis. Each aim solves a single scientific problem and constitutes a single chapter in this thesis.

1.2.1 Specific Aim 1: To characterize hepatic microcirculation, and correlate the feature changes of hepatic microcirculation with the liver fibrosis progression

Hypothesis: hepatic microcirculation is a meaningful marker of chronic liver disease, the changes of the microcirculation are correlated with the progression of fibrosis.

Studies have proved that hepatic venous pressure gradient (HVPG) has a good correlation with the degree of cirrhosis (11). This indicates a relationship between hemodynamic features and fibrosis. However, the measurement of HVPG is rather invasive and inconvenient to practice. Besides, it takes only the pressure gradient as a proxy for hepatic microcirculation. Whether the morphological vasculature and dynamic speed of the hepatic microcirculation correlate to the hepatic disease progression is not known. Therefore, the study is refined to focusing on the relationship between the microcirculation features and the progression of fibrosis to answer the question if the fibrosis progression and the change of these features are correlated.

In order to achieve the extraction of both morphological features and dynamic features of the hepatic microcirculation, current techniques include in vivo fluorescence microscopy (12, 13), laser Doppler flowmetry (14), near-infrared spectroscopy (15, 16) and orthogonal polarized spectral imaging (17). However these methods are limited either by spatial-temporal resolution or by involvement of exogenous contrast agent, which affects liver's function. Thus in this study, we implement an intra-vital microscopic system that combines wide-field fluorescence microscope and laser speckle contrast imaging (LSCI) technique. With our designed intra-vital imaging window, large volumes of in vivo images are acquired. Then a computer-based imaging processing method is explored for feature recognition and extraction. By using the histopathological score as the ground truth of progression of the fibrosis, the correlation between the quantified features and the staging of disease is analyzed. We find that the changes of the hepatic microcirculation take place in the early to middle stage of disease progression.

1.2.2 **Specific Aim 2: To explore liver surface structural features that relate to liver fibrosis**

Hypothesis: structural features from the liver surface, including the surface ECM and redox status of hepatocytes, are important imaging markers to indicate the fibrosis status.

In this section, we describe the acquisition of detailed structural and functional information from liver surface at cellular and sub-cellular level using nonlinear two photon microscopy. The nonlinear microscopy with intrinsic two-photon fluorescence (TPEF) and second harmonic generation (SHG) has its advantage in the study of liver in vivo. Firstly, it has deeper imaging penetration and less photobleaching compared to confocal microscope.

Secondly, TPEF/SHG microscopy has been exploited for qualitative and quantitative assessment of liver's histopathology features (18) because of its ability to visualize collagen and hepatocytes.

Applying TPEF/SHG microscopy to in vivo liver study enables us to visualize the intrinsic components such as reduced pyridine nucleotide (NADPH), flavins and collagen type I&III. In this part of study, we use three detection channels (i.e. 390-410nm, 430-490nm, 500-560nm) to collect the signal of liver of live animal. The images from both capsular and subcapsular layers are compared and analyzed quantitatively. Five features are defined that have significant difference between normal and fibrotic animal. These features are useful imaging markers of liver fibrosis.

1.2.3 **Specific Aim 3: To delineate structural and biochemical features that relate to hepatic steatosis**

Hypothesis: the structural and biochemical feature changes during the progression of steatosis can be studied by Raman micro-spectroscopy.

The steatosis is the main histological spectrum of non-alcoholic fatty liver disease (NAFLD). While NAFLD has become the main driver for the increased prevalence of chronic liver disease worldwide, more and more studies have focused on the progression of NAFLD. Yet the mechanism of the progression of NAFLD is not fully understood. In this part, the structural and biochemical feature changes during the NAFLD progression is studied using Raman micro-spectroscopy. The dominant role of fatty acid accumulation during the NAFLD progression is demonstrated. This study helps us better understand the disease progression mechanism.

1.3 Outline of the whole thesis

This thesis contains six chapters. The introduction part in the Chapter 1 briefly describes the motivation and the objectives of the whole thesis study. In Chapter 2, we review the background of the study. It starts with the pathogenesis of hepatic fibrosis and NAFLD, followed by a brief review of the diagnostic methods of liver disease. Thereafter, the optical microscopic techniques used in this thesis, specifically laser speckle contrast techniques, non-linear two photon microscope and Raman spectroscope, are reviewed in terms of the basic principle and application in bio-imaging. Chapter 3 begins with the design and development of liver imaging window of rodents and describes the establishment and verification of the method for liver surface microcirculation study. In Chapter 4, we explore the surface structural features of liver using nonlinear two-photon microscope. In Chapter 5, we delineate the structural and biochemical features during the steatosis progression using Raman spectroscope. Finally, in Chapter 6, we conclude all the major findings of the studies and the implications.

Chapter 2 Background and Significance

In this chapter, we introduce the background information that supports the rationale of the work presented in this thesis. Section 2.1 is a brief review of chronic liver disease including liver fibrosis and non-alcoholic fatty liver disease (NAFLD), and their pathogenesis. The clinical diagnostic method is also briefly reviewed at the end. Section 2.2 is about features of liver surface that could potentially be imaging markers to monitor chronic liver disease. Section 2.3 gives a brief review about different optical microscopic techniques used in this thesis.

2.1 Pathogenesis and diagnosis of chronic liver disease

2.1.1 Liver—anatomy and physiology

Liver is the second largest organs in body. This vital organ has a wide range of functions. In terms of metabolism, liver is functioning by storing glycogen, red blood cells decomposition, synthesizing plasma protein, producing hormone and detoxificating. Besides, it produces bile, an alkaline compound that aids in digestion. It also regulates a large variety of biochemical reactions, including the synthesis and breakdown of small and complex molecules. The function of liver is irreplaceable for a living body, clinically there is no way to compensate for the absence of liver function in the long term (19).

In terms of anatomy, liver has a reddish brown color. The mass is divided in to lobes, while the number and size varies with species. For human beings, the liver contains four lobes with unequal size and shape. The liver usually lies to the right of the stomach and over the gallbladder (rat does not has gallbladder). The typical drawing of a rat liver that contains typical four lobes (Middle lobe,

Left lateral lobe, Right lateral lobe and Caudate lobe) is shown blow (Figure 2-1).

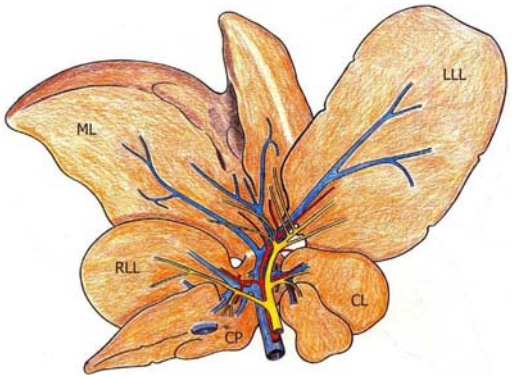

Figure 2-1. The anatomy of rat liver, the drawing shows multiple liver lobes and the drainage system of the liver. The drainage system includes portal vein (blue), hepatic artery (red) and biliary duct (yellow). ML: Middle lobe; LLL: Left lateral lobe; RLL: Right lateral lobe; CL: Caudate lobe; CP: Caudate process. Source: Image adapted from published literature (20).

Liver is covered by a thin sheet of connective capsule that extends throughout the substance of the liver. The connective tissue tree provides support scaffolding and helps the blood vessels, lymphatic vessels and the bile ducts to traverse the liver. Liver is composed of small units called lobules (Figure 2-2), which is the unit structure of the liver. Most livers have between 50,000 and 100,000 lobules. Each lobule has a hexagonal shape, the arrangement of hepatocytes radiates outward from a central vein in the center, with portal tracts distributed at the vertices of the lobule (21). Liver cells grouped into sheets or bundles surrounded by sinusoids. Sinusoid acts as caterpillar in liver and gives liver the ability to hold large amount of blood. This structure also eases the metabolic exchange between the blood and the liver mass.

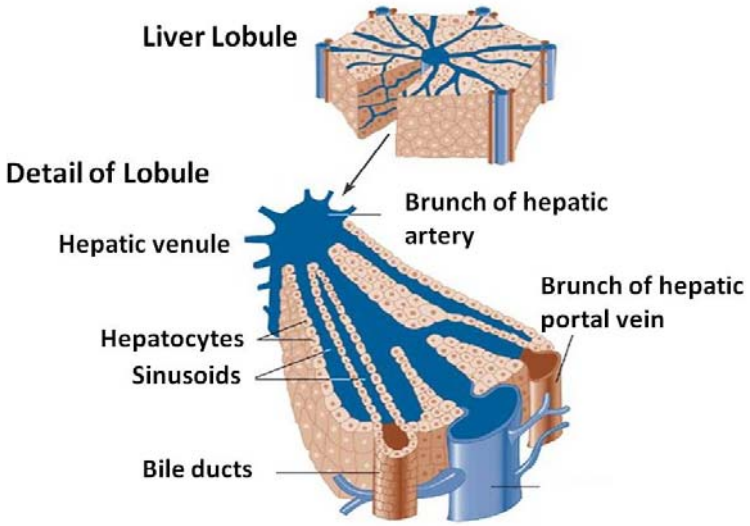

Figure 2-2. The microanatomy structure of liver. The liver is composed of hexagonal microstructures called liver lobule. Liver cells is grouped into sheets and groups surrounded by sinusoids. Source: image adapted from published literature (22)

2.1.2 **Hepatic fibrosis and cirrhosis**

Liver fibrosis is a wound-healing process in response to chronic liver injuries (23). This process involves mainly the accumulation of scar tissue that consists of extracellular matrix (ECM) components. This is a significant characteristic of most types of chronic liver disease, such as chronic Hepatitis C virus (HCV) infection, alcohol abuse, and nonalcoholic steatohepatitis (NASH). The accumulation of ECM will distort the hepatic architecture, which is a prominent sign for pathologist to diagnose fibrosis. The subsequent development of fibrosis and the presence of nodules of regenerating hepatocytes define the cirrhosis. Cirrhosis is commonly featured by cellular dysfunction and increased intrahepatic resistance to blood flow (6, 24).

The progression of fibrosis is usually insidious. In most cases, the morbidity and mortality occur well after certain complication has developed, while it is already the late stage of fibrosis (i.e. cirrhosis). The progression of fibrosis can occurs as slow as many years, but under certain clinical settings, such as

repeated episodes of acute alcoholic hepatitis, fulminant hepatitis and fibrotic cholestasis with HCV re-infection after liver transplantation (25), fibrosis can advance rapidly. Clinical complications of advancing fibrosis include ascites, renal failure and variceal bleeding. Fibrosis patients experiencing the end-stage cirrhosis (also called decompensated cirrhosis) can expect a short survival except when liver transplantation is conducted (26). Patients have a much higher risk of developing hepatocellular carcinoma (27), and the survival rate is worsen due to the increasing dropout rate while waiting for donor (28). Because of these reasons, Cirrhosis and hepatocellular carcinoma is among the top ten causes of death worldwide.

Unlike other tissue, liver has remarkable regenerative ability. Once acute liver injury occurs, liver is able to regenerate and replace the necrotic and apoptotic cells. This process is usually initiated by inflammation, but inflammatory response comes along with the deposition of ECM. If the hepatic injury persists, the liver's regeneration eventually fail to catch the speed of ECM accumulation, the hepatocytes are finally substituted by the ECM, and collagen predominated fibrillar scare is formed. The distribution of such fibrous material is dependent on the location and the onset of the liver injury. For example, ECM is vastly located around portal tracts if the injury is resulted from virus infection and cholestatic disorder; fibrotic tissue is largely presented in paricentral and perisinusoidal area if the liver disease is induced by alcohol or drug (29).

The activated Hepatic Stellate cells (HSC) are believed to be the main producer of ECM (30). In normal liver, hepatic stellate cells reside in the space of Disse, and function as the major storage sites of vitamin A in liver. Upon injury, HSCs undergo a series of morphological and functional changes, and

they are activated and transformed into smooth muscle a–actin positive myofibroblast-like cells (i.e. activated HSC). At the same time, it acquires contractile, proinflammatory, fibrogenic properties, and loses the vitamin A storage function (31). The activated HSCs migrate and aggregate to the proinflammatory sites, where both collagenous and non-collagenous ECM proteins are secreted. The degradation of the ECM is also controlled by activated HSCs, which is particularly important for the reverse of liver fibrosis. Other than HSC, myofibroblast is another important cell type with fibrogenic potential. Myofibroblasts initiate from small vessels around portal region. Its proliferation is stimulated by apoptotic hepatocytes (32). Both myofibroblasts and HSCs are fibrogenic when stimulated, but HSCs action mainly in pericentral region, myofibroblasts dominates the portal region.

The complex interplay among hepatic cells is illustrated in the following diagram (Figure 2-3). The primary injuries, such as hepatitis virus, alcohol and fat metabolites firstly target different hepatic cells (mostly hepatocytes) and induce their release of Reactive oxygen species (ROS) and different kinds of inflammatory cytokines. The inflammatory response is therefore initiated. The inflammatory cells then stimulate the activation and proliferation of HSCs. Meanwhile, the apoptosis of damaged hepatocytes activate myofibroblasts. Both HSCs and myofibroblasts migrate to damaged location and secret fibril collagen. But the story is much complicated because both of them could secret inflammatory chemokines and control the activity of lymphocytes if the injury is persisted. This results in the formation of a vicious circle that both inflammation and fibrogenesis stimulate each other to occur (33). The circle could go on and on, until the liver is doomed.

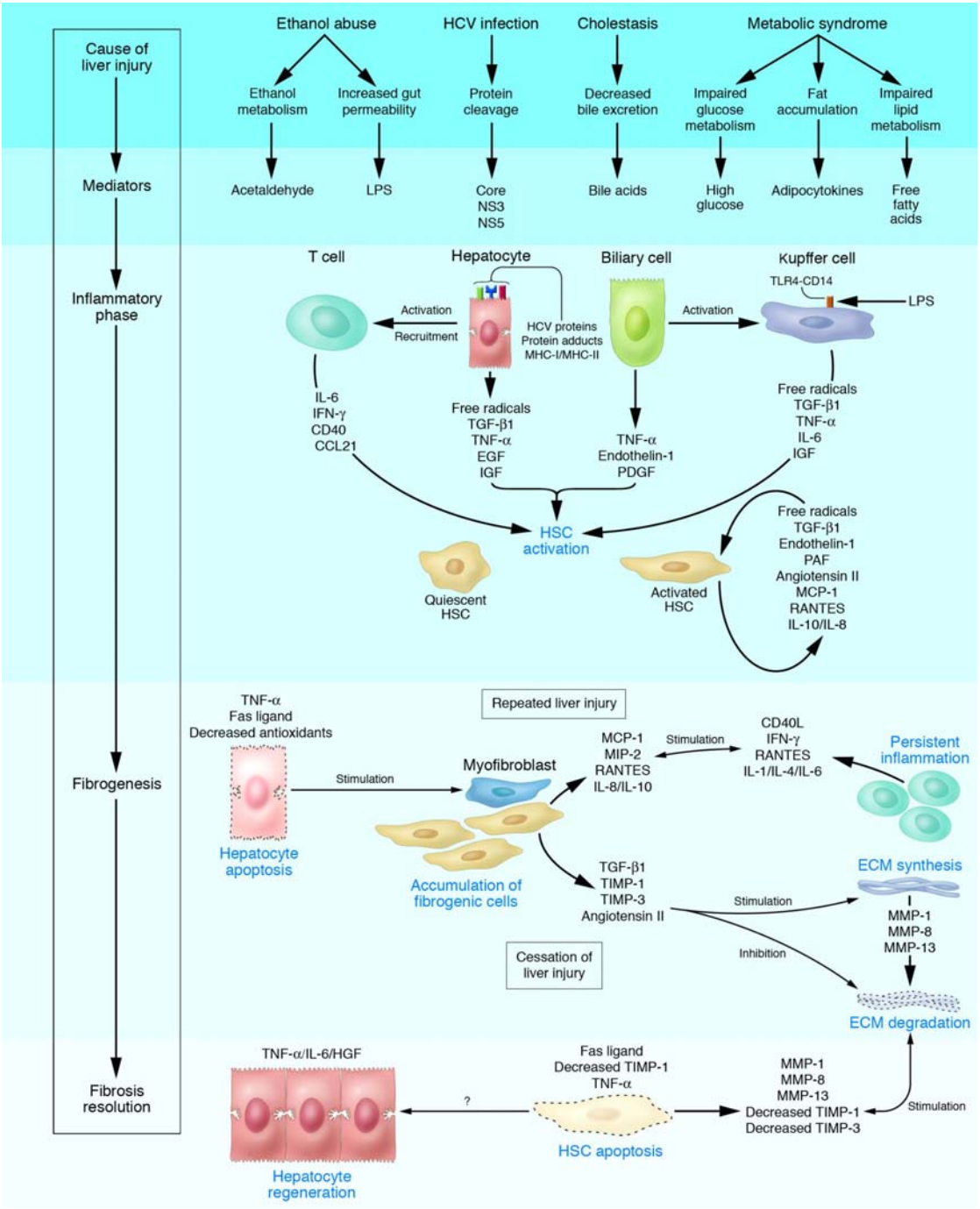

Figure 2-3. Mechanisms of liver fibrosis. The primary hepatotoxic agents induce inflammatory response among hepatic cells through the production of mediators. Damaged hepatic cells (hepatocytes and biliary cells) release ROS and inflammatory cytokines to activate the Kupffer cells and T cells. The inflammatory cells activated the HSCs and other type of myofibroblasts. Activated HSCs secrete cytokines so that

to retain the activated status, and to control the activity of the inflammatory cells. In the mean time they secret large amount of fibril collagen (ECM) at the damaged location to replace the apoptotic hepatic cells. If the injury persist, this circle goes on and on till cirrhosis and liver failure. But once the injury ceased, the degradation of ECM surpasses the synthesis of ECM, this explains the reversibility of fibrosis. The degradation of collagen is induced by the increased activity of matrix metalloproteinases (MMPs) and decreased expression of tissue inhibitor of metalloproteinases (TIMPs). The reversal of fibrosis also involves the apoptosis of activated HSCs and regeneration of hepatocytes. CCL21, C-C chemokine ligand 21; MCP-1, monocyte chemoattractant protein–1; MIP-2, macrophage inflammatory protein–2; NS3, HCV nonstructural protein 3; NS5, HCV nonstructural protein 5; PAF, platelet-activating factor. Source: image adapted from published literature (6)

The premise of forming the vicious circle is persistent injury, but what if the injury is suspended? This brings our attention to the most controversial issue regarding liver fibrosis: is liver fibrosis reversible? The reversibility issue of liver fibrosis is under the spot light in the recent decade (34-36). Since right now the only effective treatment for end stage cirrhosis is liver transplantation, but in most society, the availability of donor organ has limited the applicability of this treatment. Therefore, the possibility of regression of fibrosis has become the kernel for developing antifibrotic therapies.

Recent evidence indicates that even advanced fibrosis is reversible, both on experimentally induced fibrosis of animal models (37) and on human patients (38-41), even though the regression usually takes very long term with the condition of withdrawn liver insult. The mechanism of fibrosis regression has been extensively discussed in previous literature (37). The family of matrix metalloproteinases (MMP), expressed by activated HSCs and Kupffer cells, has been believed to have the ability to degrade collagen (type I and III) (42). Evidence also indicates that decreased expression of tissue inhibitors of metalloproteinases (TIMPs) (43) and the apoptosis of activated HSC (44) also

take roles in inhibiting collagenase and stimulating ECM degradation (Figure 2-3).

2.1.3 **NAFLD and NAFLD derived hepatocellular carcinoma**

Non-alcoholic fatty liver disease (NAFLD) is becoming the main driver for the increased prevalence of the liver disease due to the increasing incidence of metabolic syndrome (45). The pathology of NAFLD resembles alcohol-induced liver disease, but involves no alcohol abuse. The most obvious hallmark is the accumulation of the triglycerides within hepatocytes, and thus characterized by central obesity and metabolic syndrome (MS). It is also characterized by insulin resistance (IR), which is a physiological condition that cells fail to respond to the normal secretion of hormone insulin. Therefore，NAFLD could result in type II diabetes. Besides, NAFLD is a risk factor to Hepatocellular Carcinoma (HCC), among the patients with NAFLD, around 30% of the population will develop NASH, which is a more serious level of liver damage, and around 20% of the patients with NASH eventually develop cirrhosis and liver cancer.

Because NAFLD is a completed process that encompasses MS, NASH, necroinflamation and advancing fibrosis, it is unclear which contributes the most to the final development of HCC, the underlying mechanism among them is not well understood. Previous studies hold that cirrhosis is a main risk factor for hepatocellular carcinoma, therefore HCC can be regarded as a complication of end-stage NAFLD, just like other chronic fibrotic liver disease. However more and more evidence (46) indicates that hepatocarcinogenesis may be related to early stage of NAFLD so that MS might be the real risk factor to HCC (47, 48). Even though patients with NAFLD and cirrhosis have the highest risk of developing HCC, patients with

NAFLD but without cirrhosis can also develop HCC (49). HCC has been discovered in patients with simple steatosis, which is neither NASH nor fibrosis (50, 51).

Besides NAFLD, metabolic factors such as obesity and type II diabetes are also associated with HCC. Obesity is a problem that attracts enough attention in recent decades. Research has shown that obesity increased the risk of many cancers especially liver cancer (47). Obesity specifically increases the risk of HCC in populations that are already at high risk of HCC, for example with cirrhosis (52) and Hepatitis B (53) or Hepatitis C (54). Diabetes mellitus, mainly type II, has also been identified as an independent risk factor for HCC (55, 56). Diabetes also potentiate the obesity associated risk of HCC (57). Therefore, treating NAFLD with insulin-sensitizing drugs improves steatosis and inflammation, resulting in a reduced risk of liver cancer (58).

NAFLD is inflammatory dominant disease, and the occurrence of inflammation has a close relationship with the fat accumulation. The nuclear factor κB (NF-κB) family of transcription factors are the main regulator for inflammatory responses (59). In the inactive state, NF-κB proteins are suppressed by inhibitor of NF-κB (IκB). IκB kinase (IKK) complex can phosphorylate the IκB and target IκB for degradation, thus permitting nuclear localization of NF-κB proteins and altering transcription of genes regulated by NF-κB. The IKK complex includes two subunits, one is IKK-α and IKK-β, the other is NF-κB essential modifier (NEMO) (60). Deregulated activation of NF-κB has important effect on the development of NASH, IR, inflammation, fibrosis and cancer (61, 62) . The pathways involved in NAFLD- meditated carcinogenesis is illustrated in Figure 2-4.

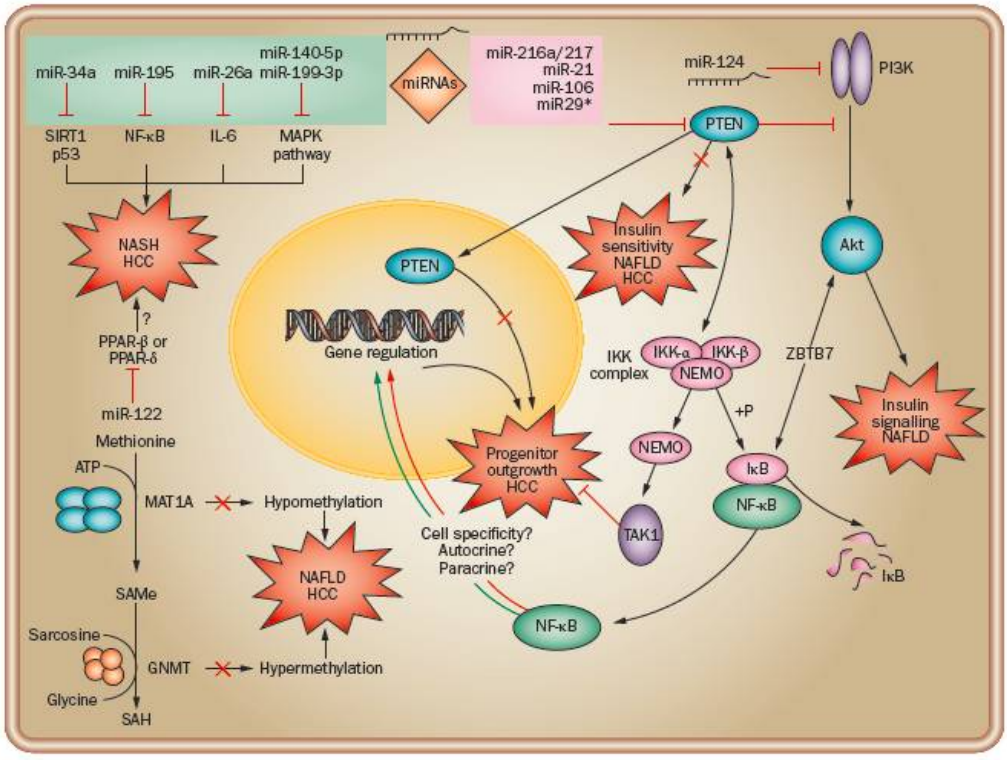

Figure 2-4. Overview of the pathway that involves in NAFLD related hepatocarcinogenesis. Inside the pink box, there are onco-MicroRNAs (oncoMiRs) that ablate expression of tumor suppressor. Inside the green box, there are tumor suppressor miRs. Black arrow indicates the activation of downstream signaling. Red blunted lines indicates inhibition, bidirectional arrows indicate crosstalk between signaling molecules. The red '×' indicates the abrogation of signaling of specific molecules. Figure is adapted from reference (63)

2.1.4 **Clinical methodology of diagnosis**

The development of chronic liver disease is always insidious in the early stage, early detection and treatment is almost impossible. Therefore, diagnosis of chronic liver disease is to decide if the disease is progressing and forecast how fast it is progressing to the end stage. Currently, liver biopsy and histological examination is still the gold-standard method to diagnose liver disease, which is trusted by most doctors. The H&E or other specific stained tissue is investigated by experienced histologist to identify the cause of the disease and to assess the stage of disease. Taking fibrosis for example, diagnosis is based on the scoring or staging according to the standard of Metavir score (0-4) (64)

or Ishak score (0-6) (65) (Table 2-1). The limitation of liver biopsy is its invasive nature and less representativeness of the obtained tissue. There is a report that 40% of patients experienced pain and 0.5% of patients went through complications come with liver biopsy (66). Besides, the biopsy tissue, with the area of 30-50 $mm^{2,}$ is trivial and incurs sampling error. The literature has suggested that cirrhosis is misdiagnosed on single liver biopsy in 10%-30% of the cases (67).

Table 2-1. Scoring systems of liver fibrosis. The Ishak system has 6 grades; the Metavir system has 4 grades.

Categorical description	**Ishak stage**	**Metavir score**
No fibrosis (normal)	0	0
Fibrous expansion of some portal areas ± short fibrous septa	1	1
Fibrous expansion of most portal areas ± short fibrous septa	2	2
Fibrous expansion of most portal areas with occasional portal to portal (P-P) bridging	3	
Fibrous expansion of portal areas with marked bridging portal to portal as well as portal to central (P-C) bridging	4	3
Marked bridging (P-P and/or P-C), with occasional nodules (incomplete cirrhosis)	5	
Cirrhosis, probable or definite	6	4

Besides liver biopsy, other non-invasive complementary diagnose method has been emerging. Broadly speaking, they can be divided to biological approach, including serum markers and metabolic test, and physical approach, including bioimaging based on ultrasound, MRI and elastrography. The advantage and disadvantage of the liver disease diagnosing method is listed in Table 2-2.

Table 2-2. The advantages and disadvantages of both invasive and non-invasive approaches for liver disease diagnosis.

<table>
<tr><th></th><th colspan="2">Non-invasive</th><th>invasive</th></tr>
<tr><td></td><td>Biological approach (e.g.Serum marker)</td><td>Physical approach (e.g MRI, elastography)</td><td>Surgical approach (Liver biopsy)</td></tr>
<tr><td>Advantages</td><td colspan="2">•Non-invasive, no pain, no risk;
•High applicability, reproducible; performed in outpatient clinic;
•Combine with other diagnose to increase accuracy.</td><td>•Assessment of architectural disturbance;
•Direct measure with well established staging system.</td></tr>
<tr><td rowspan="2">Disadvantages</td><td colspan="2">•Unable to determine intermediate stage;</td><td rowspan="2">•Invasive, painful;
•Difficult to repeat;
•Potential life threatening complications (0.03%);
•Sampling and interobserver variability.</td></tr>
<tr><td>•Surrogates not specific to liver.</td><td>•15% Unreliable results (obesity, ascites);
•False positive (acute hepatitis, congestive heart failure).</td></tr>
</table>

Protein serum can be used to decide liver disease status (68). However, the liver disease-specific markers in the blood may reflect disease in organs other than liver. Therefore, unless ideal features of liver disease markers are met, biomarkers remain questionable in detecting liver disease. The criteria include liver specific (independent of metabolic alterations of other organ); be sensitive to discriminate different stages of disease; be able to correlate with dynamic changes in disease progression and be able to predict clinical outcomes including liver failure (69). To date, no biomarker has been really fit these criteria well. Besides biomarkers, other non-invasive diagnostic tools are also applied to clinical scenario. For example, the diagnosis of liver fibrosis can be achieved using ultrasonographic and tomographic technique. Transient elastography (FibroScan) is assessing liver fibrosis by measuring liver stiffness (70) and it has great potential to detect fibrosis non-invasively (71), but it does not provide tissue and cellular level information (72), on which major histological diagnoses count. On the other hand, magnetic resonance spectroscopy (MRS) has gained great focus on its potential of detecting

fibrosis, but it needs to be confirmed in larger studies with standardized methods (73). In the long run, the reliable non-invasive or minimum-invasive markers and diagnosis of liver disease should have remarkable impact on clinical trials and would benefit patients with chronic liver disease.

2.2 Imaging features of liver surface

Looking for imaging features from the liver surface is meaningful for study of liver disease mechanism, and it is also useful for drug screening using animal model. When using imaging technique to study liver, the compromise between resolution and the penetration depth has to be considered. The application of optical microscope in biological study, especially in vivo tissue imaging, is largely limited by its penetration depth. Because the penetration limit is largely depend on the mean free path (MFP) of a photon. MFP is a parameter that describes the average distance a photon travels between two consecutive elastic scattering events. The elastic scattering is resulted from the interaction between the photon and cellular structures (74). The MFP is usually of the order of 100um, varies with the tissue type. Usually the scattering is more minimized in near-infrared spectrum than in visible and ultraviolet spectrum. Since the investigation performed by optical microscope is quite superficial, in this section we therefore focus on the liver surface. We believe components within the liver surface are of structural and functional significance, because it provides key information about the physiology of the liver. However, since the histo-pathological features that are used in routine staging systems (METAVIR and Ishak) are mostly derived from the cellular and tissue structures in the interior liver and cannot be observed from the liver surface using optical microscopic techniques, the correlation between the changes of liver surface features and the liver disease progression requires validation.

2.2.1 **Extracellular matrix**

The progression of fibrosis is featured by the alteration of both the quantity and the composition of the ECM. Its quantity change could be as conspicuous as 6 times in fibrotic liver more than in normal liver, including collagens (type I, III, and IV), fibronectin, undulin and elastin. Therefore it has been an important marker for fibrosis diagnosis. Besides ECM that distributed among the liver parenchyma, liver surface is covered by a 10 μm collagenous layer called the Glisson's capsule (75). The thickness of the Glisson's capsule has been reported to increase to 17-46 um during fibrosis progression (76) as imaged from the biopsied liver tissue sections. Besides, our previous finding has demonstrated that collagen proportionate area (CPA) in liver sub-capsule region, which is beneath the Glisson's capsule but is still detectable by optical microscope, are consistent with CPA measured from interior liver and are well-correlated with fibrosis stages (77). Therefore, ECM investigated from the liver surface could be a marker of liver disease.

2.2.2 **Autofluorescence of endogenous fluorophores**

The autofluorescence of the hepatic cells could also be an intrinsic marker to discriminating normal and diseased status, because autofluorescence properties are closely related to the metabolic status of the hepatic cells (78). The endogenous fluorophores inside liver include NAD(P)H, flavins, vitamin A and fatty acid. Their optimal excitation wavelength and emission peak center wavelength of these endogenous fluorophores are listed in Table 2-3. The NAD(P)H/flavins, NAD^+/NADH and $NADP^+$/NADPH are common redox couples, the value of the ratio indicates the cellular redox state. Therefore they are markers of the energy production and intermediary metabolic status of the hepatocytes. Vitamin A is an antioxidant; it is stored inside Hepatic stellate cell (HSC) of liver. In fact, HSC stores 80% of Vitamin

A of the whole body as retinyl palmitate (79). HSC plays an important role in liver regeneration and lose the storage of vitamin A when it is activated. Therefore the detection of vitamin A is important in deciding if the liver is injured.

Table 2-3. The optimal excitation wavelength and emission peak center wavelength of endogenous fluorophores of liver

Endogenous fluorophores	Optimal excitation wavelength (nm)	Emission peak center wavelength (nm)
$NAD(P)H_{free}$	366	463
$NAD(P)H_{bound}$	366	444
Flavins	488	526
Vitamin A	366	488
Fatty acid	366	470
lipopigments	488	587

2.2.3 **Hepatic surface microcirculation**

The liver has its unique blood perfusion system: it receives 25% of the cardiac output via two inflows, the portal vein and hepatic artery. Both vessels enter the liver at its hilus accompanied by the hepatic bile ducts, lymphatics and nerves. 75-80% of the total inflow is contributed by the capillary system of the intestine, spleen, pancreas and gallbladder via portal vein, the rest 20-25% is delivered through the hepatic artery (7). The total hepatic perfusion amounts to ~1ml.min^{-1}.g $tissue^{-1}$ and the total oxygen consumption accounts for 20% of total body consumption (80). The dual blood supply of the liver distinctly determines the regulation and the distribution of blood flow.

The hepatic microvascular bed, particularly the terminal distribution of the blood vessels and the sinusoids are as follows. In the portal tracts, branches of the hepatic artery, the hepatic portal vein, the main bile duct and the main lymphatic vessels travel parallel to each other through the liver parenchyma (81). After repeated branching, the terminal vessels transfer the blood to the hepatic sinusoids (Figure 2-5). The hepatic sinusoids correspond to the capillary bed of the liver and represent the segment of the microcirculation where supplying of nutrients and removal of metabolic products take place. The sinusoids diameters increase from 7um in the periportal to 15 um in the pericentral area, with length of ~250um. The endothelial cells that constitute the sinusoids have a special structure called ‘sieve plate’, it is open fenestrations ranged in clusters of 10-50 pores with a diameter of 150-175nm (82). Sieve plate acts as a selective sieving barrier to control the extensive exchange of material between the blood and the liver cells. After flowing through the sinusoids, blood passes through outlet, several of such terminal central veins may combine, increasing in diameter and reaching the sub-lobular vein and hepatic vein. They leave the liver on the dorsal surface and extend to the extrahepatic inferior vena cava.

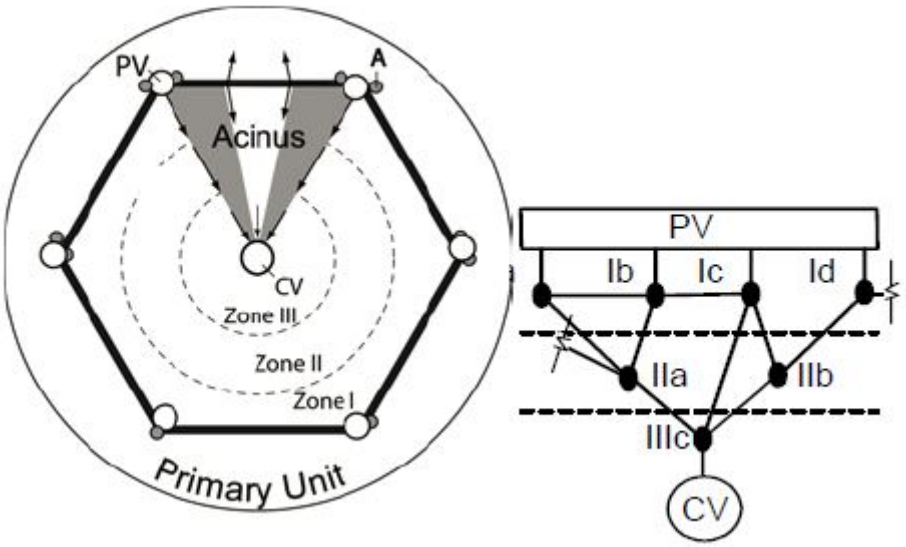

Figure 2-5. The primary vascular system of liver lobule is composed of portal vein-PV, the central vein-CV and the artery-A. After repeated branching, the portal vein and artery (zone I) is divided to small sinusoids (Zone II), nutrition/oxygen supply and metabolic exchange occur in sinusoids. Sinusoids combine together and converge to central vein (zone III).

Hepatic vascular disorder is widely acknowledged as a symptom of chronic liver disease. Even though the vascular lesion is commonly regarded as secondary to primary injury (such as alcohol abuse, HCV infection and toxic exposure), it is detrimental to hepatocytes by relating to provision of nutrients and oxygen, which is the main function of hepatic microcirculation system. In previous research, the importance of microcirculation lesion has been identified in the progression model of chronic liver disease, including Nonalcoholic Steatohepatitis (NASH) and alcoholic fatty liver (8, 83).

Once the vascular disorder has been presented, the ischemic injury will result in focal collapse of the tissue; when focal collapse accumulates to widespread parenchymal extinction, portal tract becomes more close to the adjacent hepatic vein. This change offers the opportunity for the artery in the portal tract to drain directly into the collapsed perivenous tissue, this is called the

arterivenous shunt (84, 85). The shunt formation induces the generation of high-flow and high-pressure conduit between artery and vein. Together with the bridging fibrous septa between portal tracts and terminal veins, the newly formed vascular channel effectively bypasses the parenchymal nodules, and leaves the parenchymal tissue bereft of blood flow. The underperfusion of the liver parenchyma in turn contributes to more advanced parenchymal extinction, thus a positive feedback is formed to impel the disease progression.

2.3 Imaging modality for liver surface imaging

2.3.1 Laser speckle contrast imaging

First introduced in the 1980s, laser speckle contrast imaging becomes a powerful tool for imaging blood flow. It especially gained much attention in recent year because of the application in brain blood flow study (86-88). Laser speckle arises from the random interference pattern when coherent light is scattered by a random medium. The moving scattering particles inside the random medium cause the time-varying phase shift and change the random interference pattern, thus the fluctuation of the speckle pattern is produced. When recording the fluctuation with the camera, the intensity variation shows up at the photodetector. Using temporal and spatial statistics to analyze the intensity variation could yield information about the motion of the scattering particles. Practically, when applying this technique to blood flow study, the increased blood flow speed will cause the intensity of the speckle pattern to fluctuate more rapidly, thus when recording within the CCD integral time (usually 1 to 20 ms), the speckle becomes much blurred in the corresponding area. Therefore, by acquiring the image of the speckle pattern and quantifying the blurring of the speckle, the spatial blood flow map could be obtained. To quantify the blurring, the speckle contrast is defined as the ratio of the standard deviation to the mean intensity:

$$K_{s,t} = \frac{\sigma_{s,t}}{<I>} \quad (1)$$

Here the K_s refers to the spatial speckle contrast, K_t refers to the temporal speckle contrast, σ_s indicates the spatial standard deviation of the speckle intensity, σ_t indicates the temporal standard deviation of the speckle intensity.

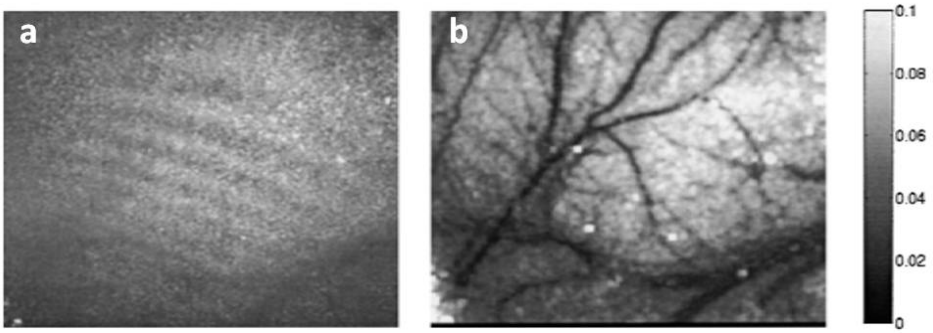

Figure 2-6. (a) Raw speckle image from rat's thinned skull, the grainy pattern is showed. (b). the corresponding spatial contrast image computed using a 5×5 window. Figure adapted from reference (86).

Figure 2-6 shows the representative raw image and the corresponding computed contrast flow map of the rat cortical surface. In theory, the speckle contrast has the value between 0 and 1. A speckle contrast of 1 indicates no blurring of the speckle pattern and thus no motion of the particles. A speckle contrast of 0 indicates that the speckle is blurred because the particles are moving fast enough. The speckle contrast is a function of the integral time *T* of the camera and is related to the autocovariance of the intensity fluctuation of a single speckle $C_t(\tau)$ by (89)

$$K^2 = \frac{\sigma_s^2(T)}{<I>^2} = \frac{1}{T<I>^2}\int_0^T C_t(\tau)d\tau. \quad (2)$$

The corrected formulation proposed recently is wrote as (90)

$$K^2 = \frac{\sigma_s^2(T)}{<I>^2} = \frac{1}{T^2<I>^2}\iint_0^T C_t(\tau-\tau')d\tau d\tau' = \frac{2}{T<I>^2}\int_0^T (1-\frac{\tau}{T})C_t(\tau)d\tau. \quad (3)$$

The autocovariance is defined as

$$C(\tau) =< [I(t) -< I >_t][I(t+\tau) -< I >_t] >, \quad (4)$$

Where $<X>_t$ indicates quantity averaged by time. According to dynamic light scattering theory, the intensity temporal autocorrelation and the autocovariance can also be expressed as (91)

$$\frac{C_t(\tau)}{<I>_t^2} = \beta \left| \frac{<E(t)E^*(t+\tau)>}{<E(t)E^*(t)>} \right|^2, \quad (5)$$

The right side of the equation is the electric field temporal autocorrelation function, β accounts for the loss of correlation that has a relationship with the ratio of the detector size to the speckle size and polarization (92), usually it is assumed that

$$\frac{<E(t)E^*(t+\tau)>}{<E(t)E^*(t)>} = \exp\left(-\frac{\tau}{\tau_c}\right), \quad (6)$$

Therefore, the speckle contrast can be expressed as

$$K = \frac{\sigma}{<I>} = \beta^{0.5}\left\{\frac{\tau_c}{T} + \frac{\tau_c^2}{T^2}\left[\exp\left(-\frac{2T}{\tau_c}\right) - 1\right]\right\}^{0.5}. \quad (7)$$

The speckle contrast is a function of the camera exposure time T and the time scale of the sample dynamics τ_c which is related to the speed of blood flow. Although the values of K^2 are in the range of [0, 1] in theory, they are practically limited to [0, 0.1]. K^2 therefore degrades into a linear correlation with τ_c when the contrast is less than 0.1, thus the reciprocal ($1/K^2$) can be used to indicate the relative changes in blood flow.

Laser speckle contrast techniques have been applied to a large number of blood flow imaging studies such as the retina, skin and brain. These tissues are well suited to be studied by this technique because the blood flows are superficial and laser speckle contrast techniques cannot access deep tissue. Retina is one of the earliest applications of laser speckle, because the vasculature is quite accessible. Researches on retina includes the effects of pharmacological agents on retina blood flow (93, 94) and analysis of the flow around the optic nerve head (95). In recent years, laser speckle contrast

techniques have been widely applied in study of blood flow in brain, such as to measure the hemodynamic responses to various stimuli (96, 97), comparison of normal blood flow with disease blood flow (86). Skin perfusion measurement is the most mature clinical application. For example, Huang et al have used laser speckle to real-timely monitor the skin response before and after the laser therapy of port wine stain birthmark (98).

2.3.2 **Two photon excitation and second harmonic generation microscopy**

The basic principle of two-photon excitation can be illustrated by Figure 2-7. The concept of two-photon excitation is a relatively old theory. It is a nonlinear process that involves simultaneous absorption of two photons, with their combined energy sufficient to drive a molecular transition to an excited electronic state (99). Generally, photons of wavelengths λ_1 and λ_2 within the constraint follow that

$$\lambda_{1p}^{-1} \cong \frac{1}{\lambda_1} + \frac{1}{\lambda_2}, \tag{8}$$

where λ_{1p} is the wavelength needed to produce fluorescence emission in a one-photon absorption event. Practically since $\lambda_1=\lambda_2$, the equation becomes $\lambda_1 \approx 2\lambda_{1p}$ (100). This indicates that the excitation wavelength in the two-photon excitation is twice of the excitation wavelength in the identical one-photon excitation.

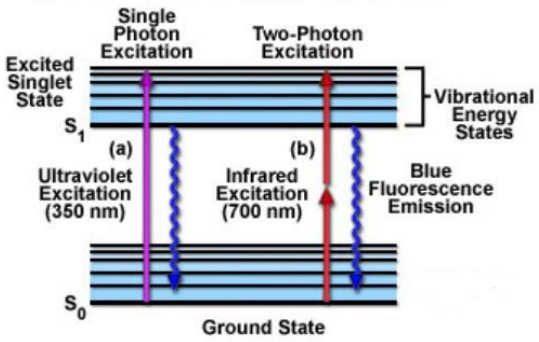

Figure 2-7. The scheme for one- and two-photon excitation. We take $\lambda_{1p} = 350nm$ for example. Fluorescent molecule is excited and shift to excited state and later relaxes back with emission at 420nm. In the identical two-photon excitation event, two photons at 700nm are absorbed simultaneously. The picture is adapted from http://www.microscopyu.com.

The interaction between the fluorophores and excitation electromagnetic field is the source of the fluorescence excitation. It is described by the time-dependent Schröedinger equation, in which the Hamiltonian contains an electric dipole interaction term: ***E, r.*** Here, ***E*** is the electric field vector of the photons, ***r*** is the position operator. The nth-order solution corresponds to n-photon excitation with transition probability ***P***. For two-photon excitation process, the probability between the molecular initial state *i* and the final state *f* is given by:

$$\boldsymbol{P} \sim \left| \sum_{\mathrm{m}} \frac{\langle f|\boldsymbol{E}\cdot\boldsymbol{r}|\mathrm{m}\rangle\langle \mathrm{m}|\boldsymbol{E}\cdot\boldsymbol{r}|i\rangle}{\varepsilon_{\gamma}-\varepsilon_{\mathrm{m}}} \right|^2, \tag{9}$$

Where ε_{γ} is the photon energy associated to the electric field ***E,*** the summation is over all intermediate states *m*, ε_{m} is the energy difference between the sate m and the ground state.

The occurrence of two-photon excitation depends much on simultaneous absorption, which means that both photons interact with the fluorophores at the same time (here, 'the same time' means a time interval less than 10^{-18} seconds). In order to produce significant numbers of two-photon excitation events, the photon density must be approximately one million times more than

that is required to generate an identical one-photon excitation. This basically means extremely high laser power is required to generate significant two-photon excitation fluorescence. This has to be achieved by focusing mode-locked (pulsed) laser, which produces pulses of light of extremely short duration (usually on the order of picoseconds (10^{-12}s) or femtoseconds (10^{-15}s)). The power at the peak of the pulse is high enough to generate two-photon excitation, but the pulse duty cycle (the duration of the pulse divided by the time between the pulses) is on the order of 10^{-5}. Therefore the average input power is around 10 mW, which just similar to the power of confocal imaging.

The narrow localization of the two-photon excitation is the basis of the technique's most significant advantages over confocal imaging. In a confocal microscope, fluorescence is excited throughout the specimen illuminated volume, and a pinhole has to be used to exclude the emission out of the focal plane. However, with two-photon excitation microscope, only the fluorescence at the focal plane is generated, the photobleaching (and photodamage) of the specimen is largely reduced. It also results in the improved axial depth discrimination and image contrast. Besides, with this character, study locally photo-initiated chemical reaction is feasible.

Practically in biological imaging application, the near IR laser source (relative to UV and visible wavelength) renders additional advantage of reduced scattering and absorption of excitation photons. In Rayleigh scattering, the scattering cross-section is inversely proportional to the fourth power of the wavelength. Therefore, the scattering event in the two-photon excitation is over an order of magnitude less likely to occur than the one-photon excitation. Although Rayleigh scattering is only an approximation of the light propagation in biological tissue, the general inverse relationship between

scattering and excitation wavelength still exists validly. Most biological tissue has reduced absorption in the near IR (refers to as 'optical window' at 700-1000nm), therefore the tissue absorption is much less than the absorption in the UV and blue-green region. The reduced scattering and absorption explain the deep penetration depth of two-photon excitation microscope.

Finally, compared to conventional one-photon microscope, in which the excitation wavelength is close to the emission wavelength, the input wavelength is significantly larger than the emission band in two-photon excitation microscope. This effectively avoids the cut-off of the emission band by the barrier filter which is used to eliminate the leak-through of the excitation light. Therefore the unnecessary detection sensitivity reduction is avoided. The optical properties of the two photon excitation microscope and the benefit derived from these optical properties is listed in Table 2-4.

Table 2-4. The optical properties of the two photon excitation microscope

Optical properties	Benefits
3D localized excitation volume (nonlinear feature of excitation)	•Improved depth discrimination and image contrast; •Reduced specimen photobleaching/photodamage •Locally photoinitiated chemical reaction
Near IR light source	•Reduced scattering (inversely proportional to 4^{th} power of wavelength) •Reduced absorption ('optical window' at 700-1000nm) =>Deep penetration depth
Excitation wavelength>>> the emission band	High signal/background ratio in fluorescence detection

Second-harmonic generation (SHG) was first described in a quartz crystal by Franken et al (101). SHG can be viewed as a special case of Sum-frequency generation (SFG) that the produced scattered beam is at exactly twice the frequency of the input beam. SHG requires that the second order optical susceptibility is non-zero, therefore it occurs only in non-centrosymmetric

molecules. Its comparison to two-photon excitation is illustrated in the Jablonski diagram (Figure 2-8). Unlike two-photon excitation, SHG involves no energy lost during relaxation and SHG does not have an excited state. Consequently, SHG does not involve excitation of molecules and no phototoxicity occurs. The SHG signal is polarization sensitive and its intensity depends on the angle between the samples and the polarization of the excitation light (102). Since no external labeling of the sample is involved for SHG, it can be used to image material with non-centrosymetric organization without labelling. Examples of such molecule are protein fibers such as collagen, microtubules and cellulose in biological application. Application of combined SHG and TPEF to conventional laser scanning microscope makes it possible to obtain information of multiple moleculars and structural constituents in the same sample.

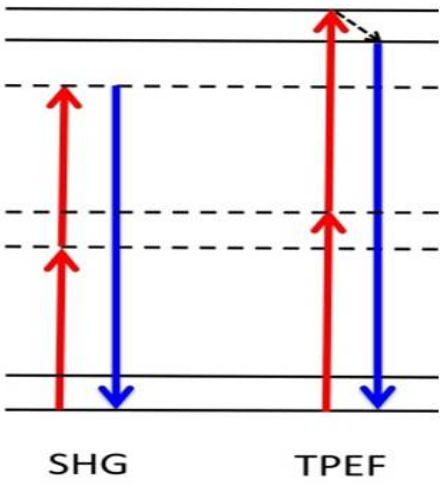

Figure 2-8. The Jablonski diagram illustrating the difference of SHG and TPEF. SHG: two photons are converted to a single photon with twice the energy (half of the wavelength). TPEF: two photons are absorbed simultaneously to excite a molecular energy state that can emit fluorescence.

The discussion of the principle of SHG has to start from the Maxwell's wave equation for a non-absorbing, non-conducting dielectric medium containing no free charges:

$$\nabla^2 \boldsymbol{E} - \frac{n^2}{c^2}\frac{\partial^2 \boldsymbol{E}}{\partial P^{NL} t^2} = \mu_0 \frac{\partial^2 \mathrm{P^{NL}}}{\partial \mathrm{t}^2}, \tag{10}$$

Where $\boldsymbol{E}$ is the electric field vector of the electromagnetic field and P^{NL} is the polarization vector. As we are only interested in second order nonlinear effects, with ignoring the higher order terms and assuming the electromagnetic waves plane waves propagating in the z direction, we simplify the electric field $\boldsymbol{E}$ to one consisting only the three infinite uniform plane waves and ignoring the effects of double refraction and focusing. It therefore can be written in the form:

$$E_j(z,t) = E_j(z)e^{-iw_j t} + c.c. = A_j(z)e^{i(k_j z - w_j t)} + c.c. \tag{11}$$

Where j = 1,2, with $w_1 = w$, $w_2 = 2w$, $\boldsymbol{E_j}$ is the complex amplitude of field j, $\boldsymbol{A_j}$ is the spatially slowly varying field amplitude and *c.c.* represents the complex conjugate. Besides, there is also

$$P_2(z,t) = P_2(z)e^{2\pi(k_1 z - w)} + c.c., \tag{12}$$

where P_2 represents the complex amplitude of the nonlinear polarization. Introducing expression (11) and (12) to the wave equation (10), we obtain

$$\frac{dA_2}{dz} = \frac{2iw}{n_2 c}\chi^{(2)} A_1^2 e^{i(2k_1 - k_2)z}. \tag{13}$$

Assuming A_1 to be constant, the amplitude of the second harmonic field after propagation through a distance L is given by

$$A_2(L) = \frac{2iw\chi^{(2)}A_1^2}{n_2 C}\frac{e^{i\Delta k} - 1}{i\Delta k L}, \tag{14}$$

where $\Delta k = k_1 - k_2$. The intensity of the generated radiation is thus

$$I_2(L) = \sqrt{\frac{\mu_0}{\varepsilon_0}}\frac{2w^2}{n_1^2 n_2 c^2}\left[\chi^{(2)}\right]^2 I_1^2 L^2 \left[sinc^2\left(\frac{\Delta k L}{2}\right)\right]. \tag{15}$$

Only the interactions with $\Delta k = 0$ will undergo macroscopic amplifications as they propagate through the medium. Even though the second order nonlinear susceptibility (non-centrosymmetric medium) is satisfied, nonlinear emission dipoles aligned in an anti-parallel arrangement that produce SHG exactly out of phase, may result in the cancellation of the signals due to destructive interference.

TPEF and SHG have been widely applied to biomedical research. Its capability of deep imaging is especially valuable for in vivo imaging (103). The in vivo applications include imaging of brain, where a cranial window is used on the thinned skull of living animals (104-106); mammalian embryos (107-109) and retina(110, 111). The application to in vivo liver study started from recent year. For example, Thorling et al. used two-photon microscopy to visualize zonal damage after the hepatic ischemia-reperfusion injury (Figure 2-9) (112) . The same group has also studied drug distribution and metabolism in the live rat liver using two-photon microscopy (113).

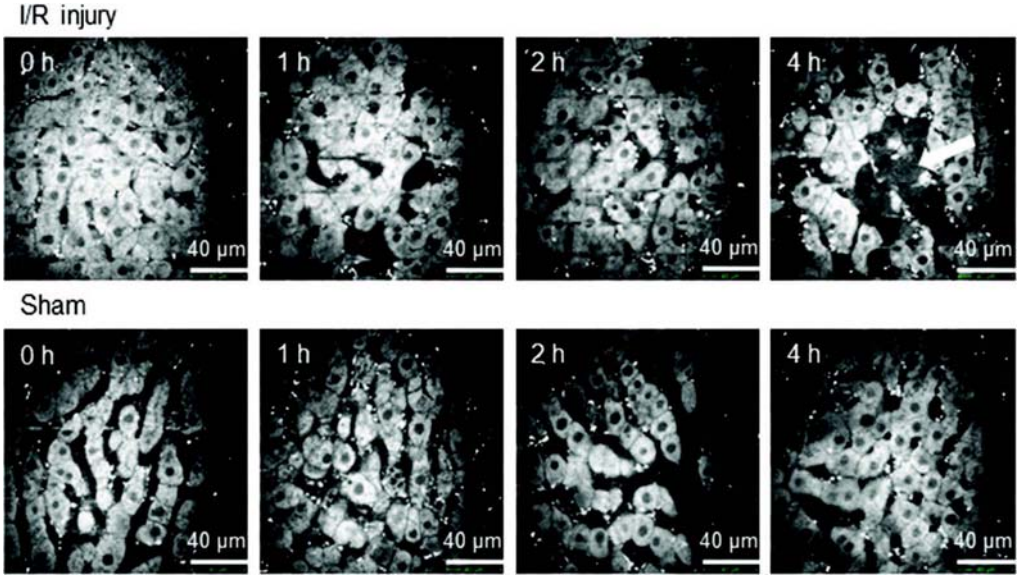

Figure 2-9. Two-photon microscopy images of liver in vivo after ischemia-reperfusion injury at various reperfusion time points. Figure adapted from reference (112).

2.3.3 **Raman spectroscopy**

Raman spectroscopy is an invaluable technique for investigation of molecules. It involves shinning the monochromatic laser light on a sample and detecting the inelastic scattered light. The inelastic scattering means that the frequency of the monochromatic photons shifts (up or down) upon interaction with the

samples. It is also called the Raman effect. The basic origins of Raman effect is illustrate as below.

The molecular deformations in electric field $\boldsymbol{E}$ is determined by molecular polarizability α. The laser beam forms an oscillating electromagnetic field with electrical vector $\boldsymbol{E}$. Upon interaction with the sample molecules, it induces electric dipole moment $P = \alpha \boldsymbol{E}$, which deforms molecules. With periodic deformation, the molecules start vibrating with the characteristic frequency ν_m. The amplitude of vibration is called a nuclear displacement. The emission light from the oscillating dipoles has three different frequencies (Figure 2-10):

1. A molecule with no Raman-active modes absorbs a photon with the frequency ν_0. The excited molecule returns back to the same basic vibrational state and emits light with the same frequency ν_0. This type of interaction is called an elastic Rayleigh scattering.
2. A molecule with Raman-active mode absorbs a photon with the frequency ν_0. Parts of the energy is transferred to the Raman-active mode with frequency ν_m, therefore the resulting scattered light has the frequency of ν_0-ν_m. This type of interaction is called inelastic Stokes Raman scattering.
3. A molecule with Raman-active mode absorbs a photon with the frequency ν_0. The molecule is already in the excited vibrational state, excessive energy of the excited Raman active mode with the frequency ν_m is released. Molecule returns to the basic vibrational state and the frequency of the scattered light goes up to $\nu_0+\nu_m$. This type of interaction is called inelastic Anti-Stokes Raman scattering.

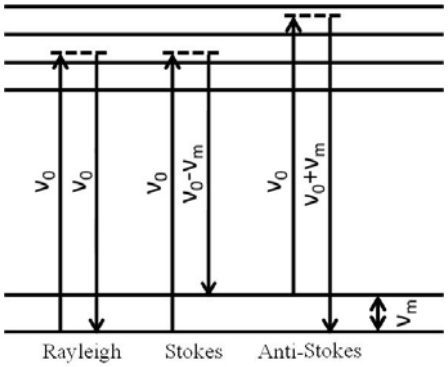

Figure 2-10. Vibrational energy level diagram showing Rayleigh and Raman scattering.

Raman microscope is used in many fields where non-destructive microscopic chemical analysis and imaging is required. Both Biologists and Chemists use Raman Spectroscopy to identify chemical compounds, their functional groups, and to determine the conformation of complex biomolecules, such as proteins and DNA. It can be used to rapidly characterize the chemical composition and structure of a sample, whether solid, liquid, gas, gel, slurry or powder. It is particularly amenable to in vivo measurements.

In the study of biological tissue sample, the Raman spectroscopy has advantages over fluorescence microscopy as it requires no external labeling. The contrast is generated in the cross section of Raman scattering due to induced polarizability generated in the tissue. Near-IR excited Raman spectroscopy was discovered to have advantages in studying biological tissue in 1986 (114), because with IR excitation, Raman spectra can be measured when previously they are immeasurable due to fluorescence interference. The features of near IR Raman spectroscopy includes: firstly, the extinction coefficients of biological tissues are small at near-IR excitation wavelengths; secondly, water is a weaker absorber in the near-IR so that won't interfere the measurement, when biological cells consist of 70-90% of water by weight; thirdly, the excitation light at near-IR wavelength is easily transmitted through

optical fiber, enabling remote collection of Raman spectra. Near-IR Raman spectroscopy has wide application in clinical study. One important application is cancer detection. Raman spectroscopy is able to identify markers associated with malignant changes. Liu et al. have explored its potential for diagnosing malignant lesion in the gynecological tract (115). Shafer-Peltier et al. have created a Raman microspectroscopic model of human breast tissue (116). Feld et al. used 830nm excited CCD Raman spectroscopy to collect spectra from normal and colonic carcinomatous tissues (117). Other applications include the study of atherosclerosis (118), brain (119) and soft tissue sarcomas (120).

Chapter 3 Study of Hepatic Microcirculation in Liver Fibrosis

3.1 Introduction

Hepatic vascular disorder is known as a symptom of chronic liver disease. Although commonly regarded as secondary to primary injury (such as alcohol abuse, viral hepatitis and toxic exposure), the onset of vascular disorder is detrimental to hepatocytes by inhibiting the provision of nutrients and oxygen (this is exactly the main function of normal hepatic microcirculation system). In previous research, vascular disorder is regarded as critical to the progression of chronic liver disease (especially, NASH and alcoholic fatty liver), because once the vascular disorder is presented, ischemic injury comes out and leads to focal collapse of the tissue; the accumulated focal collapse results in widespread parenchymal extinction (8, 121), which is the omen of liver failure and end stage liver disease. Therefore, the prominent importance of microcirculation highlighted the need of technical development to detect hepatic microvascular abnormalities in vivo.

Several techniques have previously been used to study the hepatic microcirculation, including radio/fluorescence labeled microspheres (122), hepatic clearance of tracer substances(123, 124), in vivo fluorescence microscopy (125, 126) and laser Doppler flowmetry (127, 128). However, most techniques are limited by the recruitment of extra contrast-enhancer, such as fluorescent dextran and fluorescence labeled red blood cells, because the contrast enhancer would introduce undesirable impacts to the liver cells and microcirculation (129, 130). Among all the techniques, doppler flowmetry technique is label-free but the Doppler signal is easily deteriorated due to

phase wrapping and interferometric fringe washout effects, resulting in measurement ambiguities and loss of information (131). In the main part of this chapter, we describe a methodology of combining wide-field fluorescence microscope and laser speckle contrast imaging (LSCI) techniques to study liver microcirculation without labeling.

The use of wide-field fluorescence microscope is to take advantage of the endogenous fluorophores inside hepatocytes, such as NAD(P)H, flavins inside hepatocytes and vitamin A inside hepatic stellate cells (132). Their existences give rise to autofluorescence emission, enabling the locating of hepatocytes and hepatic stellate cells. LSCI (133) has in recent years attracted considerable attention in both laboratory research and clinical application because of its advantage in spatiotemporal resolution. It is widely used to monitor capillary blood flow (134, 135), image blood coagulation (136), and blood perfusion mapping (87, 88, 137). Intensive study on its clinical application has also been conducted in skin (138), retina (139, 140) and neurosurgical application (141-143). Laser speckle is produced when coherent light is shone onto a random medium, and the scattered light is collected by a camera detector. The moving particles in the medium, such as red blood cells (RBC) in blood vessels, will cause the pattern to fluctuate as a result of time-varying phase shifts. Both temporal and spatial intensity variation of the speckle can be analyzed to resolve the motion of the scattering particle, i.e. the RBC, and thus the information of the blood flow. Practically, the intensity variation is quantified as temporal or spatial contrast value. The temporal contrast, mainly used in the experiment, is computed through the division between the temporal standard deviation and the temporal mean of every pixel. Areas with greater motion will render faster intensity fluctuations and therefore more blurred speckle within a certain camera exposure time. The contrast thus will be

smaller due to smaller temporal standard deviation of the intensity. A combination of the wide-field fluorescence microscope and LSCI will yield a complementary function by visualizing both the hepatic parenchymal tissue and microcirculation. Neither of each requires the use of external contrast agent, endowing this method with good potential of long-term liver disease monitoring on animal model.

In this chapter, we start with the design of the intra-vital imaging window, followed by the setup of the instrument. To demonstrate the ability of the instrument in chacterizing hepatic microcirculation lesion, we create the rat primary biliary fibrosis model through Bile Duct Ligation (BDL) surgery. The model has been previously investigated regarding both morphological and functional changes of liver (144-146), yet studies focus on the relationship between microcirculation lesion and the disease progression are rare. Bearing the hypothesis that the microcirculation lesion is correlated with the fibrosis progression in this fibrosis model, in this chapter, we characterize hepatic microcirculation change with progression of fibrosis. We have viewed the morphological change and flow speed change of hepatic microcirculation with the progression of fibrosis. By further analyzing the obtained digital image with imaging processing techniques, we quantify the hepatic microcirculation changes, and scrutinize the correlations between its changed features with fibrosis progression. This experiment suggests the potential application of this method in studying liver fibrosis and other chronic liver disease.

3.2 Materials and methods

3.2.1 Design of Intra-vital imaging window for in vivo imaging of liver

To perform in vivo imaging, intravital hepatic imaging window for rodents was modified based on the design of Liu et.al (147). The basic idea for the imaging window design is to open a window on the abdomen skin of the rodents, exposing the liver but ensuring that the imaging procedure introduces little invasion to the abdominal organs. For ease of in vivo imaging, the chamber should have the following features:

1. Easy to be stabilized relative to the microscope, so that the artificial movement induced by animals' heartbeat and breath can be overcame;
2. Ensure the imaging area is as large as possible but at the same time flat enough to facilitate the light penetration.

The prototype of the first generation rat imaging window was illustrated using SolidWorks (Dassault Systèmes *SolidWorks* Corp.) in Figure 3-1(b). In the design, all the components can either be locked or screwed to ensure the stability. Besides, in practical experiment, we purposely use inverted microscope for in vivo imaging, so that the animals are lying on belly facing down during the imaging. Their body weight will exert pressure to the liver as well as to the window. Therefore the imaging site is less influenced by heart beat and breath. In this way the stability is assured. In order to make sure the imaging area is large but flat, the diameter size of the window is designed to be less than 20mm as shown in Figure 3-1(a) in order to match the actual size of the rat liver. The cover slip used together with the imaging chamber is 22x22 mm square cover slip which is commercial available.

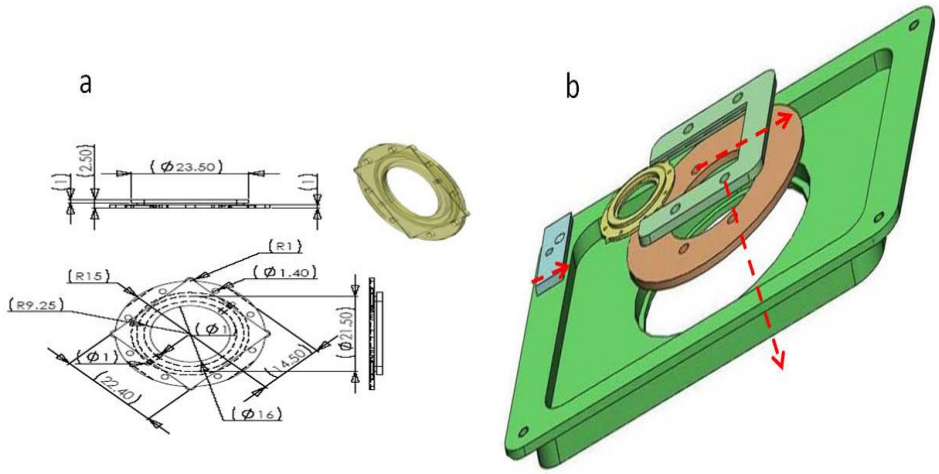

Figure 3-1. The first generation of rat liver imaging window. (a) The design and size of the inner ring, which is to be installed onto the skin of animal through surgical suturing. (b) The assembly diagram, every part can be locked or screwed to ensure stability.

The inner ring of the window is to be sutured to the animal's abdominal skin, the other parts are designed to secure the window to the sample stage of the microscope. The design was fabricated with medical grade titanium because titanium has good biocompatibility and is used in most implantable medical device. The final prototype is showed in Figure 3-2. Figure 3-2(a) shows the components designed to secure the window. They include a u-shaped holder to lock the window (inner ring), and a ring holder that is attached to the u-shape holder and connects all the components to the plate by fitting inside the big hole. The plate is shown in Figure 3-2(b). A small screw on the side of the plate is used to lock the ring holder. Figure 3-2(c) shows the imaging window with all parts assembled.

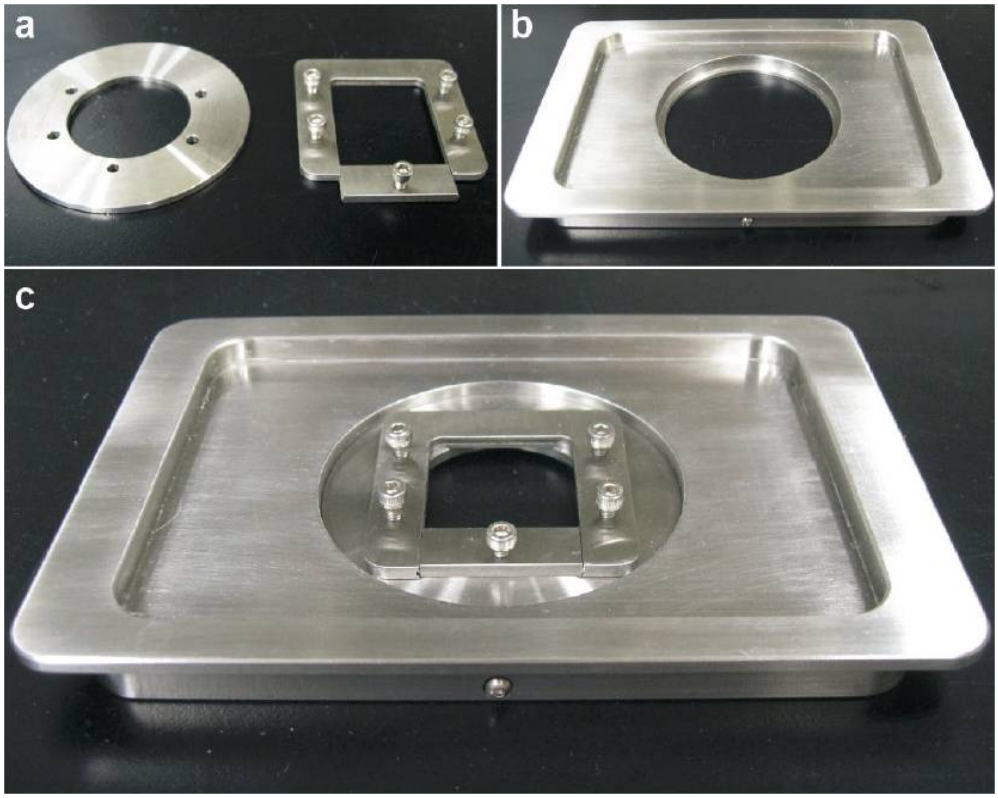

Figure 3-2. The final prototype of the rat imaging window. (a) The u-shape holder to lock the inner window and the ring holder to connect the u-shape holder to the stage. (b) The plate that holds the animal. It will be inserted to the microscope sample stage. (c) The imaging window with all parts assembled.

Based on our first generation imaging window design, we later improved the design with the aim of simplifying the surgical installation procedure. The purpose of doing so is to save time for window installation so that we will have more time for in vivo imaging. It could also benefit the experiment by reducing the usage of anesthetic drug or avoiding the repeating anaesthetizing procedure. The second generation window is illustrated in Figure 3-3. In this design, the whole window is simplified to three parts. Only the ring to be sutured to the skin is fabricated using medical grade titanium, the other parts are made by aluminum alloy. This has largely decreased the cost of fabrication.

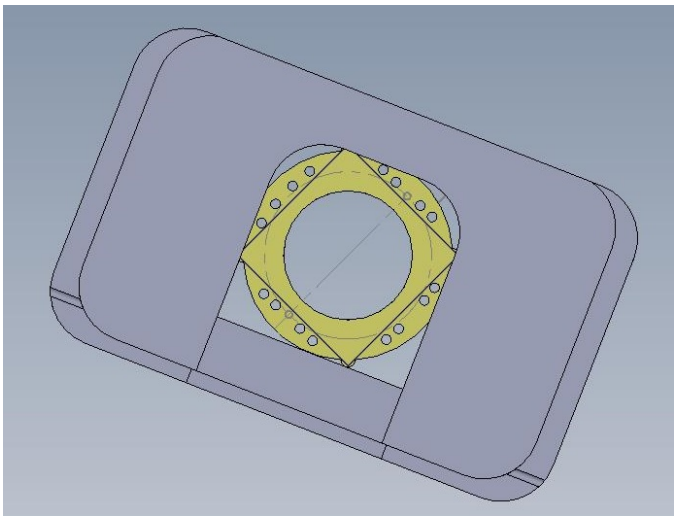

Figure 3-3. The second generation rat imaging window design. The design has been simplified to three components. It is handy to use and largely reduces the cost of fabrication.

On the basis of our second generation rat imaging window, we revise the design to fit on mice because mice are more widely used in study of liver cancer than rat because of the availability of genetically-altered mice. However, since in all the animal experiment in this thesis, rat is used instead of mice, here we only show the design of the mice window chamber, its application and evaluation is not included in this thesis. The design of the mice imaging window is showed in Figure 3-4. Different from the rat imaging window design, in which the plate is directly inserted into the microscope, the mice imaging window is of much smaller size (55mm x 75mm). The length of the mice imaging window is the same as a histological glass slides, which means it fits to the object stage of microscope just like a glass slides. This feature increases the adaptability of the window to different modal of microscope. The fabrication of the mouse imaging window is showed in Figure 3-5.

Figure 3-4. Different views of mice imaging window design. This design is revised based on the second generation rat imaging window design, but it is in a much smaller size. It could be stabilized to the microscope's sample plate like histology slides. This feature makes it able to adapt to different microscope models.

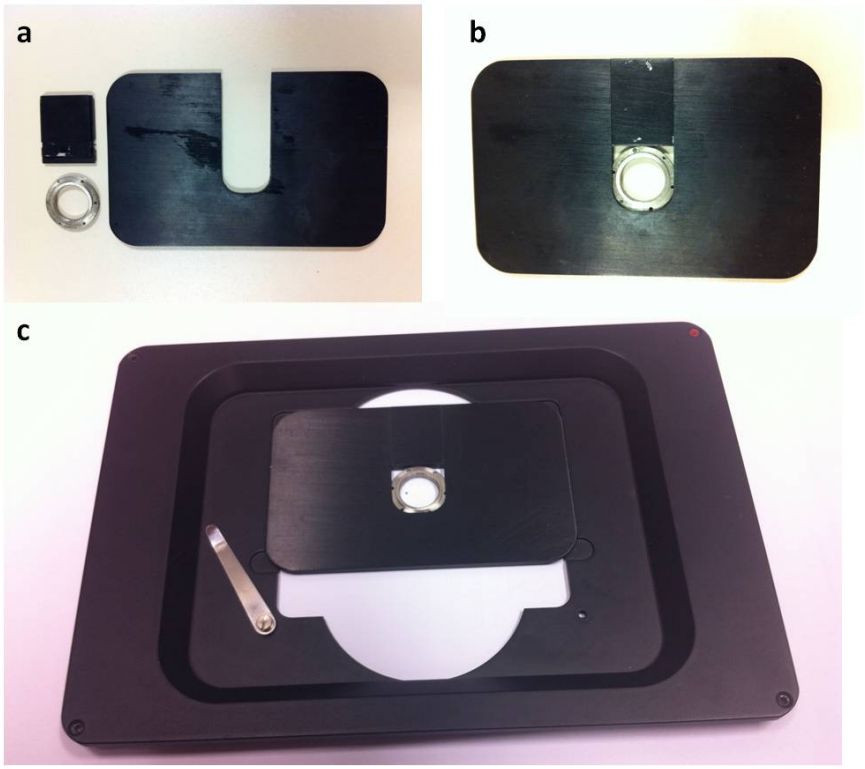

Figure 3-5. The fabrication of mouse imaging window. (a) There are three main components in this design; only the inner ring is made of medical grade titanium, the other two parts are made of aluminum alloy. (b) The assembled window is showed.

The mouse window is designed at the size of a glass slide, so it easily fits to different microscope models.

3.2.2 **Statistics of laser speckle**

The computation of the spatial contrast is achieved by sliding a window with pixel size of 5×5 or 7×7 over the whole raw image and estimate the contrast, the contrast will be assign to the middle pixel of the window. This can be realized in MATLAB by:

```
winsz = 5; %window size
Imp = padarray(Im,[winsz winsz],'replicate');% pad the border of the image by replicating the border element, Im = raw image
conIm = nlfilter(Imp,[winsz winsz],@contrast); % sliding the window through the image by performing the 'contrast' function

% 'contrast' function
function [Ki] = contrast(A)
Ki=std2(A)/mean2(A);
end
```

The computation of temporal contrast uses temporal standard deviation and temporal intensity mean, which is achieved from the statistics along n (usually n = 20) frames of images in temporal dimension. This can be realized in MATLAB by:

```
% read image of size rownum * colnum to a combo
for comboindex = 1:n;
    combo(1:rownum,1:colnum,comboindex) = imread(filename);
end

% calculate the temporal contrast of each pixel
for rowindex = 1:rownum;
    for colindex = 1:colnum;
        tempstd = std(combo(rowindex,colindex,:));
        tempmean = mean(combo(rowindex,colindex,:));
        tempconIm(rowindex,colindex) = tempstd./tempmean;
    end
end
```

3.2.3 **Experiment setup and image acquisition**

The experiment set-up is presented in Figure 3-6(a). The wide-field illumination provided by a mercury lamp passed through a long pass filter set (ET470/24x, 510dcxr, HQ525lp, Chroma Technology), the specifications of each filter is listed in Table 3-1. The LSCI employed a diode laser (CrystaLaser, USA, λ=638nm, 25mW) to coherently illuminate the imaging site with an incident angle of about 30 deg. Images were acquired by the CCD camera (DP72, Olympus) after light passing through the objective lens (LD Plan-Neofluar, 20x, NA=0.4, Carl Zeiss). For each imaging site, five wide-field fluorescence images were taken followed by 200 frames of raw speckle images with size of 1024×1360 pixels and capture frequency of 15Hz. The exposure time was set to 75ms for fluorescence images and 20ms for speckle images.

Table 3-1. The specifications of long pass filter set.

Filter type	Quote number	Specifications
Emission	ET470/24x	CWL:470nm, FWHM:24nm
Dichroic	510dcxr	Cut on/off: 510nm
Excitation	HQ525lp	Cut on/off: 525nm

2D blood flow map was obtained by calculating the speckle contrast temporally, which is to estimate the speckle contrast from 20 consecutive frames of raw images in the temporal dimension. To increase the signal-to noise ratio, we used the average of 10 speckle contrast images to analyze the blood flow. The resulting wide-field fluorescence image in showed in Figure 3-6(b), the result blood flow map is showed in Figure 3-6(c). The blue color on the map indicates faster speed while the red color indicates slower speed.

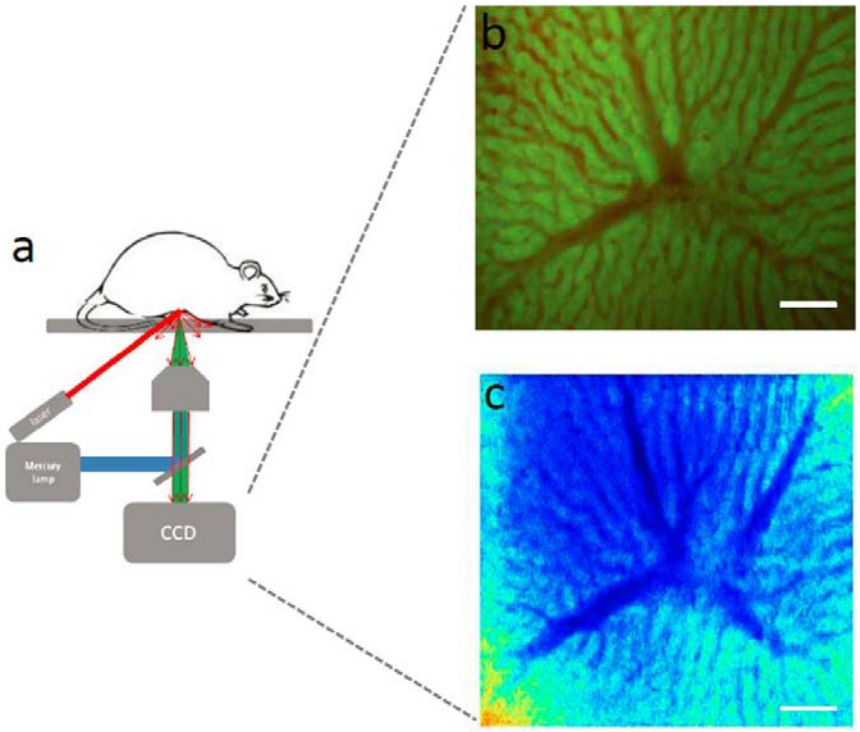

Figure 3-6. (a) Schematic illustration of the optical set-up. For the wide-field fluorescence microscope, the light generated by mercury lamp passes through a long pass filter set (ET470/24x, 510dcxr, HQ525lp, Chroma Technology). The LSCI recruits a diode laser (λ=638nm, 25mW output) as light source with an incident angle of about 30deg. Resulting images were collected by a CCD camera. (b) Wide-field fluorescence image. (c) Blood flow contrast color map of the same imaging site. Scale bar: 100um.

3.2.4 **Liver fibrosis model establishment by Bile Duct Ligation (BDL)**

In this experiment, we use Bile Duct Ligation (BDL) surgery to create liver fibrosis model. The procedure of the BDL surgery is as follows:

Before the surgery, surgical instruments are autoclaved at 121°C for 30 minutes. Autoclaved items are dated, labeled and must be used within a week. Surgical space is disinfected with 70% ethanol. The rats are transported to the preparation room and sedated, under general anesthesia with ketamine (75mg/kg) and xylazine (10mg/kg) (148). Animals are then shaved on the

abdomen and fur is removed with a vacuum evacuator. Operation site is scrubbed with 1% iodine followed by 70% ethanol, repeated three times. The rat will be injected with 5ml 0.9% NaCl S.C perioperatively. The abdomen is then draped. The surgical team will do a five minute wash of hands and forearm to remove the microbes from the skin, using chlorhexidine preparations. Hands are rinsed with running water from hand to elbows and dried with sterile towels. The surgeon then wears gowns and gloves with the help of an assistant, ensuring sterile technique.

Common BDL of rat is performed according to the protocol of Maria-Angeles Aller et.al (149). Briefly, a midline laparotomy is performed, exposing the liver. The common bile duct is doubly ligated in two areas near the hilum with 6-0 silk suture and then transected between the two ligation points (Figure 3-7). Abdominal contents are gently rearranged, and the wound is closed with double layered tissue closure using 3-0 vicryl sutures. Tetracycline HCL is applied on the closure wound and plastered with a water proofing protection.

After the surgery, animal will be monitored every 4 hours the first day, and every 24 hours till the day on which the rat is ready for imaging. The appetite, condition of the surgical wound, state of arousal, indices of pain or discomfort will be monitored and recorded.

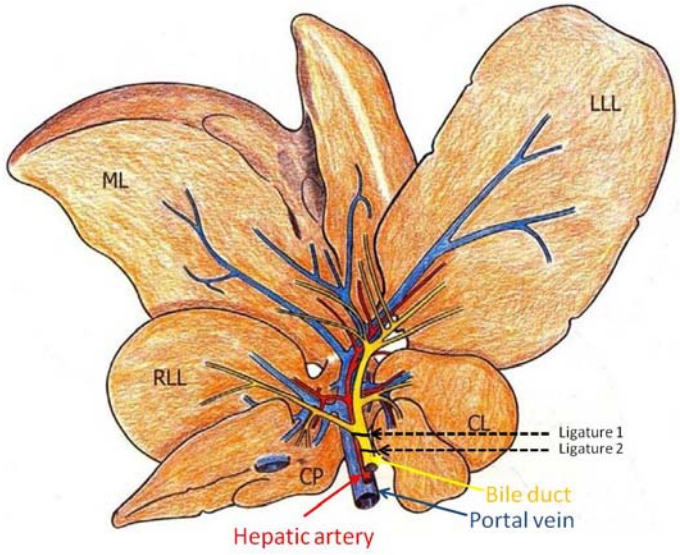

Figure 3-7. The illustration of the transaction site of on the common bile duct. Picture is adapted from ref (150). The bile duct is transected between two ligatures. RLL: right lateral lobe. ML: middle lobe. LLL: left lateral lobe. CL: caudate lobe. CP: caudate process.

3.2.5 **Animal preparation for in vivo microcirculation study**

To prepare the animal for the in vivo imaging experiment, rat is anesthetized using ketamine (75mg/kg) and xylazine (10mg/kg) (148). A midline incision of abdomen skin and muscle is created after shaving. The inner ring of the hepatic imaging window is sutured inside the abdominal wall through the holes on the ring. In order to minimize motional artifacts associated with respiration, tissue adhesive (vetbond 3M, USA) is applied to the edge of the inner lid to adhere the left lobe of liver to the ring. A cover glass is then adhered to the lid to serve as an observation window. The following procedure of applying imaging window is using the first generation rat imaging window. The rat with the window installed is kept in the supine position, then the window is fitted into the U-shape ring holder, which is then screwed tight to another round ring holder that fits into the steel plate. There is a small screw on the flank of the plate to lock the round steel plane. The plate is then attached to the stage for live imaging purpose. A hot pack is put on top of the

rat for warming purpose. All experiment procedures described in this chapter are carried out in compliance with the National Advisory committee For Laboratory Animal Research (NACLAR) Guidelines. The protocol is approved by Institutional Animal Care and Use Committee. inserted to the microscope sample stage. In this way, the rat could be firmly

For the experiment of looking for microcirculation imaging features, a total of 15 rats at the age of 9-12 week old are ligated and proceeded to in vivo imaging at intervals of 1, 3, and 5 weeks (n=5 per week) after ligation. Another five rats are sham operated and sent to in vivo imaging as a control group. To prepare animal for in vivo study, the hepatic imaging window was used to expose the liver for imaging.

3.2.6 **Image segmentation and features extraction**

Image processing is performed to quantify the resulting images using MATLAB (Mathworks, Massachusetts). The wide-field images are first filtered by the Frangi filter (151, 152) to enhance the blood vessel conduit from a noisy background. Different scales of the Gaussian kernel with σfrom 1 to 8 are used in the Frangi filter and the intensity of each pixel in the filtered images is assigned with the maximum output value of the Frangi filter among all the scales assessed. The filtered images are then thresholded. Delaunay triangles are computed from the thresholded image boundary points. The medial axis transforms (MATs) are obtained from the Delaunay triangles (153). The MAT consists of the vessel centerline and radius. The flowchart of imaging processing procedure is illustrated in the Figure 3-8. Four parameters are identified through imaging processing. They are (1) number of junctions inside each image; (2) the averaged vessel breadth, which is the averaged diameter of the vessels within each image; (3) the vessel area, which is defined

as the integral of the diameter of vessel over the vessel length; (4) the average perfusion speed. In order to obtain the averaged perfusion speed, we identify the vessel region on the LSCI blood perfusion map. The contrast value of every pixel within the vessel region is averaged and transferred to the speed according to the relationship between contrast value and the speed.

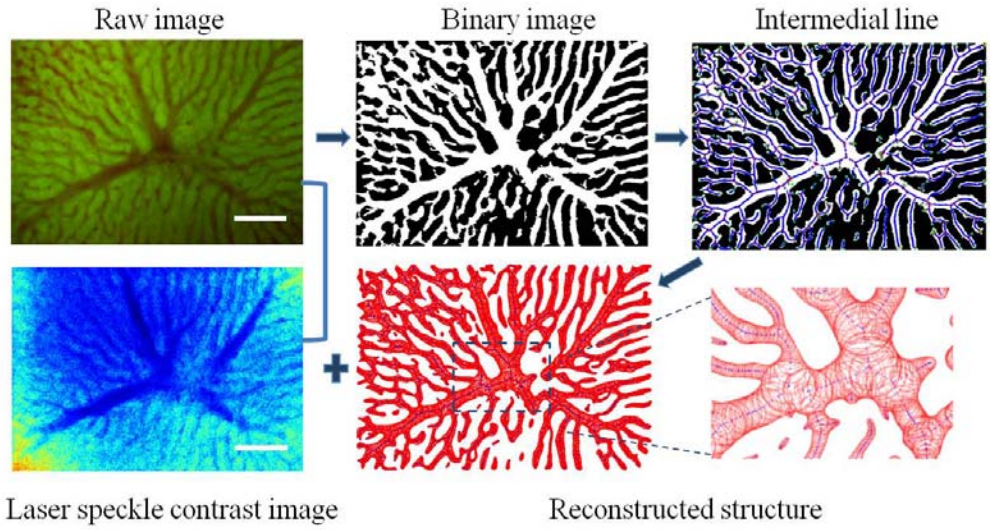

Figure 3-8. The flowchart of imaging processing procedure. Raw wide-field fluorescence image is firstly Frangi filtered and thresholded to obtain the binary image. Delaunay triangle was computed and the MAT was acquired to get the vessel centerline and radius. Using the resulting centerlines and radii of all vessels, the vessel structure could be reconstructed, so that the feature of number of junction, average vessel breadth and vessel area can be extracted. Combing the reconstructed structure and the laser speckle contrast flow map enables us to identify the vessel region and obtain the averaged flow speed.

3.2.7 **Quantification and statistics analysis**

Statistical analysis is carried out using SPSS 20 (IBM Corporation). The rats are grouped into different stages according to the tissue histological review. Since multiple images are taken from a single rat, each image is treated as a sample. Because the normality assumptions are not always satisfied for every group, the equivalent non-parametric Mann Whitney U/Wilcoxon Ranked Sum test is used to test the differences of each feature between two consecutive groups. $p<0.05$ implies a statistically significant difference. Data

is presented using mean±s.e., The data is normalized towards the mean of the normal group. ROC Curves are also plotted to evaluate and compare the performance of each parameter in classifying the disease progression.

3.2.8 **Liver sample extraction, processing and staining**

After in vivo imaging, before the animal is euthanized, one dose of 0.5ml heparin is given to the rats injected through tail vein, to suppress the blood platelet agglutination; then cardiac perfusion with 10% paraformaldehyde is performed to flush out the blood cells and fix the liver tissue before harvesting. Liver specimens from left lateral lobe are preserved in buffered fixative for further slicing preparation.

After fixation, the tissue is dehydrated by first using graded ethanol solutions, followed by graded xylene solutions and finally liquid paraffin. The graded solutions would expose the sample to changes in hydrophobicity gradually, thus minimizing the damage to cells. After a short time in the liquid paraffin, the tissue is placed into a mold with more paraffin. In this way, the infiltrated tissue is embedded into a paraffin block. The embedded samples are then cut into 15μm thick sections. After the several slices of the paraffin-embedded tissue have been sectioned, the slices are removed from the blade and floated atop a warm water bath to smooth out the sample. The slices are teased apart and floated onto a glace slide. Place the slides with paraffin section on the warm block in a 65^{o}C oven for 20 minutes in order to melt the wax and bond the tissue to the glass. To prepare the slides ready for staining, deparaffinize the slides with 2-3 changes of xylene and hydrate in increasing graded ethanol solutions, then rinse with distilled water. Every two consecutive tissue samples are stained separately with Masson Trichrome (MT) and Hematoxylin/Eosin (H&E).

3.2.9 **Histopathological scoring of tissue sample**

The stained tissue slides are imaged with bright-field microscopy (Aperio Digital Pathology Environment). Animal tissue score is performed by experienced histopathologist based on modified Ruwart score according to Ruwart et al (154) and Boigk et al (155). Because there is extensive bile duct proliferation noted. The modified Ishak (156) score is also considered and served as a guide to commensurate animal pathological score with the clinical human scoring system.

3.3 Results and discussions

3.3.1 Intravital imaging window for live liver imaging

All three designs of the imaging window can meet the requirement of stability. The second generation rat imaging window is much easier to handle than the first generation, the mice imaging window based on the second generation rat imaging window is also handy to use. During the experiment, we compared the inner ring made of titanium alloy and aluminum alloy, and found that the imaging window fabricated using titanium alloy is more durable, because repeated autoclaving of the imaging window will deform the fine features, such as the brim of the slide slot, if the window is made of aluminum alloy. Besides, the titanium alloy is less tending to induce inflammation reaction of the abdominal wall than aluminum alloy. Therefore, that the titanium alloy is the most desirable material for such implantable device. Considering the price of fabrication, we finally decided to fabricate only the implantable part with titanium, the other parts are still made of aluminum alloy.

Figure 3-9 illustrates the usage of the imaging window on rats. Four steps are involved in achieving this: first, suturing the inner ring to the abdominal skin of the rat (Figure 3-9(a)); second, insert the inner ring to the u-shape holder and lock the u-shape holder by screwing it to the ring holder (Figure 3-9(b)); third, insert the ring holder to the plate and lock it using the small screw on the side (Figure 3-9(c)); forth, placing the plate to the microscope sample stage (Figure 3-9(d)).

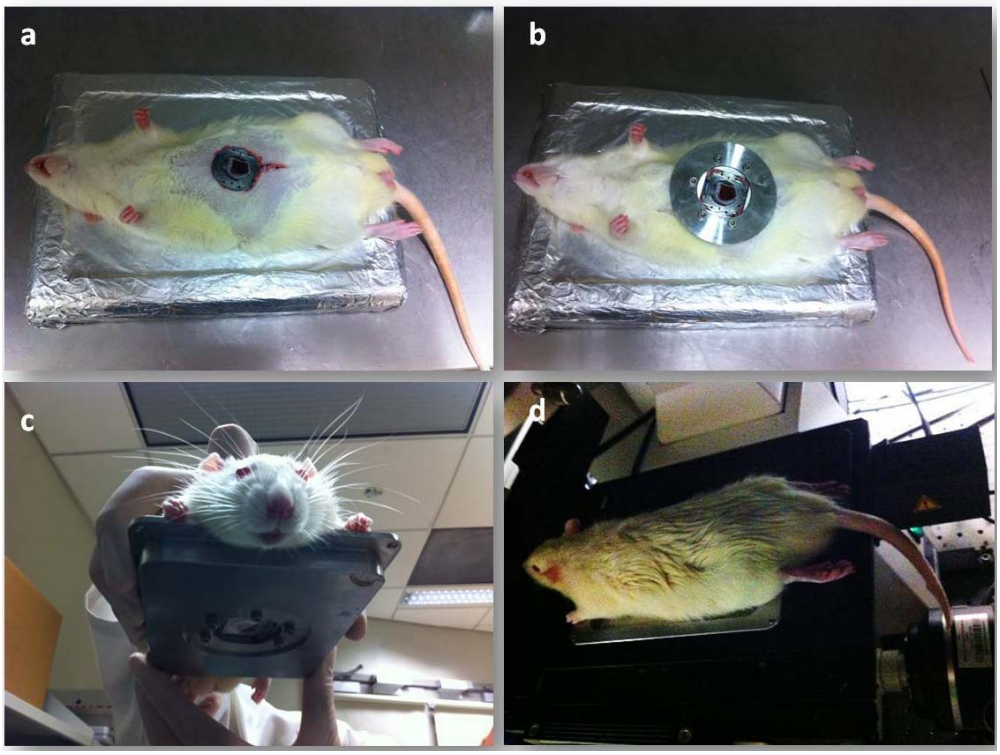

Figure 3-9. The illustration of using the imaging window on rat. (a) Suturing the inner ring to the abdominal skin of the rat. (b) Connecting both the U-shape holder and the ring holder to the inner ring. (c) Locking the ring holder to the plate. (d) Placing the plate to the microscope stage.

Some points require full attention during the experiment: first, when using the tissue adhesive, we must be cautious not to apply too much and never make the adhesive to drop onto the liver surface. The adhesive is volatile and easy to create haze if applied too much. Under the two-photon microscope, the adhesive could generate second harmonic generation (SHG) signal as the collagen inside the liver capsule does, therefore dropping of tissue adhesive on the liver surface could confuse the imaging result; second, the artificial movement due to animal breathing and heartbeat is a big headache during the live imaging of animal liver. In order to reduce this effect, the depth of the anesthesia is of most importance. Controlling the anesthesia is nothing more than experience of anesthetics dosing according to the animal weight and health status.

3.3.2 **Spatial and temporal laser speckle contrast**

Spatial contrast and temporal contrast are two methods to resolve laser speckle. Spatial speckle contrast is estimated from the mean and standard deviation of the speckle intensity, which are generally determined from a square region of N_{pixels} (i.e. $N_{pixels}^{1/2} \times N_{pixels}^{1/2}$). A larger value of N_{pixels} will yield a more accurate estimate of speckle contrast, but at the expense of spatial resolution. It is suggested that the window size of 5×5 or 7×7 pixels are reasonable trade-off between spatial resolution and uncertainty in the estimated speckle contrast. However, it all depends on camera resolution, speckle size, and desired contrast resolution. To study the effect of window size on contrast value (K), we chose one images as Figure 3-10(b), the corresponding wide-field fluorescence image is showed in Figure 3-10(a), spatial contrast was calculated when window size equals to 3×3, 5×5, 7×7, and 9×9. The resulting flow maps are showed in Figure 3-10(c) - (f). It's obvious that the spatial resolution has decreased with the enlargement of the window size. In Figure 3-10(f) the grain appearance has been very obvious because of the loss of the spatial information. We may take it for granted that the smaller the window sizes the better. However, the size of the window size has to compromise with the computing time. When the window size is small, longer time is required to calculate the resulting flow map. Moreover, the smaller window size means smaller sample size in calculating the contrast, the accuracy is also undermined. Therefore, the window size of 5×5 and 7×7 is widely used in most literature (157, 158).

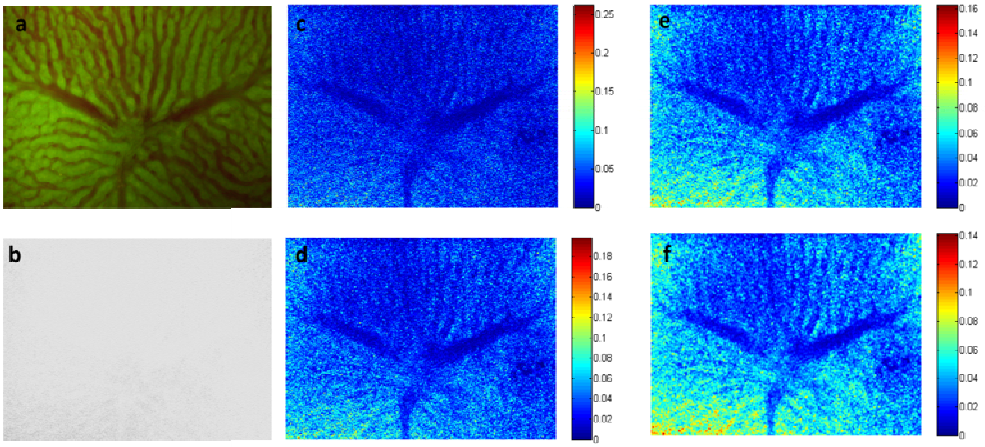

Figure 3-10. (a) The wide field fluorescence image of liver surface. (b) The corresponding laser speckle raw images. (c) The resulting flow map using spatial contrast with window size equals to 3×3. (d) The resulting flow map using spatial contrast with window size equals to 5×5. (e) The resulting flow map using spatial contrast with window size equals to 7×7. (d) The resulting flow map using spatial contrast with window size equals to 9×9.

To gain a more quantitative understanding of the relationship between the quality of contrast image and the window size, and to understand the reason of choosing 5×5 or 7×7 window size, we did the following test: three locations in the image were chosen manually, where A is a large portal vein, B is a sinusoidal and C is parenchyma. a 11×11 observation window were placed over these locations as showed on Figure 3-11 (a), the corresponding contrast values are obtained and plotted in Figure 3-11(b). An interesting finding is the contrast value becomes larger as window size enlarges. It is likely that more pixel values corresponding to the slower and nonmoving scatters are included in the computation of contrast value. Therefore, the contrast value tends to increase as window size enlarges. To explain the choosing of window size of 5×5 and 7×7, 1-SD error was used as the threshold of selection criteria, when a K value exceeds 1-SD, it will be rejected. From the Figure 3-11(c), It is noticed that only when window size equals to 5×5 and 7×7, the contrast values

at three locations lie within the 1-SD error. It is expected that images are noisy when window size equals to 3×3 with most pixels have lower contrast value, while when window size equals to 9×9 most pixels have higher contrast value. Refer back to Figure 3-10(c) and (f), in both cases, smaller vessels disappear from the image.

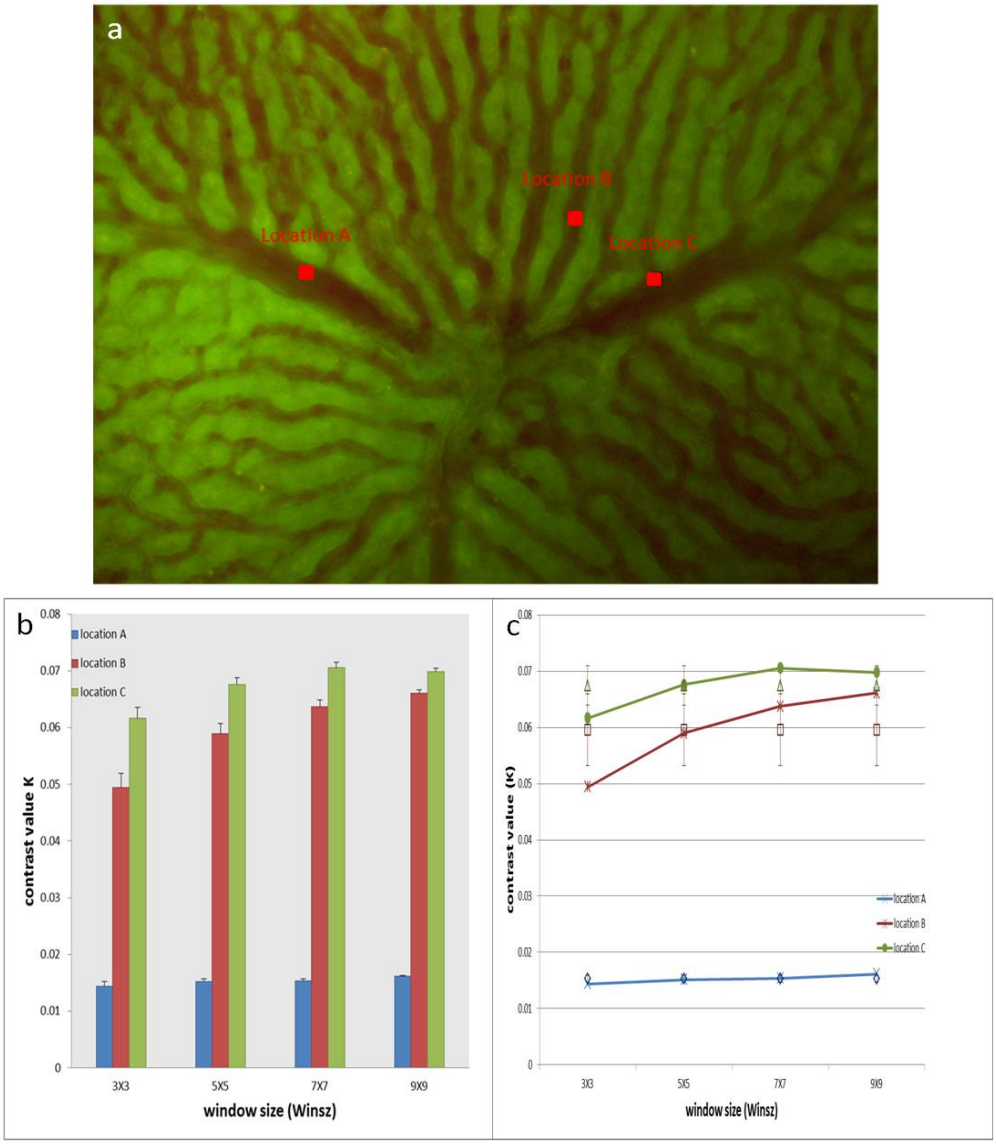

Figure 3-11. (a) To understand why window size 5×5 and 7×7 are widely used to calculate the spatial contrast, three points are chosen from the image, a 11×11 observation window on each point, the mask were applied to the resulting flow map calculated using different window sizes, the resulting is plotted on (b). (c) The 1-SD ranges and the exact center contrast value (connected by line) are shown. Contrast values are beyond the range of 1-SD when the window size is 3×3 and 9×9.

Temporal speckle contrast images the time-integrated speckle and subsamples the temporal variation at 10 Hz or faster, thus it images all pixels in parallel but does not resolve the high-frequency temporal variation. The temporal speckle contrast K_t is obtained with the temporal standard deviation σ_t of the speckle intensity divided by the mean intensity. Both parameters are achieved from the statistics along n frames in the temporal dimension. By using temporal sampling to estimate the speckle contrast, rather than spatial sampling, the result can maintain a higher spatial resolution but at the expense of temporal resolution. The number of frame that is used to calculate the contrast remains to explore. We use the same data set as showed in Figure 3-10, and in Figure 3-12 the temporal contrast K_t to the number of frames n = 2 to 30 are plotted. It turns out that the contrast values become more stable when n increase after n = 16 (from frames 16-30) than after n = 10 (from frames 10-30). Practically the time of processing the data prolongs when a larger n is used, to gain a good balance between the time cost and the accuracy of the processed data, n = 20 is chosen in all the later data processing. To balance the advantage and disadvantage of spatial contrast and temporal contrast, temporal contrast was recruited in the later analysis since in the application of liver microcirculation in chronic fibrosis disease, the change may be subtle, a better spatial resolution is more important in analysis.

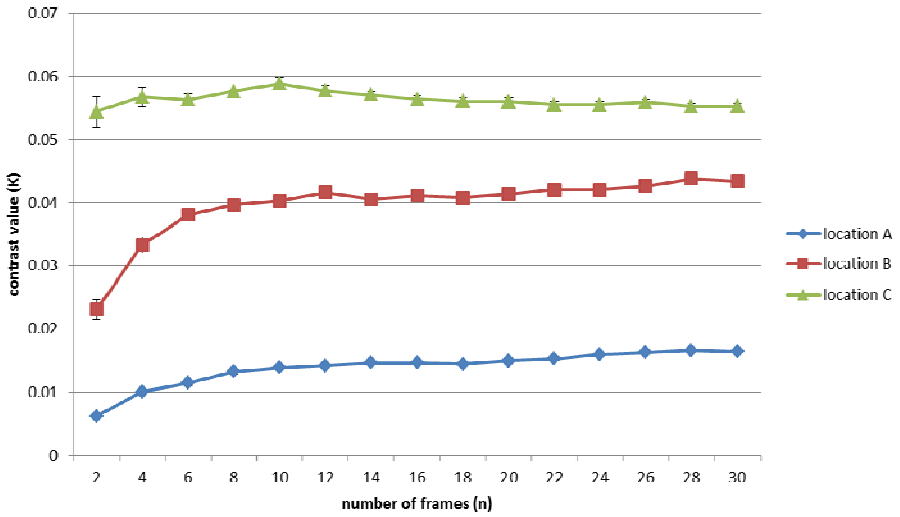

Figure 3-12. The contrast value calculated using temporal derived contrast over n frames. K(A) ~ 0.015225 (within 10% of each other after n = 10), K(A) ~0.015593 (within 8% of each other after n = 16); K(B) ~0.041807 (within 5% of each other after n = 10), K(B) ~ 0.042177(within 4% of each other after n = 16); K(C) ~0.056300 (within 5% of each other after n = 10), K(C) ~ 0.055701(within 2% of each other after n = 16); therefore, the contrast becomes more stable if use more than 16 frames to calculate.

3.3.3 The Histopathological findings from the tissue section of BDL model

The resulting effect of the BDL surgery is to artificially stop the bile flow secreted from the liver from entering into the intestine. The chronic obstruction of bile acid causes massive activation of myofibroblasts and ultimately results in fibrosis. BDL model is a mature animal model that simulates the progression of Primary Biliary Fibrosis/Cirrhosis. The progression of this model is also very similar to clinical disease Billary Atresia, which is a serious digestive disease affecting infants.

The time-related changes in liver after BDL are summarized in Figure 3-13. the acute injury to hepatocytes takes place in days 2-3. The cholangiocellular proliferation peaks at days 4-5. Acute injury was followed by continuous

tissue repair, showing as lymphocyte and Kupffer cell infiltration and the accumulation of collagen (144).

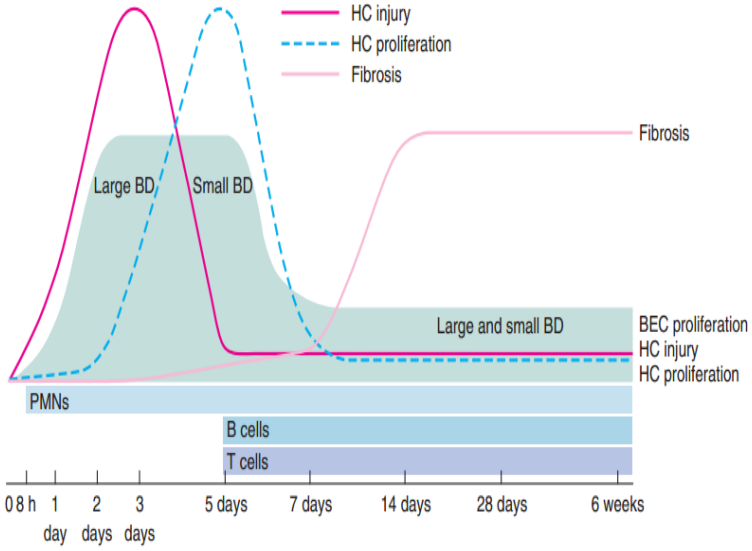

Figure 3-13. The overview of dynamic changes following bile duct ligation in mice. BD, bile duct; HC, hepatocyte; PMN, polymorphonuclear leucocyte (figure adapted from ref (144))

The most obvious feature from the HE staining is the substantial distribution of proliferated biliary epithelial cells (BECs) as shown on Figure 3-14(d) (black triangles), arranging in circles. This is because BDL introduces biomechanical stress to BECs and triggers the compensatory proliferation of BECs. Bile duct elongates inside the liver in a twist and winding style, and a single section of the tissue would yield multiple lumens in one plane. The proliferated BECs stem from the portal region and sprawl towards the central region. The portal tracts and sinusoids were gradually squeezed by the proliferated BECs, plus most necrotic hepatocytes are replaced by BECs, causing the difficulties of distinguishing portal tracks from central region and the drastic distortion of the vessel morphology as showed in Figure 3-14(d) (black arrow).

The MT staining shows extensively distributed collagen in the tissue collected 5 weeks after the BDL Figure 3-14(c) (collagen is stained in blue). Chronic obstruction of bile duct causes massive activation of myofibroblasts in the periductal region which is the basic feature of biliary fibrosis. With time going on and the accumulation of fibrosis becomes more and more substantial. When inspecting all the slides, we find the trend of collagen accumulation is from portal region to central region. Bridging collagen is obvious in the late stage of the BDL.

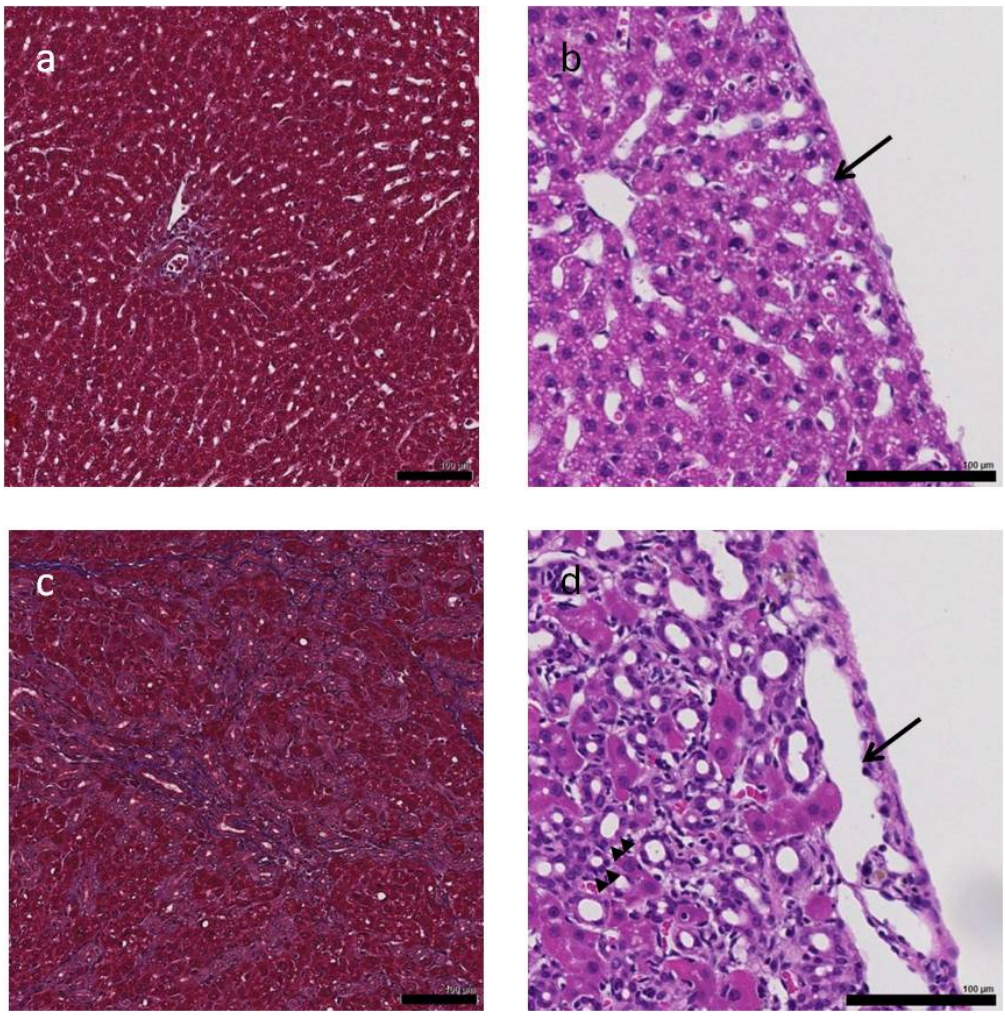

Figure 3-14. Histopathological comparison of the normal tissue (a, b) and tissue collected 5 weeks after BDL (c, d). (a) and (c) are MT stained, the blue color yields the distribution of the collagen. (b) and (d) are H&E stained. BECs are extensively distributed on week 5 BDL tissue (black triangles); the vessel morphology has changed drastically (black arrows). Scale bar: 100μm.

3.3.4 **Live image acquisition with the laser speckle and wide-field microscope**

In the following study, we will denote progression status of fibrosis using fibrosis score. Fibrosis was scored from 0 to 4 with score 0 denoting no fibrosis and score 4 denoting the most advanced fibrosis or cirrhosis. The representative wide-field fluorescence images and laser speckle contrast flow maps of liver at different fibrosis stages are displayed in Figure 3-15. Although in theory, most endogenous fluorophores could contribute autofluorescence, the signal in Figure 3-15(a) should be mostly ascribed to the flavins inside the hepatocytes; because flavins have the excitation peak at around 470nm and emission peak at 520nm, which is in conformity with the filter set used in our setup. Other fluorophores, such as NAD(P)H and vitamin A, are not effectively excited. This might cause the hepatic stellate cells to become invisible under the current setup. The vasculature showed on laser speckle contrast flow maps coincides with auto-fluorescence images. The complementation of the two modalities enabled us to comprehensively analyze the hepatic perfusion in terms of both morphological and flow speed features.

In Figure 3-15(a), all five imaging sites contain many pericentral sinusoids (around 15 um in normal state) and one to two central venules which multiple sinusoids are confluent with. If comparing the vasculature across the different stages of fibrosis, the most remarkable changes are dilated sinusoids radius and decreased sinusoids area. This finding is in agreement with previous research (12, 159). For normal livers, the sinusoids are radially spreading with the centre focused on the hepatic central venule. In fact, the liver blood flows through the sinusoids, where the nutrition supplying and the removal of metabolic products take place, then collects in central venula and later drains out of liver through bigger hepatic central vein. At earlier stages (stage 1 -

stage 2) of fibrosis, sinusoids seemed atrophic with sinusoids looked shrunken but the general pattern is mostly preserved. Multiple reasons could lead to this change, including the inflammation induced by detained bile acid that promotes the neutrophil accumulation, extravasation, and activation (160); the proliferation of biliary epithelia cells (BEC) (144) that take the space of sinusoids (black triangles in Figure 3-15(c)); and the collapse of the hepatocytes that destroy the structure of the sinusoids. The exact mechanism is beyond the scope of this study. Whereas from stage 2 to stage 3, the pattern of sinusoids changed more drastically, most previously atrophic sinusoids start to disappear, leaving large sinusoidal-free space, while the remaining micro-vessels, supposedly the central venula, have their diameters significantly distended. This change is similar to the microvascular change reported on fibrosis models induced by carbon tetrachloride (CCl_4) (12) , even though the etiologies are totally different.

The combining of laser speckle contrast technique with wide-field fluorescence microscope enables us the imaging capture and analysis of liver microvasculature (morphological) and dynamic information. Although the laser speckle contrast technique is a powerful technique in mapping the blood perfusion, the measurement of the absolute flow speed is impossible. The reason is that the physics of the scattering process is so complex and right now the relationship between the absolute flow speed and fluctuation of the speckle pattern is still not clear. Works will no doubt continue to find solutions to this problem. Therefore strictly speaking, this technique is a semi-quantitative technique. Besides, laser speckle contrast technique is purely 2D imaging of the superfacial flow, this is the limitation of this technique.

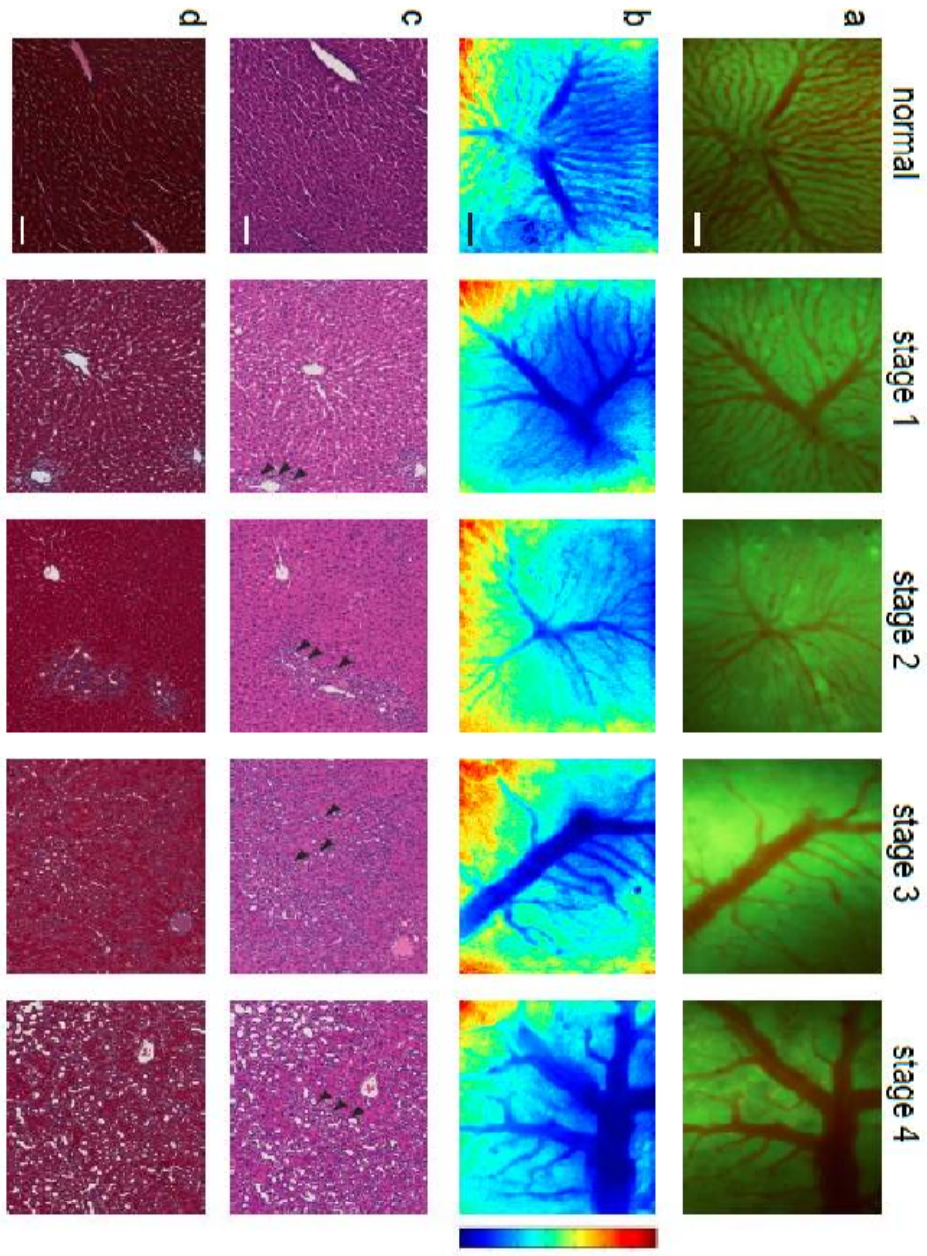

Figure 3-15. Wide-field fluorescence images and laser speckle contrast flow maps at different fibrosis stages. (a) auto-fluorescence images; (b) laser speckle contrast flow maps, the blue color indicates faster speed, the red color indicates slow speed; (c) tissue sections stained with Hematoxylin/Eosin; (d) tissue sections stained with Masson Trichrome. The black triangles indicate the proliferation of BECs. Scale bar: 100μm.

3.3.5 **Quantification of the four parameters**

The quantified results of four microcirculation parameters, namely number of junctions, average vessel breadth, vessel area and perfusion speed at different time point are shown in Figure 3-16. Generally, the number of junctions has decreased (Figure 3-16 (a)) with the progression of liver fibrosis, suggesting that the vasculature has simplified and distorted. This might be due to the detained bile inside tissue creating a toxic environment for hepatocytes, resulting in focal necrosis. At the same time the occlusion of bile acid induced the massive proliferation of bile duct epithelial cells, which took the place of the necrotic hepatocytes. The extinction of hepatocytes leads to the collapse of the tissue and the loss of sinusoids. Figure 3-16 (b) shows the increasing averaged sinusoid breadth. The parenchymal pressure might have increased due to the obstruction of the sinusoids, increasing the resistance for blood inflow and inducing the dilation of afferent vessel. The changing in the early stage is not statistically significant, only the increase from stage 2 to stage 3 is significant with $p<0.001$. In Figure 3-16 (c) we quantified the overall perfusion area within each image. The result shows that the overall perfusion area is vastly decreased with the progression of the fibrosis. This should be due to the loss of the sinusoids, because smaller sinusoids coalesce into very few larger vessel-like structures. Combining Figure 3-16 (b) with Figure 3-16 (c), the effect of sinusoids loss has surpassed the effect of dilation of the afferent vessel, so that the whole tissue is under-perfused due to the loss of micro-vascular capacity. Figure 3-16(d) reveals that the blood perfusion speed has dramatically increased in the remnant vessels. We speculate that the decreased overall vessel lumen together with the increased portal pressure (161) has pushed the blood volume into the remnant vessel with higher speed. This finding is consistent with the description of the ‘fast sinusoids’ in previous literature (12, 159).

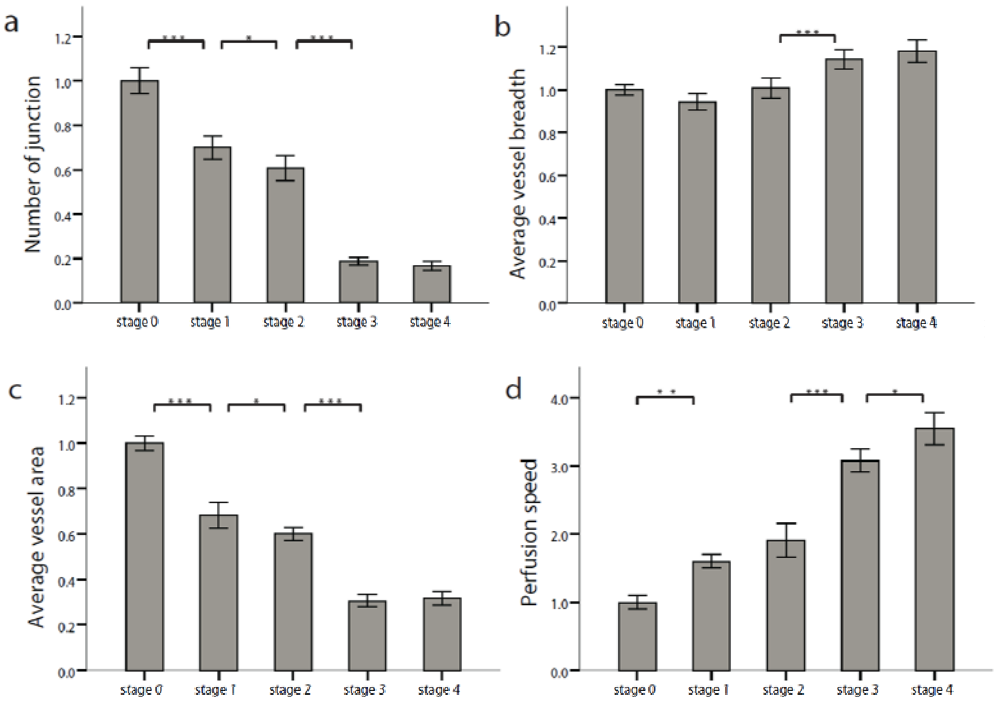

Figure 3-16. Quantification of four features extracted from the obtained auto-fluorescence images and laser speckle contrast images. With the progression of the liver fibrosis, (a) the number of junctions steadily decreases; (b) the average vessel breadth changes only from stage 2 to stage 3; (c) the average vessel area decreases steadily; (d) the perfusion flow rate map increases drastically. All the results presented are normalized to the mean of the stage 0 (normal). *** $p<0.001$, **$p<0.01$, *$p<0.05$

3.3.6 **Vessel cross-section speed comparison**

Cross-sectional intensity profiles of the speckle blood flow map from normal rat (Figure 3-17(a) and (b)) and end stage fibrotic (Figure 3-17(c) and (d)) rat are also compared. We manually chose three different locations in the main vessel from both normal and fibrotic images, and translate the intensity into relative speed based to the relationship between laser speckle contrast and speed. The calculated resulting speed of every pixel is plotted in the right panel. The flow speed curve of normal liver (A-A, B-B, C-C) along the cross section is more parabolic fitted, in contrast, the flow speed curve of the fibrotic liver (D-D, E-E, F-F) are prone to fluctuate more seriously. We

speculate the reason of this to be the imbalance between the increased portal pressure and the decreased resistance, which has deprive the hepatic microcirculation system of the normal fluid behavior.

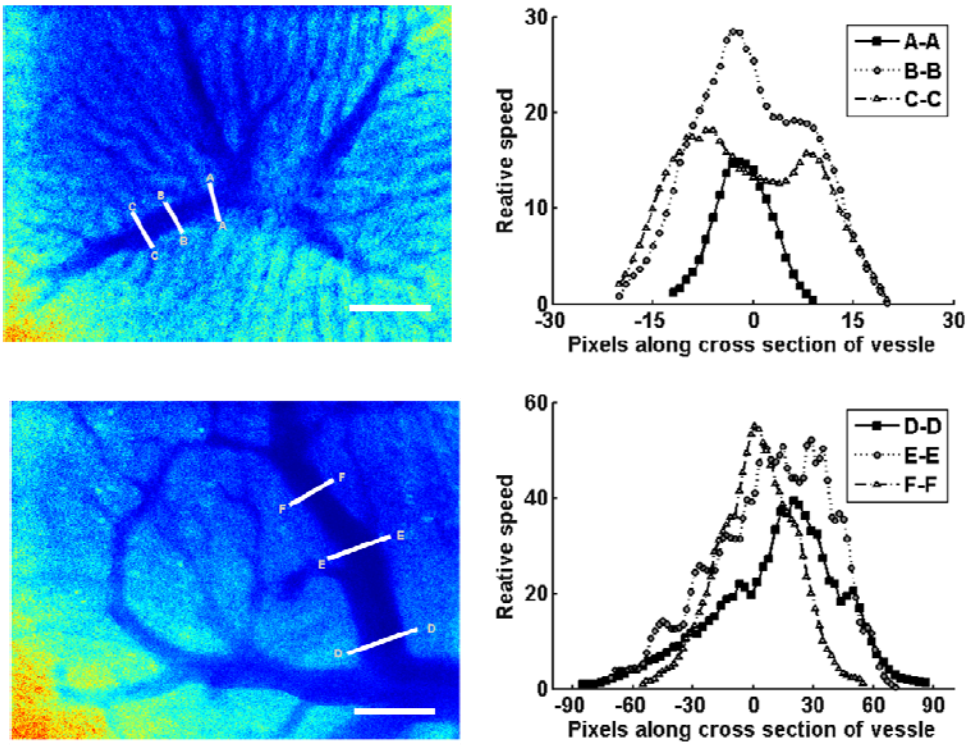

Figure 3-17. The cross-sectional speed of main vessel of normal liver (a and b) and end stage fibrotic liver (c and d). The sections are manually chosen as indicated as white line. The pixel intensity of the pixels on the line are translated into speed and plotted on the diagram on the right panel. Scale bar: 100μm.

3.3.7 **The onset of the microcirculation lesion is the early to middle fibrosis**

While the vessel average breadth is not changing constantly through the fibrosis progression, we exclude it in further ROC analysis in assessing features' ability of detecting every stage of fibrosis. The ROC analysis result is showed in Figure 3-18. The larger area under the curve (AUC) indicates the better sensitivity and specificity in differentiating certain stages. An AUC of 0.5 represents a random classification. All three features perform well in

detecting fibrosis from normal (stage 0 vs. stage 1, 2, 3, 4) and in detecting significant fibrosis from insignificant fibrosis (stage 0, 1, 2 vs. stage 3, 4) with AUC larger than 0.95. However, all three features have weak ability in detecting end stage fibrosis (stage 0, 1, 2, 3 vs. stage 4). This result suggested that, the drastic change of microcirculation takes place mainly in the early to middle stages of fibrosis in this model, preceding the accumulation of vast amount of the collagen (stage 4). The alteration of microcirculation results in progressive restriction of blood-liver exchange as a secondary injury to obstructive cholestasis contributing to liver fibrosis progression.

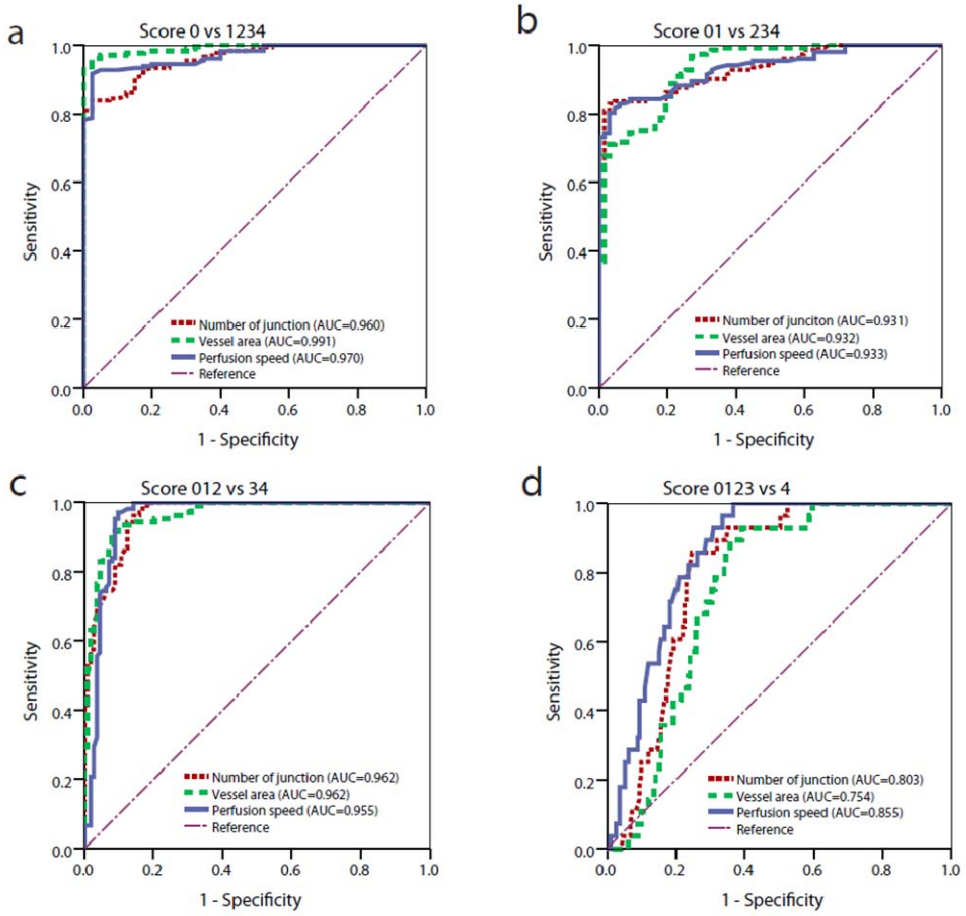

Figure 3-18. The receiver operating characteristics (ROC) curve analysis of the three selected features to demonstrate the performance of each feature in differentiating fibrosis stages. All three features perform worse in detecting the end stage fibrosis, suggesting the feature changes take place in the early and middle stage of fibrosis.

3.4 Summary and conclusions

In this chapter, we start with the design and validation of intra-vital imaging window for in vivo liver imaging. The establishment of the dual modality microscopy combining wide-field microscope and LSCI was then described in detail. Its ability of quantitatively detecting hepatic microcirculation lesion without labeling has been demonstrated on a rat obstructive cholestasis induced liver fibrosis model. By extracting four microcirculation related features from the resulting images, including increased radius of sinusoids, decreased perfusion area, changed pattern of vasculature and increased blood perfusion speed were revealed, significant microcirculation lesion has been observed in the early to middle stage of fibrosis. Because hepatic microcirculation lesion is a good indicator of early stage liver disease, detection of hepatic microcirculation lesion would shed light on the progression of the disease. We also envision further development of this bimodal imaging method to monitor the liver disease progression for drug screening on an animal model.

In this chapter, we have demonstrated the correlation between the microcirculation features and the staging of fibrosis. During the experiment, we use the histological score to denote the staging of fibrosis. Our experiment results show the microcirculation features already have a significant change from normal to stage 1. However, according to our prior knowledge, the collagen is accumulating drastically from stage 3 to stage 4. We therefore infer that the change of microcirculation features precede the change of collagen and maybe even other features. To prove this inference, we need to further explore other surface features that can be quantified and denote the disease progression. Therefore, in the next chapter, we will explore quantitative structural surface features to denote the disease progression.

Chapter 4 Study of Liver Surface Structural Features Related to Liver Disease status

4.1 Introduction

In this chapter, we aim to look for quantitative liver surface structural features that related to the disease status. The modality used here is nonlinear intravital microscopy. Intravital imaging using nonlinear microscope has been extremely successful in skin microvascular (162), neurophysiology (104, 163) and cerebroma research (164, 165), owing to ingenious design and application of dorsal skin / brain window. However, intravital liver investigation using imaging window is still limited, because of the opacity of the liver tissue and the existence of profuse blood in liver. With the development of nonlinear two photon intravital microscope with deep-penetration ability (103) in recent decades, there are some study of liver using two photon microscope (112, 147). However, rare studies focus on the structural features of the liver surface. Structural features on the liver surface reflects functioning changes of the liver in pathological status (77, 166). The ability to visualize these features with micrometer-scale resolution is therefore significantly important for both physiological studies and disease diagnosis of the liver. Although several methodologies have been proposed to probe liver (167, 168), the major limitation remains the absence of label-free and high-resolution methods that provide a fast quantitative visualization of various surface features in the native microenvironment of the living tissue. Therefore, our goal is to establish the methodology to visualize the structural feature on liver surface with high resolution but label-free.

In this part of study we used nonlinear two photon microscopy to obtain the detailed structural and functional information from liver surface at cellular and sub-cellular level. Two photon microscopy relies on the nonlinear excitation of fluorescence molecules or the induction of second harmonic generation. To brief its principle: two near infrared wavelength photons interact simultaneously with a molecule or structure in the sample, resulting in the emission of the one photon in visible range. Since the signal generation in two photon microscope occurs in a confined volume, it has the three dimensional sub-cellular spatial resolution. Particularly, Longer wavelength excitation allows deeper penetration compared to confocal microscope (169). Besides, two photon signals and second harmonic signals can be obtained by using the same excitation wavelength but separate detectors to visualize several intrinsic sources of contrast (170), which means this method posses multimodal capability. Previous studies have shown the use of two-photon excited fluorescence (TPEF) for visualizing the distribution of intrinsic components such as reduced pyridine nucleotide (NAD(P)H), oxidized flavoproteins (Fp), elastin, and so on (171-173). Second-harmonic generation (SHG) has been proven to be a sensitive probe of the structural organization of collagen in tissues (174-176), therefore it is an effective approach for imaging collagen fibers in the liver.

Using nonlinear two photon microscope, we have developed a label-free, three-dimensional quantitative and sensitive method to visualize various structural features of liver surface in living rat. We created the liver disease model by BDL surgery, because it is a well-established experimental animal model of extrahepatic cholestasis. In the experiment, we compared the obtained TPEF and SHG image from the normal liver and the liver at 5 weeks after BDL surgery. Using imaging processing techniques, we quantified

micro-structural features of liver surface with respect to the sinuosity of collagen fiber, and the ratio between elastin and collagen and the redox index. The results confirmed the ability of the methodology and this study highlights the potential of this technique as a useful tool for pathophysiological status studies and diagnosis of liver disease with further development.

The developed methodology also provides a good approach to explore imaging markers that related to hepatic inflammation. Hepatic inflammation is an important feature for the early phase of chronic liver disease. The detection of tissue inflammation mostly counts on blood test or immunohistochemical method, and little research is about the imaging marker of liver surface that related to hepatic inflammation because of the difficulty in specifically labeling and visualization of Kupffer cells and neutrophils. At the end of this chapter, we discussed the future study of the using the developed methodology and animal model to study the imaging marker of hepatic inflammation.

4.2 Materials and methods

4.2.1 Animal preparation for in vivo imaging

In this experiment, we created the liver disease model by conduct BDL surgery. The procedure of BDL surgery has been described in the last chapter. The rats after BDL surgery are used at week 5 as the disease group. Normal rats are used directly for imaging as control group. Each group has 5 rats to maintain statistical meaning in the later quantification. The procedure of preparing animal for intravital microscope investigation has also been described in detail in the last chapter.

4.2.2 Nonlinear microscope and image acquisition

The nonlinear optical system is achieved as described previously (77). The setup of the nonlinear two photon microscope we used for experiment is showed in the Figure 4-1. The microscope setup is based on a commercial laser scanning microscopic imaging system (Zeiss LSM 510 META, Jena, Germany) coupled to a femtosecond Ti: Sapphire laser (Mai-Tai broadband, Spectra-Physics). The wavelength of the output laser is set at 810 nm for the in vivo experiment. The laser passes through a pulse compressor (Femtocontrol, APE GmbH, Germany) and an acousto-optic modulator (AOM) for group velocity dispersion compensation and power attenuation respectively. The polarization direction of the laser beam is the horizontal polarization. Oil immersion objectives (40×, NA = 1.3 and 60×, NA = 1.4, Carl Zeiss) are employed for focusing the excitation beam into tissue samples (average power at the sample is around 10 mW) and are also used to detect the intrinsic TPEF and SHG signals. The detection of the signal is using the Photomultiplier tube (PMT), Hamamatsu R6357, Japan). In the experiment, three detection channels are used: two channels (430-490 nm and 500-560 nm) are used to

collect TPEF signals, whereas another channel (390-410 nm) is used to record SHG signal. These three channels recruit the same system parameters, including laser power, detector gain, amplifier gain and amplifier offset. To change and record the focus position, a fine focusing stage (HRZ 200 stage, Carl Zeiss) is used. The images are obtained at 2.56 μs per pixel. Two-photon images are recorded from the capsular and sub-capsular regions of liver surface. For each rat, the preparation and in vivo imaging is completed within 2 hours as required by the animal experiment protocol.

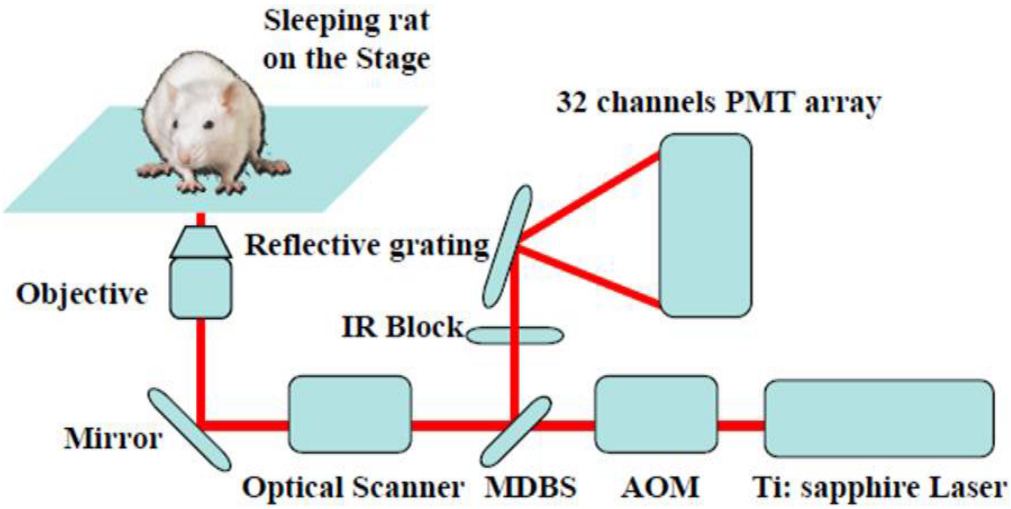

Figure 4-1. Schematic illustration of the optical configuration. Excitation laser is a tunable mode-lock laser (710nm-990nm, set as 810nm for in vivo experiment) with a pulse compressor (PC, not shown in diagram) and an acousto-optic modulator (AOM) for power control. The laser beam goes through a dichroic mirror, optical scanner and an objective lens. The emitted TPEF and SHG signal from the liver goes back through objective and goes to the reflective optical grating after descanned.

4.2.3 **Feature extraction and quantification**

To further quantify the images acquired from the liver surface, we perform quantitative analyses. All the image processing and computation mentioned here are carried out with MATLAB (the MathWorks Inc, Massachusetts). The methods we used to perform the quantification are as follows: firstly, five 225 μm by 225 μm rectangular areas are randomly selected on every image we took as the data pool. Using these data, we calculate sinuosity of collagen fiber,

collagen percentage and the redox ratio. The definitions of the three parameters are defined as below:

1. Sinuosity of collagen fiber is a measurement of curvature of the collagen fiber. In each rectangular area, the curvilinear length (along the fiber) is defined as *a* while the distance (straight line) between the two end points of the fiber is defined as *b*. The sinuosity of collagen is defined as *a*/*b*.
2. Collagen percentage is determined by counting the ratio of the SHG pixels over the whole image pixels. By this definition, collagen increase results in a larger collagen percentage value.
3. Redox ratio of the cell is an common measurement of the metabolic status of the cell (177). The pixel intensity of NAD(P)H on the images taken from spectral band 430-490 nm and the pixel intensity of Fp on the images taken from spectral band 500-560 nm were defined as *a* and *b* respectively. The Redox ratio is defined as *a*/*b*.

We also define another feature named elastic fiber structure. It was analyzed by using the gray-level co-occurrence matrix (GLCM) module (178). This module examines texture features based on the spatial relationship of pixels, it characterizes the texture of an image by calculating how often pairs of pixel with specific values and in a specific spatial relationship occur in an image. The basic step of using this module is to create a GLCM first based on raw image, and then extract statistical measures from the matrix. It can be achieved by using the MATLAB functions graycomatrix and graycoprops.

4.3 Results and discussions

4.3.1 Liver surface in vivo imaging using two photon microscope

Here we demonstrate firstly the in vivo liver surface imaging using nonlinear two photon microscope. The rat we used here is a normal 12-week-old Wistar rat. The rat with the window installed is stably accommodated onto the microscope stage of the nonlinear two photon microscope. The setup of the two photon microscope has been described in last section. The resulting images are showed in Figure 4-2. We took the z-stack with 2 μm interval. In the figure, we only showed the image as deep as 14um but in fact we were able to obtain satisfying image result as deep as 38 μm in this experiment without changing the PMT voltage. Beyond 38 μm, the signal becomes weak, the PMT voltage has to be increased. Practically, according to my experiment experience, the system could achieve a penetration depth of 100 μm. Although this depth is still smaller than the 1000um depth claimed by the Theer et.al (179) in the imaging of animal brain using two photon, it is deeper than any other modalities in liver in vivo imaging used currently, considering the opacity property (liver is heavily pigmented tissue) of the liver organ. The profuse red blood cells inside the liver could also increase the scattering of both the excitation and emission photons. Besides the property of the tissue, the maximum penetration depth depends largely on the laser power and the detection efficiency. Our system uses descanned detection scheme, in which the fluorescence signal returns through the scanning system before reaching the final detector. We believe this detection scheme is less optimized than non-descanned detection scheme in collecting scattered fluorescence signal. To fully take advantage of the two-photon excitation technique to achieve deep penetration, the non-descanned detection scheme is suggested to use.

The image resolution of the two-photon microscope is actually not better than that achieved by a confocal microscope because of the use of the longer excitation wavelengths. To estimate the lateral and axial resolution of the two-photon excitation microscope, we use the resolution equations for confocal microscope to estimate that of two-photon excitation microscope:

$$r_{xy} = \frac{0.46\lambda}{NA},$$

$$r_z = \frac{1.4n\lambda}{NA^2},$$

where r_{xy} and r_z represent lateral resolution and axial resolution separately, λ is the wavelength, NA is the numerical aperture of the objective. According to the equation the lateral resolution is 0.29 μm, the axial resolution is 1.08 μm.

To generate SHG signal, the sample object must contain certain material that has specific molecular orientation, so that the incident light could be frequency doubled. Some biological materials are highly polarized. For example, collagen in liver tissue, especially collagen type I and type III (180) is an efficient sources of SHG signal because of its noncentrosymmetric structure (174, 175), so the resulting SHG (the detection filter is band pass 390-410 nm) images in the first column of Figure 4-2 results from type I and type III collagen. Liver surface is covered by an around 10 μm thick collagenous layer called the Glisson's capsule (75), and from the figure, we see it generate strong SHG signal (from d = 2 μm to d = 6 μm). With depth goes deeper and deeper, SHG signals becomes less and less, because the collagen distribution within the normal liver is scarce. From previous studies of liver structure (77), we know that TPEF image is suitable for hepatocytes morphology observation, because when excited with a femtosecond pulsed laser, intrinsic molecules inside hepatocytes, such as NAD(P)H and Fp, emitted substantial fluorescence. The second column of Figure 4-2 shows the distribution of

TPEF signals (the detection filter is band pass 500 -560nm). The boundary of the hepatocytes is clear as well as the location of the nuclei which is shown as dark ellipsoid. The brighter red signal inside hepatocytes shows the bile canaliculi, which is the conduit for bile secretion. The autofluorescence of bile ascribable to bilirubin could also be excited by two-photon laser, and its emission range is 510-600nm (181).

To demonstrate the ability of two photon microscopy in liver in vivo imaging, other than the autofluorescence imaging of the liver, we have also explored the in vivo imaging using nonlinear two photon microscope when introducing external contrast agent. Figure 4-3 showed the hepatic microcirculation of live rat in a normal state and five weeks after BDL surgery. The microcirculation is highlighted with Rhodamine B dextran injected through jugular vein. From the image, there is drastic difference of the microvasculature between the two. The image was taken using a 10× objective lens, so that the field of view has covered a hepatic lobule that contains few portal regions and a central region. Figure 4-4 shows the labeling of both microcirculation and nucleus. The nucleus is labeled using BrdU. As BrdU incorporated into DNA during synthesis phase of the cell cycle, the staining also serves as a marker for proliferation.

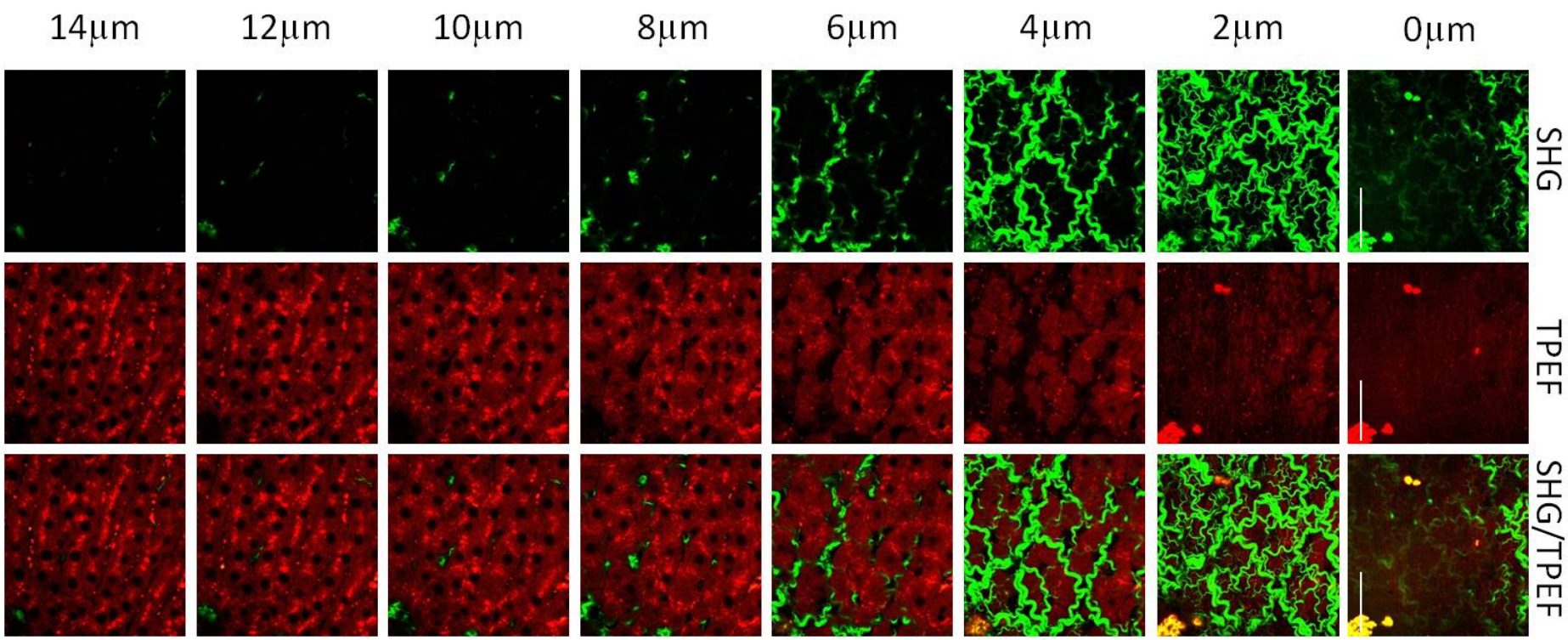
14μm
12μm
10μm
8μm
6μm
4μm
2μm
0μm
SHG
TPEF
SHG/TPEF

Figure 4-2. The liver in vivo imaging using nonlinear two photon microscope. The first column is SHG signal resulted from collagen (type I and type III), the second column is TPEF signal resulted from the intrinsic molecules such as NAD(P)H, Fp and bilirubin. The third column is the overlay of both channels. The images are taken as a z-stack with 2 μm interval; the deepest signal actually comes from 38μm (not shown). The size of the field of view is 150μm x 150μm, scale bar: 50μm.

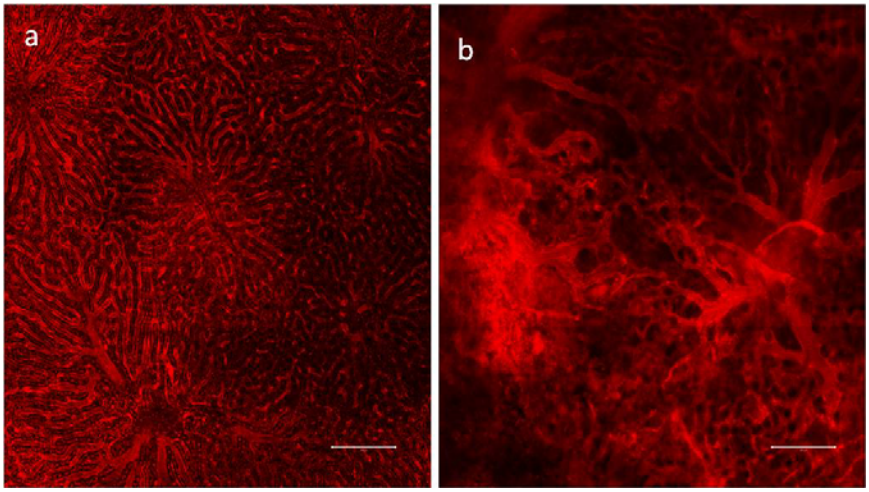

Figure 4-3. The image of hepatic microcirculation of normal rat (a) and BDL rat after 5 weeks (b). The external contrast agency Rhodamin B dextran was injected through the jugular vein of the rat to highlight the microcirculation. Scale bar 200μm.

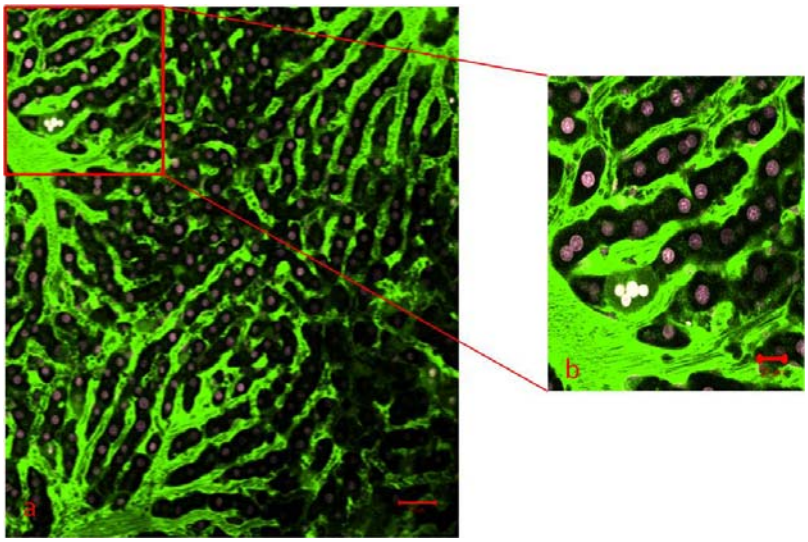

Figure 4-4. The in vivo labeling of microcirculation and hepatic cell nucleus in a normal rat. The microcirculation is assigned with green color; the nucleus is in purple color. The enlarged region showed in (b) indicates the proliferation of hepatocytes which shows double nucleus. The scale bar in (a): 50μm, the scare bar in (b): 20μm.

4.3.2 **Structural features of liver surface**

During the imaging using two-photon microscope, we noticed the emission of TPEF signal from the liver is very wide (from 430 nm to 560nm) under the excitation of 810nm laser. We hereby separate the detection spectrum to two bands (430-490 nm and 500-560 nm) for better analysis of the metabolic status of the hepatocytes. The reason for doing so is that different molecules will show different emission spectrum, in this way we could separate the signal from different molecules. In the capsular layer (from liver surface to around 10 um depth) TPEF falls in both 430-490 nm and 500-560 nm spectrums mainly results from the elastin, whereas in the subcapsular layer TPEF signals within 430-490 nm originates mainly from NAD(P)H and the TPEF signals within 500-560 nm signal arises mainly from Fp (170, 171).

In the following figures, we show the representative multiphoton images from *in vivo* normal (Figure 4-5) and diseased rat livers (Figure 4-6) at two different depths (capsular and subcapsular layers). For the purpose of distinguishing the SHG and TPEF signals, pseudocolors of grey (SHG: 390-410 nm), green (TPEF: 430-490 nm), and red (TPEF: 500-560 nm) were assigned. Comparing Figure 4-5 and Figure 4-6, several interesting results are discovered. Firstly, when comparing the morphological pattern of collagen and elastin, we find that in the normal capsular region collagen is dense with curvy subfilament structures and elastin displayed a fine structure with visible fibers, whereas in the diseased liver, capsular region collagen is less dense and straight with loss of curvy subfilament structures and elastin shows a breakage of fine structure with merged fibers. Second, in comparison with the normal capsular region, the diseased capsular region has an alteration in the proportions between collagen and elastin, as obviously shown in the combined SHG & TPEF figures. Third, in the normal subcapsular region there are well-organized

hepatocytes and only a little collagen is presented; whereas in the diseased subcapsular region there are some hepatonecrotic areas because of bile duct proliferation and some abnormal collagen, a clear indication of fibrosis, is also presented. Last, in the subcapsular region, the abnormal hepatocytes display the color of pale yellow, whereas the normal hepatocytes exhibits a more green, as seen in the combined SHG&TPEF figures. Because green and red can give yellow, the pale yellow color indicates that the proportion of Fp signals (red) increases in abnormal case, while a more green appearance reflects that the proportion of NAD(P)H signals (green) is higher in normal case. In other words, the abnormal hepatocytes show a lower redox ratio, whereas the normal hepatocytes display a higher redox ratio.

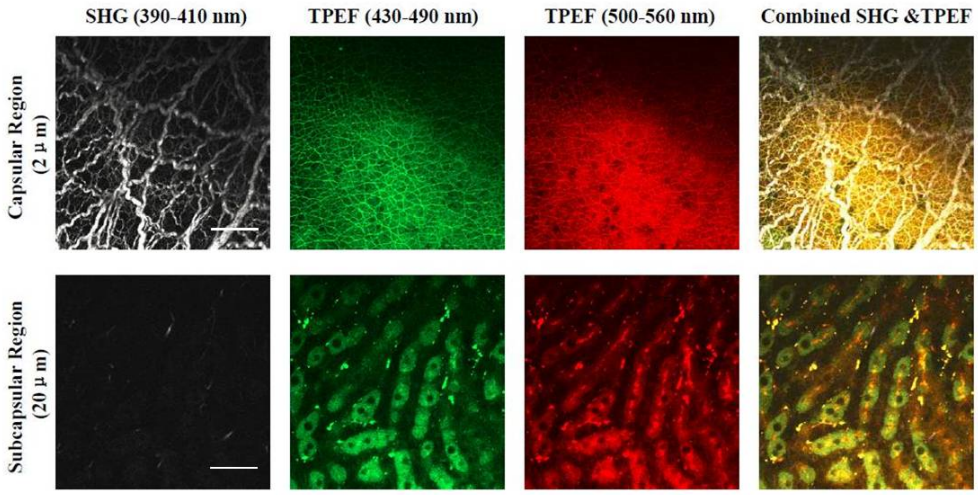

Figure 4-5. Representative two photon images acquired from in vivo normal rat liver. Four columns from left to right: SHG, TPEF detected at 430-490nm, TPEF detected at 500-560nm and combined SHG and TPEF images. Two rows from top to bottom: capsular region (d = 2μm) and subcapsular region (d = 20μm). The excitation wavelength is 810 nm. The size of field of view is 225μm × 225μm. Scale bar: 50μm.

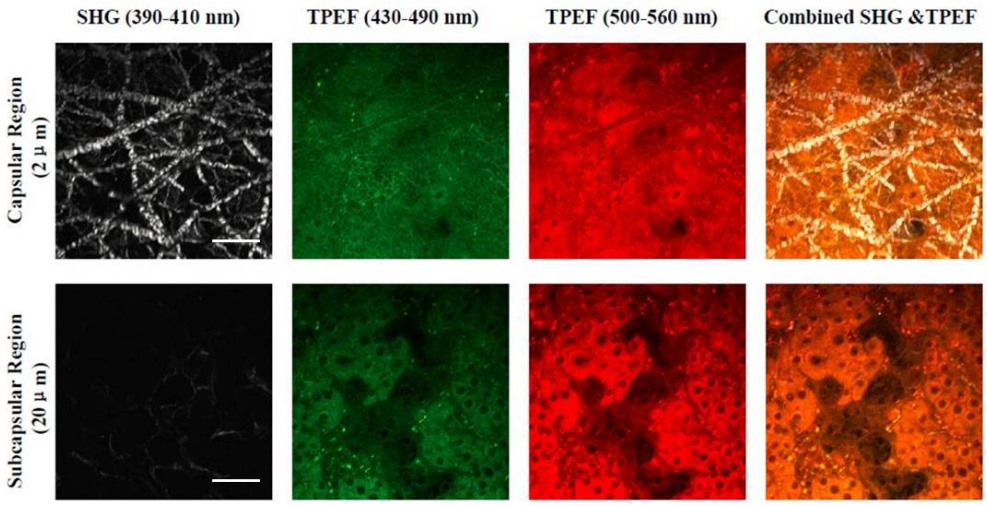

Figure 4-6. Representative two photon images acquired from in vivo diseased rat liver. Four columns from left to right: SHG, TPEF detected at 430-490nm, TPEF detected at 500-560nm and combined SHG and TPEF images. Two rows from top to bottom: capsular region (d = 2μm) and subcapsular region (d = 20μm). The excitation wavelength is 810 nm. The size of field of view is 225μm × 225μm. Scale bar: 50μm.

In specific interest in the quantitative comparison of normal and diseased liver as mentioned above, we use the quantification method as detailed in last section. Presented in Table 4-1 are the quantified results of five parameters, namely sinuosity of collagen fiber, elastic fiber structure, ratio between elastin and collagen, collagen percentage and redox ratio from *in vivo* normal and diseased rat livers. As showed in the table, all the five parameters are significantly different between normal and diseased rat livers. Sinuosity of collagen fiber is a parameter for the morphological shape of the collagen. It was found that the sinuosity of collagen fiber of normal rats is significantly higher than that of abnormal rats. Specifically, it is 1.50±0.13 for normal rats and 1.26±0.06 for diseased rats. This observation is in conformation with the notion that BDL surgery leads to higher expansion force in the liver surface, which cause straight collagen fibers. This could also link to the increased stiffness of liver tissue during the progression of liver fibrosis, which lays the basis for application of elastography for liver fibrosis measurement (182).

In our quantification using the gray-level co-occurrence matrix (GLCM), the correlation value at the distance of 30 pixels is defined as the elastic fiber structure. In this definition, a loss of fine structure leads to a bigger elastic fiber structure (EFS) value. Based on our quantification, the EFS for normal rats is 0.26±0.07, whereas for diseased rats it is 0.59±0.10, suggesting the loss of the fine elastic fibril structure in BDL rats. Moreover, we analyzed the ratio between elastin and collagen. Generally, in the capsular layer, the SHG signal reflects the collagen content and TPEF signal signifies the distribution of elastin (176, 183), we performed the analysis to cauculate the ratio of SHG (390-410 nm) signal and TPEF (430-560 nm) signal. The ratio for normal rats is 1.72±0.17, whereas for diseased rats it is 2.51±0.23, suggesting increased amount of elastin in BDL rats. This result also confirms the results from previous research that there is the regulation of elastin secretion and turnover after BDL (184). Finally, to analyze the subcapsular layer images, we quantified the collagen percentage. It is calculated as the percentage of SHG signal pixels to the pixels of whole image. As showed in the table, the collagen percentage for normal rats is 0.005±0.001 and for diseased rats it is 0.023±0.006, reflecting collagen increase in BDL rats. The increased amount of collagen is in agreement with imaging study using in vitro fibrotic liver tissue (77).

Table 4-1. Quantitative characterization of parameters derived from two photon imaging

	Capsular Layer			**Subcapsular Layer**	
	SCF	EFS	REC	CP	RR
Normal	1.50±0.13	0.26±0.07	1.72±0.17	0.005±0.001	1.24±0.12
Diseased	1.26±0.06	0.59±0.10	2.51±0.23	0.023±0.006	0.38±0.05

SCF: sinuosity of collagen fiber; EFS: elastic fiber structure; REC：ratio between elastin and collagen; CP: collagen percentage; RR: redox ratio. Data is represented as mean±s.d..

4.3.3 **Redox ratio indicates hepatocytes function**

The ratio of NAD(P)H over Fp fluorescence intensity, called the redox ratio, is a good indicator of the cellular metabolic status (171, 185, 186). In this analysis, we objectively selected regions where the cell boundaries can be identified and performed the redox ratio analysis to make sure the ratio is gained from the region of hepatocytes. For the diseased rats, a significant decrease in the RR is observed. Specifically, the redox ratio for normal rats is 1.24±0.12, and for diseased rats it is 0.38±0.05. This observation supports the notion that there is a decrease in metabolic activity in this model due to apoptosis of hepatocytes (187).

According to previous literature, the oxidation of NADPH induces the active neutrophils to generate superoxide. Superoxide dismutates to hydrogen peroxide and oxygen and thus easing the generation of neutrophile induced oxidant stress and cytotoxicity (186). This has related the redox status to the hepatic inflammation. We therefore hypothesize that the redox status is a surrogate of inflammation, but the demonstration of this hypothesis needs further experiment.

4.4 Summary and conclusions

In this chapter, we focused on looking for surface structural features that could potentially differentiate the liver disease status. We reported a label-free, three-dimensional quantitative and sensitive method for visualizing various components of liver surface in living rat using nonlinear two photon microscope. The ability of this method to extract label-free quantitative morphological features *in vivo*, including the sinuosity of collagen fiber, the elastic fiber structure, the ratio between elastin and collagen, collagen percentage and the redox ratio, could provide a direct method for researchers to compare pathophysiologically induced changes.

Currently, several commercialized two photon microscopic devices have demonstrated their application in clinic, including DermaInspect and MPTflex Multiphoton Laser Tomography from JenLab GmbH, Germany. Although to our knowledge, two-photon microscope integrated to the fiber endoscope has not yet seen commercialization, it is heavily studied as a hot research topic. Especially, Zhang et al. has prototyped the nonlinear endomicroscope and demonstrated its ability to visualize cervical remodeling during pregnancy (188). Thus, it is reasonable to predict that commercial development of the fiber based nonlinear endomicroscope may occur within the near future. For our developed method, I believe with the development of two photon endomicroscope (189-191), this method has the potential to become a useful tool for the physiological studies and disease diagnosis of the liver in the future.

Chapter 5 Study of Progression Mechanism of Non-Alcoholic Fatty Liver Disease

5.1 Introduction

NAFLD has become the main driver for the increased prevalence of chronic liver disease worldwide. It is also a risk factor for Hepatocellular Carcinoma (HCC). Yet its mechanism still requires clarification. Since NAFLD is a chronic liver disease that encompasses the non-alcoholic steatohepatitis (NASH), necroinflammation and progressive fibrosis. In the previous chapter, we have studied the fibrosis, in this chapter, we focus on steatosis by delineating the structural and biochemical features changes during the disease progression and in the mean time understand the mechanism of the disease.

Raman micro-spectroscopy has emerged as a promising clinical detection tools in recent years, especially for cancer diagnosis (192, 193). The signal of Raman micro-spectroscope results from the inelastic scattering of photons induced by the intrinsic molecular bonds. Because it has the ability to acquire rich biomedical information, it provides a good method to probe the progression change of the disease. The other reason of using Raman micro-spectroscopy to study steatosis is its ability to probe fatty lipid. Firstly, fatty lipid is difficult to store in the post-processing procedure of liver biopsy, due to its resolvability in organic solvent. Even though Oil red staining method is developed as a superior fat stain, it adds the work load to common H&E staining and prohibits a rapid assessment of structural tissue damage. Secondly, for in vivo application, only Raman spectroscopy, Coherent anti-Stokes Raman scattering (CARS) microscopy and Third Harmonic Generation imaging has the ability to probe fatty lipid. Among all three

modalities, Raman micro-spectroscopy provides a relatively simple and reliable method.

In this Chapter, we used the Raman micro-spectroscopy to image the fresh frozen tissue from the different time points of NAFLD diseased mice. The basic spectra change with the disease progression was analyzed. We used principle component analysis and biological component analysis to delineate the structural and biochemical feature changes. The results indicate the dominant role of fatty acid in the progression of NAFLD.

5.2 Materials and methods

5.2.1 Animal model for NAFLD and sample preparation

A good animal model that exactly reproduces the pathogenesis of NAFLD of human is not available, because the progression term may be as long as 20-30 years. In this experiment, we used the STAM™ Nash/fibrosis-HCC model developed by the Japanese company Stelic Institute & Co, Inc. This model is created by combining the effect of chemical toxic Streptozotocin (STZ) and high fat dietary on non-genetic C57BL/6 mice. It is featured by clear onset of NASH and a 100% development of HCC. Specifically, the model is developed by giving a low dose STZ injection subcutaneously when mice are two-day old, and starting to feed mice with high fat diet when 4 week old. The end point for the mice is 20-week old age, during which they will develop NASH, fibrosis and HCC finally. Its histological phenotype is quite similar to human NASH with peri-sinusoidal fibrosis and fatty lipid droplets accumulation.

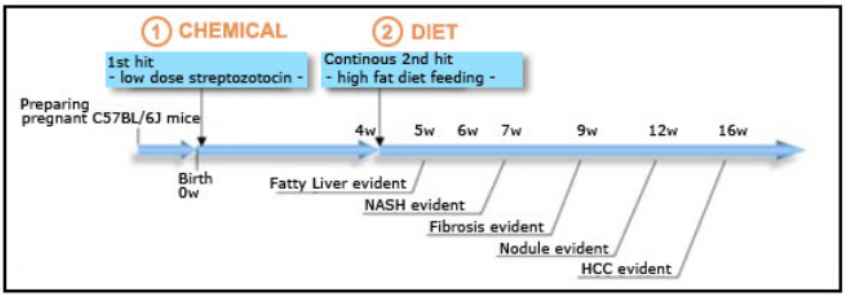

Figure 5-1. The STAM™ model for NASH-fibrosis/HCC, picture adapted from the official website of Stelic Institute & Co, Inc (http://stelic.com/nash/index.html).

In total, 46 cryo-preserved tissue samples have been purchased from the company, they are from 6 time points (Table 6-1). Each sample is from one mouse. The tissue is not chemically fixed but cryo-frozen preserved directly after it is harvested. The samples are then sectioned into 20um thick tissue

slides, the tissue is put on quartz glass slides for Raman imaging. Every consecutive three sections were separately stained with H&E, Oil Red and Sirius Red separately.

Table 5-1. The number of samples in each time point

Time point	Sample number
Week 4	8
Week 6	8
Week 8	8
Week 12	8
Week 17	8
Week 20	6

5.2.2 **Raman spectroscope and data acquisition**

The Raman spectroscope is based on the home-built inverted microscope. A frequency-doubled Nd: YAG laser with wavelength of 532nm (Millennia 5sJ, Spectra-physics) is used as the pump source of a CW tunable Ti: sapphire Laser with the wavelength of 785nm (3900S, Spectra-Physics). The collimated beam is firstly filtered by the laser line clean-up filter (BPF, LL01-785-12.5, Semrock) and directed by a dichroic mirror (LPD01-785RU-25, Semrock) to the dual-axis galvanometer mirrors (CT-6210, Cambridge Technology). Then the beam size is adjusted by a telescope and focused at the sample plane by the water immersion objective lens (Olympus UPLSAPO60XWIR 60X/1.20). Laser power at the sample location is around 3.5mW. The micrometer-controlled stage realizes the XY position. A piezo actuator combined with a differential micrometer (DRV517, Thorlabs) controls the course and fine adjustment of the sample focus. The inelastic scattering Raman signal is then delivered to the spectrograph (HoloSpec f/1.8i, Kaiser

Optical Systems), which is featured by high throughput and low aperture ratio. The Raman grating (HSG-785-LF, Kaiser Optical Systems) has the spectra shift coverage of -34 to 1894 cm^{-1} and the spectra resolution of 2.0 cm^{-1}/pixel. Spectra are captured by a liquid Nitrogen cooled CCD. An intensity controlled white LED is used as the illumination source for the bright field imaging, the picture is captured by the CMOS camera (BCN-B050-U, MightTex). Labview 8.2 software (National Instruments) and a data acquisition board (PCI-6251, National Instruments) are used to control the devices. The setup of the system is showed in Figure 5-2.

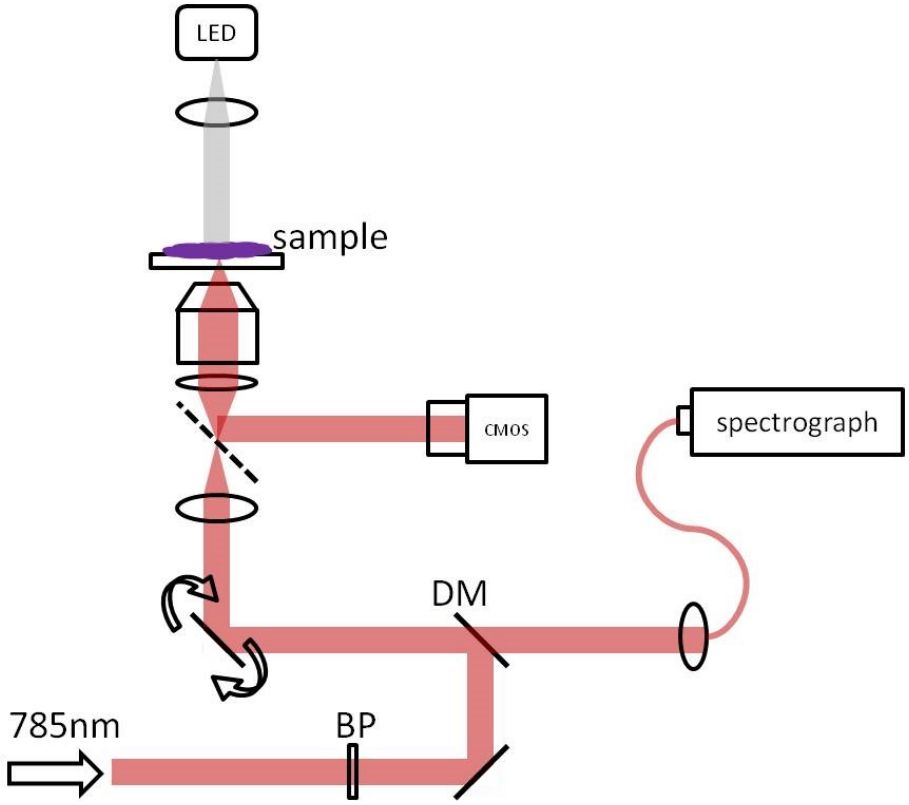

Figure 5-2. The schematic of home built Raman Spectroscope system. BP: bandpass filter. DM: dichroic mirror.

Two types of data have been acquired from the tissue slides. The first type is 30×30 high resolution spectral images. One image in this type is acquired from each tissue sample. This type of data is used for image based analysis. The second type is 10×10 low resolution spectral images. Nine images in this

type are acquired from each tissue sample. This type of data is used for spectral based analysis. The signal acquisition integral time is 1 sec, therefore each 30×30 spectral image would take around 20 minutes to get, each 10×10 spectral image would take around 2 minutes to get. In the later biochemical components analysis, we also acquired the spectra of different chemicals. To acquire the spectrum of the basic chemical, small amount of chemical powder was put on the quartz cover slip, the resolution was set as 3×3, but since no voltage was given to the galvanometer, the nine measurements were actually from the same point. The signal acquisition integral time is 10 sec. The spectra of basic chemicals were the averaged from the nine measurements.

5.2.3 **Data analysis**

The spectra were measured over the range of -175cm^{-1} to 1843 cm^{-1}, since the signal from the quartz substrate is mainly in the range of 250 cm-1 to 580 cm-1. The spectrum within the range of 600cm^{-1} to 1800cm^{-1} is selected for analysis. Data processing was performed using MATLAB (Mathworks, Massachusetts). The narrow spikes induced by cosmic rays were removed firstly, and then fluorescence background from the tissue was estimated and subtracted using the adaptive minmax method, the algorithm will be introduced in the next section. Finally the spectrum was smoothed before the subsequent analysis was performed.

5.2.4 **Tissue autofluorescence background subtraction**

Raman spectrum of tissue usually contains Raman scattering, intrinsic tissue fluorescence and noise. The removing of tissue background could effectively expose the Raman scattering for easier analysis of the basic chemical composition of the tissue. In order to achieve the fluorescence background subtraction, the method developed by Cao et. al. (194) has been adapted.

Based on their method, polynomial fits (195) are used with the consideration of the fluorescence-to-signal (F/S) ratio, to minimize the residual mean square (RMS) error. Here the F/S ratio is defined as the maximum fluorescence divided by the maximum Raman scattering signal, when the minimum intensity value is set as zero. The proposed method, named 'adaptive minmax method', contains two steps, the first step involves constrained and unconstrained polynomial fit for two consecutive orders, where the order is decided by the adaptive part of the algorithm based on the F/S ratio and can also refer to the empiric value listed in Table 5-2; the second step takes the maximum value among the initial fits as the points for the final fit. This method works better than others with minimized RMS error.

Table 5-2. Orders to be used in constrained/unconstrained polynomial fit

F/S range	Order of fit
(0, 0.2)	1^{st},2^{nd}
(0.2, 0.75)	2^{nd}, 3^{rd}
(0.75, 8,5)	3^{rd}, 4^{th}
(8.5, 55)	4^{th}, 5^{th}
(55, 240)	5^{th}, 6^{th}
(240, 517)	6^{th}, 7^{th}
(517, 1000)	7^{th}, 8^{th}

5.2.5 **Biological components analysis (BCA)**

The biological components analysis (BCA) is commonly used in Raman spectra analysis. The assumption behind this method is that the spectrum of tissue is the linear combination of the basic components' spectra, BCA method estimates the contribution of each component by using least square regression. This method has been applied in the tissue level study of breast cancer

diagnosis (116) and in cell level study of necrotic cells (196). To perform BCA analysis, prior knowledge of the constituents of the tissue is required.

For BCA, pure basic biochemical components, including saturated lipid acid, unsaturated lipid acid, collagen, glycogen, phenylalanine, NADH and 3-nitro-L-tyrosine were purchased from Sigma Aldrich (USA) and used directly. Raman spectra were measured from each chemical. To decompose the spectrum of the tissue, the least square regression method was adapted by using a linear curve fitting function lsqnonneg in MATLAB. This function finds the non-negative coefficients of all basic component spectra that best fit the tissue spectra.

5.2.6 **Principle component analysis (PCA)**

The principle component analysis (PCA) method is a non-parametric method that uses the orthogonal transformation to convert the data set that possibly correlated with each other into the linearly uncorrelated principle components. This analysis is widely used in Raman spectroscopy studies of biological sample to classify pathological features (197-199), because the classification of the spectral data could be easily achieved by choosing different combinations of principle components. The purpose of PCA here is to reduce the dimensions of a highly complex chemical system to a simpler system that has smaller number of principle components. The selected principle components effectively contain the important information of the spectra (200). However, PCA doesn't reveal chemically interpretable information of the tissue, it provides purely mathematically decomposed information that is abstract and broadly distributed in the data.

PCA is performed using princomp function in MATLAB on Raman spectra before and after the fluorescence background removal, the background is included in the analysis because it may contain important information. Before the PCA is preformed, the outliers greater than the 99 percentile were removed, the intensity level are standardized across all samples to ensure that all the samples within each wavelength have zero mean and a standard deviation of 1.

5.3 Results and discussions

5.3.1 Mean Raman spectra of tissue at different time points

After the spike signal removal, the spectrum in the range of 600cm^{-1} to 1800cm^{-1} was screened out. The data was carefully reviewed and corrupted data was excluded from the further analysis. Here the corrupted data is defined when the intensity of the spectrum is beyond the recording range of the spectrograph. After the preprocessing the mean Raman spectra of the tissue at different time points were plotted. Table 5-3 has listed the number of spectra for each time points.

Table 5-3. The number of spectra averaged in each time points

Time point	Sample size
Week 4	5237
Week 6	7021
Week 8	7084
Week 12	6184
Week 17	7075
Week 20	4350

Figure 5-3 shows the typical Raman spectra of the liver tissue at different time points. Obviously, the tissue Raman scattering is representing a smaller contribution to the intensity, while the intense autofluorescence background is quite strong and showing different level among different time points. The peak location of the Raman scattering is not changing too much after week 6. The difference between week 4 and week 6 onwards is because the diet has changed from normal diet to high fat diet from week 4 onwards, while the effect of diet change is still negligible when mice are sacrificed in week 4. After week 4, the intensity of the Raman scattering is supposed to have been

changing, therefore the next step is to remove the tissue fluorescence background to reveal the minor changes.

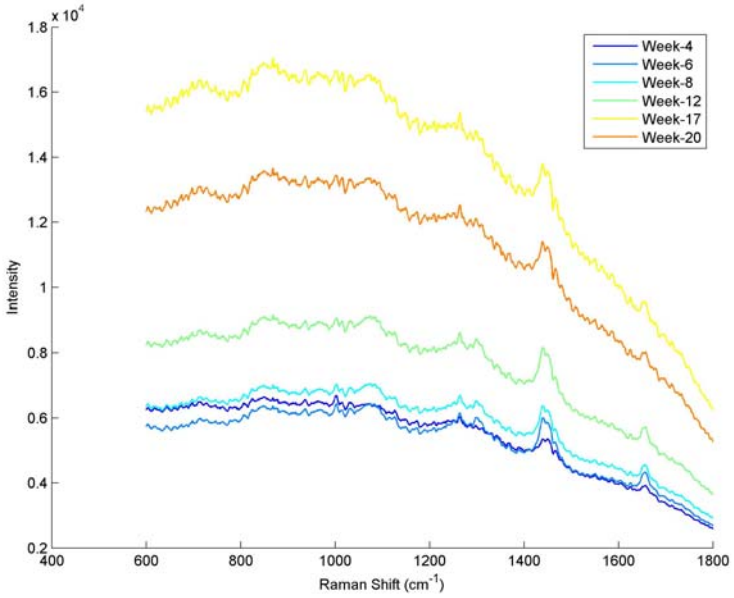

Figure 5-3. Mean spectra of the tissue of each time point. The spectra data have been corrected for the spectral response of the system.

Figure 5-4 shows the Raman spectra after the fluorescence background substraction as mean ± 1.96SD for six different time points. The variation of the overall spectral intensities is relatively higher for week 4 and week 20 tissue. This is reasonable considering the variability of the individual animal's reaction to the diet changing and producing tumor in the end stage of the disease. Besides, within each time points, the variation is relatively small in the range of 1200 cm^{-1} ~1700cm^{-1}, the reason for this requires further study.

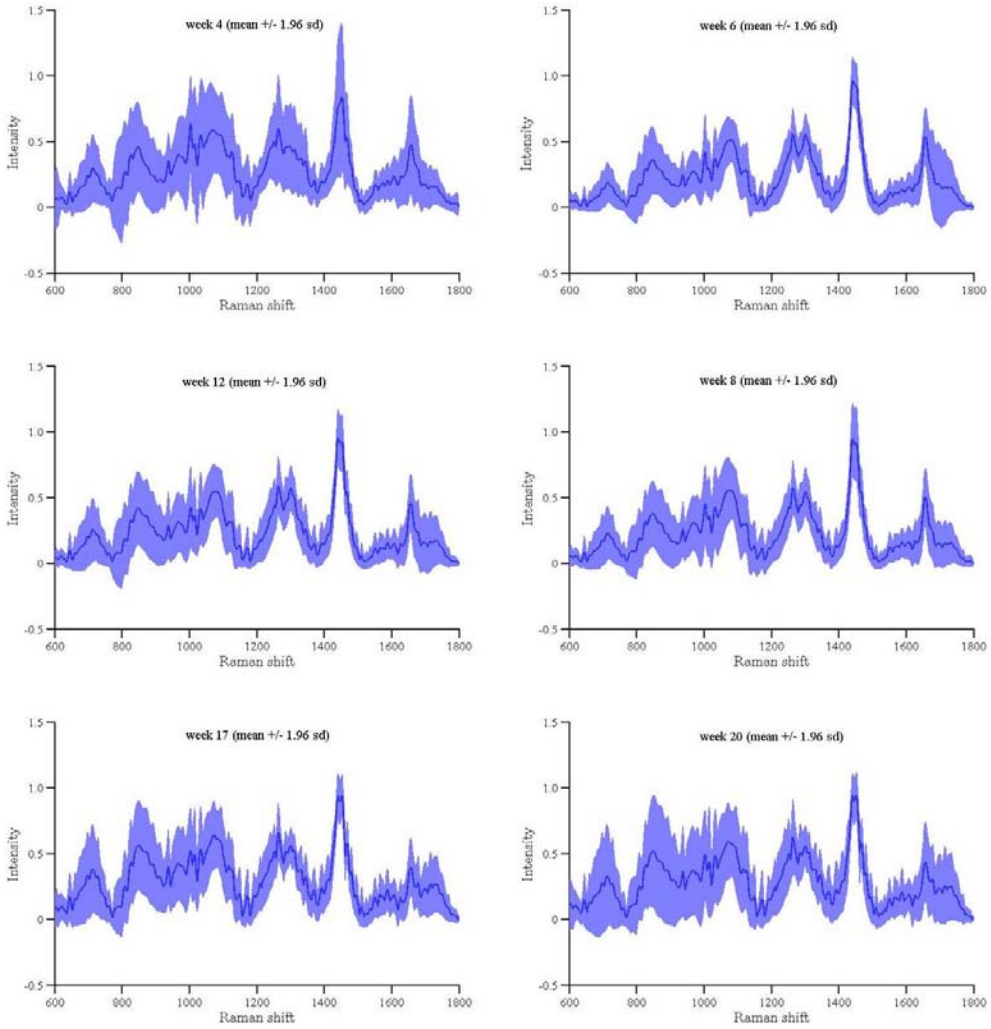

Figure 5-4. Mean Raman spectra after tissue fluorescence background subtraction (solid line) ± 1.96SD (shadow area) for tissue of six different time points.

Figure 5-5 displays the mean Raman spectra of six different time points in the single plot. Except for the week 4, the spectra of the other time points are showing almost identical patterns, most Raman peaks are exactly in the same frequency. The reason for big change between week 4 and the rest time points has been discussed earlier, which is the effect of the animal dietary change. From week 6 onwards, the peaks are exactly in the same frequencies, indicating that there should not be new biochemical components generated but

only the quantity of the existing components changed with the progression of the disease.

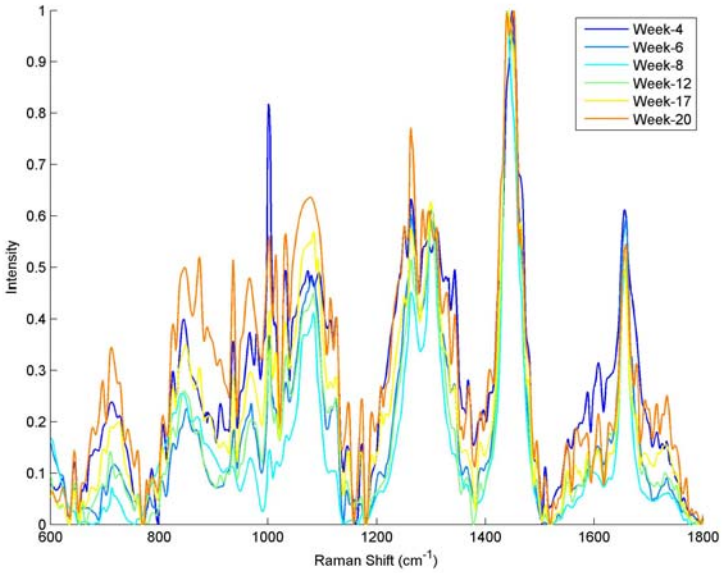

Figure 5-5. Mean Raman spectra after tissue fluorescence background subtraction in a single plot. Except for week 4, the spectra of the other five time points display almost identical patterns. The main peaks are all in the same frequency.

5.3.2 **Selection of basic chemical components**

Table 5-4 lists the basic biochemical components chosen for analysis. The reasons of selection are also listed in the table.

Table 5-4. The selected basic biochemical components and the reason of selection

Item	Biochemical components	Reason
1	Oleic acid	unsaturated fatty acid
2	Palmitic acid	Saturated fatty acid
3	Collagen (type I, II, III)	Main component inside liver, would increase quantity with fibrosis
4	Glycogen	Main form of energy storage
5	phenylalanine	Amino acid to form proteins

6	NADP/NADPH	Coenzyme in all living cells responsible for metabolism
7	3-nitro-L-tyrosine	Indicator of cell damage

Figure 5-6 shows the Raman spectra of the selected basic biochemical components. The spectra of oleic acid and palmitic acid are quite similar to the spectrum of liver tissue; it indicates the dominant role of the fatty acid in the liver with NAFLD. Oleic acid is a mono-unsaturated acid, which means it has only one double bound (C=C) in the fatty acid. During the experiment, we also measure the Raman spectrum of linoleic acid, which is a polyunsaturated acid, but the spectra of the two chemicals are identical (data is not show). Oleic acid's spectrum is featured by the peaks at 1266 cm^{-1} and 1655 cm^{-1}, both of them are corresponding to the double bond (C=C). Palmitic acid is featured by the peak at 1302 cm^{-1} and 1446 cm^{-1} (201). These two peaks are attributed to CH_2 stretching mode. The Phenylalanine is featured by the peak at 1004 cm^{-1} corresponding to the C-C stretching (202). The captured peak at 830 cm-1 of Tyrosine is attributed to the phenol ring modes (203).

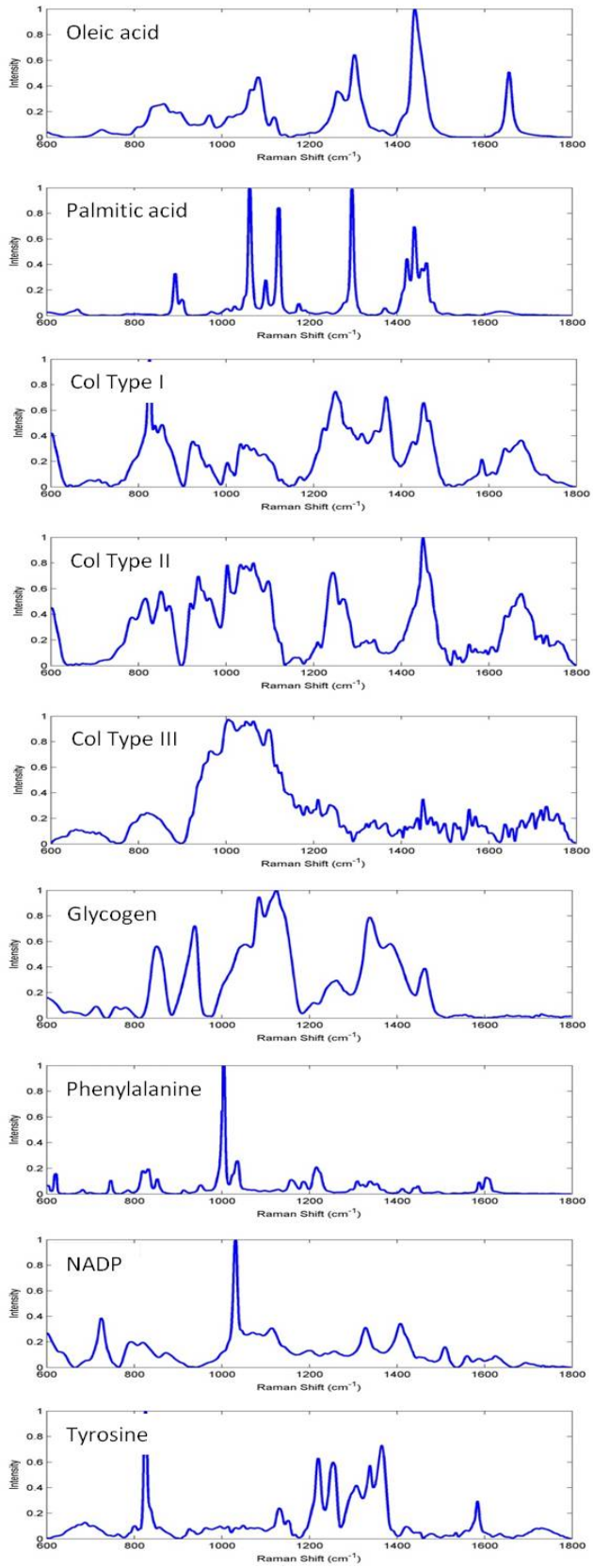

Figure 5-6. The Raman spectra of selected basic chemical components. These chemicals' spectra are used in fitting the liver tissue's Raman spectrum.

5.3.3 **Biological component analysis result**

Figure 5-7 shows the average Raman spectra of the liver tissue from different time points of NAFLD and the fitting results to the combination of selected basic biochemical components. The fitting result is represented in cyan color, the fitting residue is showed in red color. The fitting coefficient is shown in the Table 5-5, the fitting coefficients are normalized to sum to one. The coefficient of unsaturated fatty acid and saturated fatty acid are summed, the coefficient of collagen type I, II and III are also summed for easier discussion.

From the result, the change of fat components is the most obvious. From week 4 to week 6 the percentage of fat is increasing obviously. This can be explained by the changing of diet from common diet to high fat diet. The percentage of the collagen is also increasing, but the changing amplitude is not big and it remains unchanged in the later stage. This finding is consistent with our UV imaging of collagen and Sirus red staining of collagen, therefore the tissue is not much fiber condensed in the late stage in this animal model. The glycogen representing the polysaccharides inside the tissue is the second main form of energy storage besides fat, but since it has relatively lower energy

Table 5-5. The fitting coefficients of the basic components

components	meaning	W4 (%)*	W6 (%)	W8 (%)	W12 (%)	W17 (%)	W20 (%)
Fat	Fat droplets	50	67	65	66	60	60
Collagen	fibrosis	14	16	15.7	17	16	17
glycogen	Energy storage	5	0	2.1	0.8	0.8	1.8
Phenylalanine	cancer	14	7	6.5	6	8	7.2
NADH	metabolites	3	0	1.9	0.2	1.2	2

tyrosine	NO-derived oxidant	14	10	9.3	10	14	12

*The fitting coefficients are normalized to the sum to one, and represented in percentage form

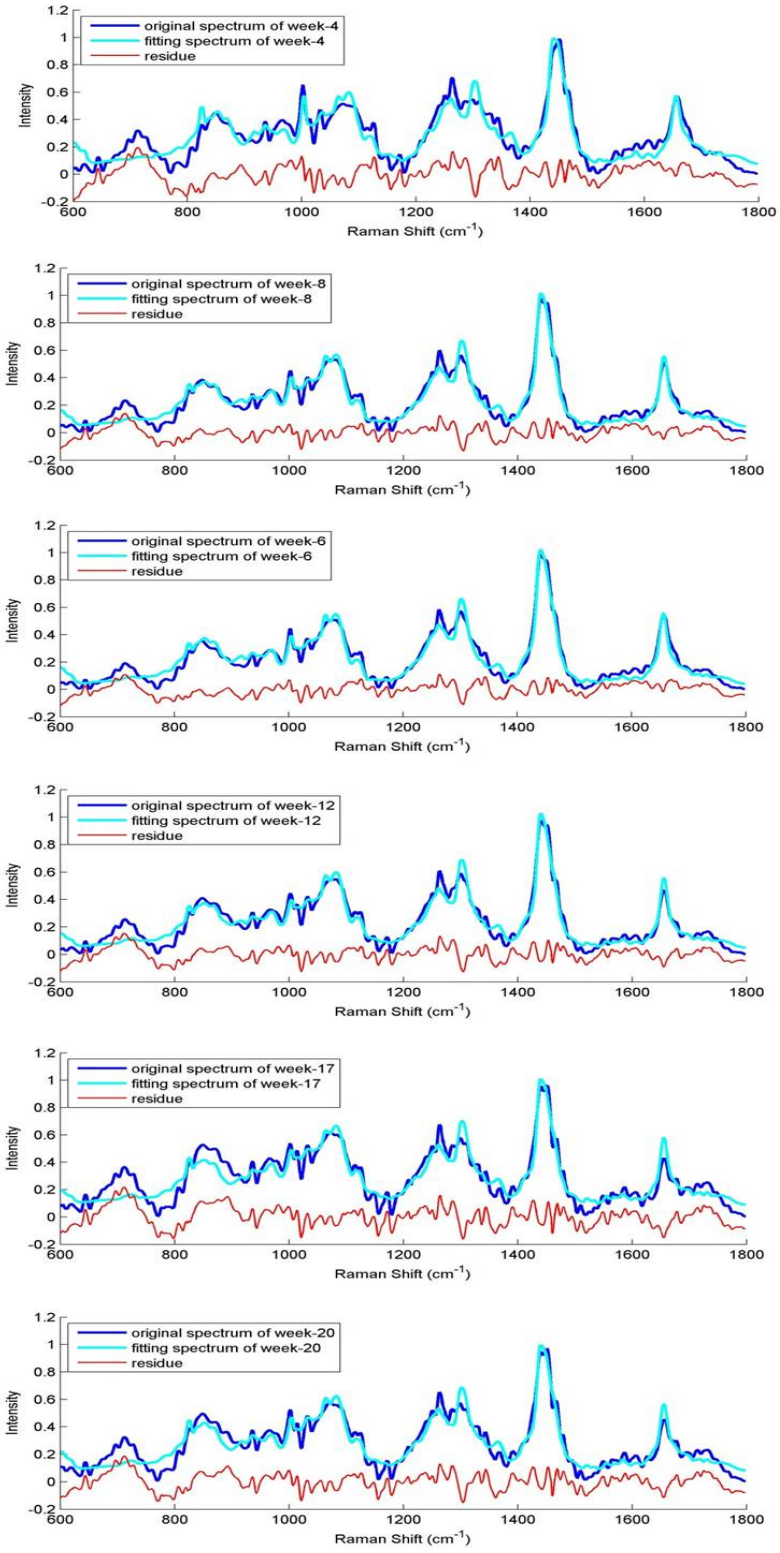

Figure 5-7. The mean Raman spectra of tissue at different time points and the corresponding fitting results. The line of blue color is the original spectrum, while the line of cyan color is the fitting result. The red color line is the fitting residue.

storage efficiency comparing to fat, so the amount of glycogen is lower than fat in liver. The amount of glycogen has decreased drastically from the week 4 indicate diseased liver tissue has lower metabolic ability. The NADH is not changing too much, we speculate the reason of this is that frozen preserving is not good for keeping NADH inside the tissue, so that NADH has largely vanished.

5.3.4 **Principle component analysis result**

The accumulated variance explained by the first 10 principle components (PC) is plotted in Figure 5-8. From the analysis, PC1 already accounts for the most variance (around 99.6%) in the data set. The first five PCs have achieved an accumulated variance up to100%.

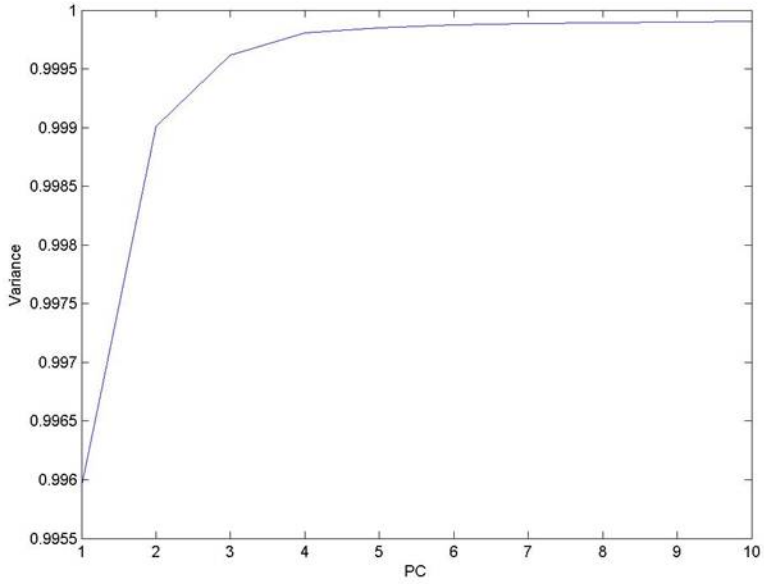

Figure 5-8. The accumulated variance explained by the first 10 PCs

The 2D and 3D plots of different combination of first five PCs are displayed in Figure 5-9. It was found that the combination of first PC has the most ability to differentiate the data set of different time points. However, the others don't show much ability in differentiating data. Referring back to the raw spectra of the tissue in Figure 5-3, the raw spectra of different time points shows

different magnitude. For PCA analysis, unless the vectors in the dataset are completely normalized, the top PC is typically a global shift of magnitude. This explains the great variance interpretation ability of PC1.

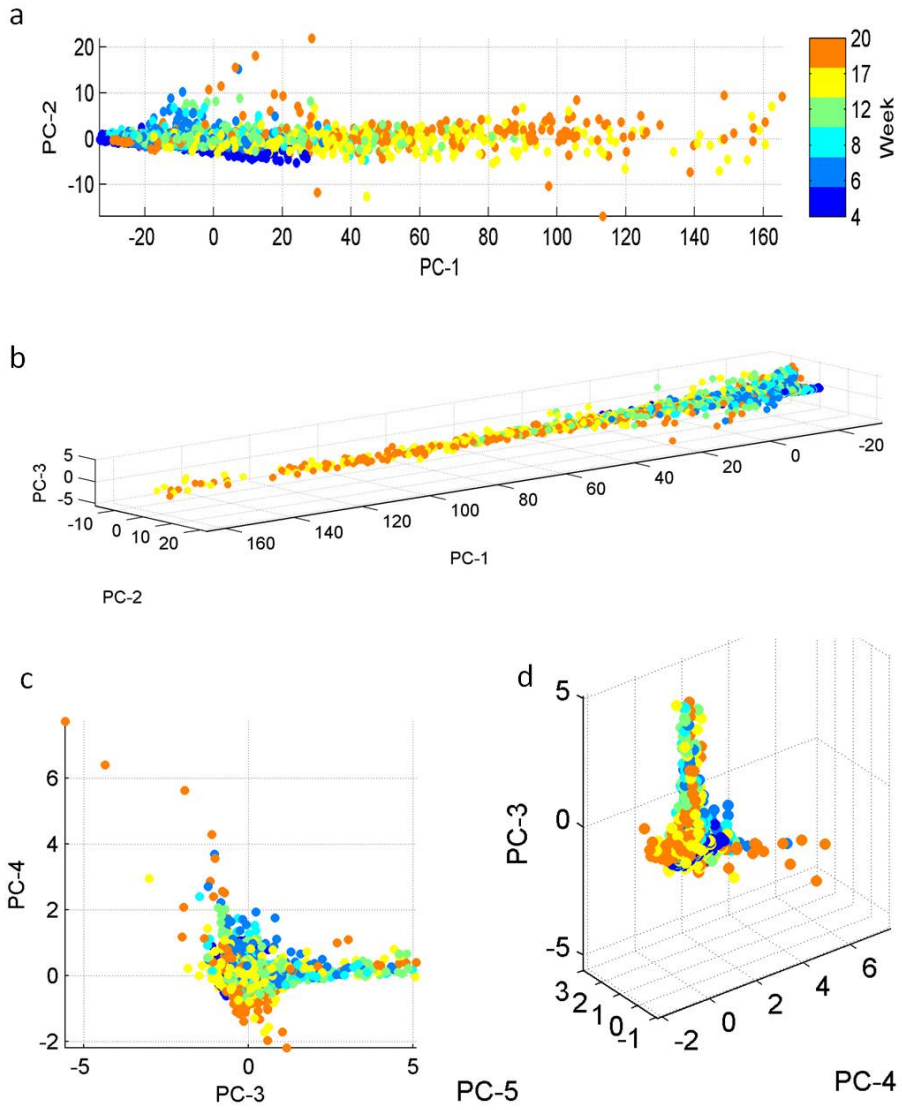

Figure 5-9. The 2D and 3D plot of different combinations of first five PCs

The loading of the first three principle components in PCA is shown in Figure 5-10. It was found that PC1 is much flat and it can be explained the global magnitude of the data, it can also be explained as the fluorescence background of the data set. PC2 is glass background signal caused by back-reflected Rayleigh light. PC3 resembles the spectrum of fatty acid (referring back to

Figure 5-6). This result indicates the dominant role of fatty acid in the progression of NAFLD.

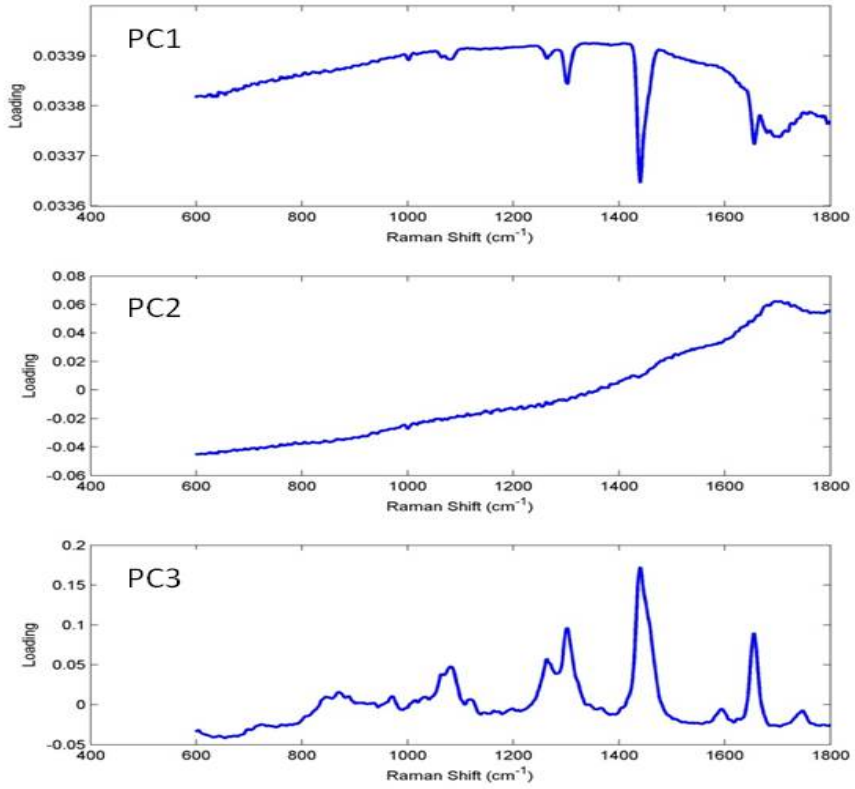

Figure 5-10. The loading of the first three PCs.

5.4 Conclusion

Raman spectroscopy provides a unique advantage in studying the fatty liver disease. Understanding the chemical basis of the Raman spectrum of the liver tissue with progressing NAFLD is necessarily important in developing the disease mechanism model for the future research. In this chapter, we described the experiment that used the near-infrared Raman spectroscopy to measure the spectra of liver tissue at six different time points. The Raman spectra with or without the fluorescence background is plotted. The data was analyzed by decomposing the tissue to the basic biochemical components using least square regression. The results show the clear increasing of fatty acid components. Principle components analysis was also used to identify the dominant differentiating factor within the dataset. The result also indicates the dominant role of fatty acid. We, hereby, acknowledge the important role of fatty acid accumulation during the progression of NAFLD. However, some data requires further analysis and careful scrutinizing to reveal the underlying mechanism of the disease.

Chapter 6 Conclusion and recommendations for future research

6.1 Summary

This thesis described the study of imaging marker from liver surface during the chronic liver disease progression using different optical microscopic techniques. The hypothesis that drives the whole thesis study is that the hepatic microcirculation is a meaningful marker for liver disease, and drives the progression of the disease. Chronic liver disease can be composed of complex histological spectra, such as inflammation, fibrosis and steatosis. In this thesis, the study focuses on two different histological spectra of chronic liver disease: fibrosis and steatosis.

The first part starts from the design and development of the intra-vital imaging window for liver in vivo imaging. With a highly reproducible liver fibrosis animal model, we established a quantified method to characterize the change of hepatic microcirculation during the fibrotic disease and correlated the changes with the staging of the fibrosis. We discovered that the drastic change of the hepatic microcirculation takes place in the early to middle stage of the fibrosis. From this result, we infer that the microcirculation lesion drives the progression of fibrosis by preceding the changes of the other features such as collagen accumulation.

In order to quantitatively denote the disease progression, we keep on looking for structural features of liver surface that relate to hepatic fibrotic status. On the same fibrosis model, images were taken from the liver of both normal rats and end stage fibrotic rats using nonlinear microscope. Five features regarding

the collagen, elastin morphology and redox status of hepatocytes were extracted and quantified. We found that they are significantly different between the normal and fibrotic group.

In the third part of the study, we shift our attention to the non-alcoholic fatty liver disease (NAFLD) because NAFLD has become the main driver for the increased prevalence of chronic liver disease worldwide. NAFLD is a chronic liver disease that involves multiple spectra of liver pathology, including hepatic steatosis, necroinflammation, fibrosis. Its complication includes advanced cirrhosis and HCC. In this part we focus on steatosis mainly and delineated the structural feature changes with Raman micro-spectroscopy, and find that fatty acid is playing a dominant role in the progression of the disease. The exact mechanism behind requires further experiment and analysis.

To conclude, this study focus on searching for imaging markers that are potentially useful to monitor the liver disease. With further study on this topic, we envision the integration of all the imaging markers and the comparison of the significant onset of structural feature change and the microcirculation feature change to further prove the hypothesis about the importance of microcirculation.

6.2 Recommendations for future research

In chapter 4, we have demonstrated that the hepatocytes redox status obtained from two photon images is changing with the liver disease status. In the literature searching, we also find that the redox status could also be related to the hepatic inflammation (186, 204). To demonstrate this hypothesis, further experiments need to be conducted.

As we have already known, BDL surgery created a well-established experimental extrahepatic cholestasis animal model. The early stage of extrahepatic cholestasis disease is featured by hepatic inflammation (205, 206). During the early phase after BDL, Kupffer cells are activated by showing increased phagocytic activity, cytokines formation and platelet activating factor formation one week after BDL (207-209). Therefore the early stage of BDL animal provides a good animal model of investigating hepatic inflammation. Using the redox ratio to monitor the early stage of the BDL model, we could probably have interesting findings.

In chapter 5, the biochemical components feature change of steatosis has been delineated with Raman micro-spectroscopy. With large amount of data acquired, the study requires further analysis to reveal the mechanism of the progression of NAFLD on this animal model. The statistical model of the disease progression can be created by feeding the features extracted from PCA and BCA analysis into a linear discriminant classifier to train the classifier. Further evaluating the classification accuracy and comparison between the two classifications would be an interesting discussion for this experiment.

References

1. R. Williams, "Global challenges in liver disease," *Hepatology* 44(3), 521-526 (2006)
2. W. H. Organization, *Global health risks: mortality and burden of disease attributable to selected major risks*, World Health Organization (2009).
3. G. Vernon, A. Baranova and Z. Younossi, "Systematic review: the epidemiology and natural history of non‐alcoholic fatty liver disease and non‐alcoholic steatohepatitis in adults," *Alimentary Pharmacology & Therapeutics* 34(3), 274-285 (2011)
4. L. Racine‐Samson, J. Scoazec, A. D'Errico, M. Fiorentino, L. Christa, A. Moreau, C. Roda, W. F. Grigioni and G. Feldmann, "The metabolic organization of the adult human liver: a comparative study of normal, fibrotic, and cirrhotic liver tissue," *Hepatology* 24(1), 104-113 (1996)
5. A. Desmoulière, I. Darby and G. Gabbiani, "Normal and pathologic soft tissue remodeling: role of the myofibroblast, with special emphasis on liver and kidney fibrosis," *Laboratory Investigation* 83(12), 1689-1707 (2003)
6. R. Bataller and D. A. Brenner, "Liver fibrosis," *Journal of Clinical Investigation* 115(2), 209-218 (2005)
7. A. Rappaport, "Hepatic blood flow: morphologic aspects and physiologic regulation," *International Review of Physiology* 21(1), 1-63 (1979)
8. I. R. Wanless, F. Wong, L. M. Blendis, P. Greig, E. Jenny Heathcote and G. Levy, "Hepatic and portal vein thrombosis in cirrhosis: possible role in development of parenchymal extinction and portal hypertension," *Hepatology* 21(5), 1238-1247 (1995)
9. I. R. Wanless, J. J. Liu and J. Butany, "Role of thrombosis in the pathogenesis of congestive hepatic fibrosis (cardiac cirrhosis)," *Hepatology* 21(5), 1232-1237 (1995)
10. L. Venkatraman, S.-M. Chia, B. C. Narmada, J. K. White and S. S. Bhowmick, "Plasmin Triggers a Switch-Like Decrease in Thrombospondin-Dependent Activation of TGF-β1," *Biophysical Journal* 103(5), 1060-1068 (2012)
11. V. Calvaruso, A. K. Burroughs, R. Standish, P. Manousou, F. Grillo, G. Leandro, S. Maimone, M. Pleguezuelo, I. Xirouchakis and G. Piero Guerrini, "Computer‐assisted image analysis of liver collagen: Relationship to Ishak scoring and hepatic venous pressure gradient," *Hepatology* 49(4), 1236-1244 (2009)
12. B. Vollmar, S. Siegmund and M. D. Menger, "An intravital fluorescence microscopic study of hepatic microvascular and cellular derangements in developing cirrhosis in rats," *Hepatology* 27(6), 1544-1553 (1998)
13. B. Vollmar, M. Rucker and M. D. Menger, "A new method for the intravital microscopic quantification of hepatic sinusoidal perfusion failure using the dye bisbenzamide H33342," *Microvascular Research* 51(2), 250-259 (1996)
14. S. Richter, J. Sperling, O. Kollmar, M. Menger and M. Schilling, "Laser Doppler flowmetry of hepatic microcirculation during Pringle's maneuver: determination of

spatial and temporal liver tissue perfusion heterogeneity," *European Surgical Research* 44(3-4), 152-158 (2009)
15. J. Kaneko, Y. Sugawara, Y. Matsui, H. Sakata and N. Kokudo, "Comparison of near-infrared spectroscopy and laser doppler flowmetry for detecting decreased hepatic inflow in the porcine liver," *Investigative Surgery* 22(4), 268-274 (2009)
16. T. Hashimoto, K. Miki, H. Imamura, K. Sano, S. Satou, Y. Sugawara, N. Kokudo and M. Makuuchi, "Sinusoidal perfusion in the veno‐occlusive region of living liver donors evaluated by indocyanine green and near‐infrared spectroscopy," *Liver Transplantation* 14(6), 872-880 (2008)
17. W. Groner, J. W. Winkelman, A. G. Harris, C. Ince, G. J. Bouma, K. Messmer and R. G. Nadeau, "Orthogonal polarization spectral imaging: a new method for study of the microcirculation," *Nature Medicine* 5(10), 1209-1212 (1999)
18. S. Xu, Y. Wang, D. C. Tai, S. Wang, C. L. Cheng, Q. Peng, J. Yan, Y. Chen, J. Sun and X. Liang, "qFibrosis: A fully-quantitative innovative method incorporating histological features to facilitate accurate fibrosis scoring in animal model and chronic hepatitis B patients," *Journal of Hepatology* 61(2), 260-269 (2014)
19. A. Maton, H. Jean and W. Charles, *Human biology and health*, Englewood Cliffs, New Jersey, USA (1993).
20. M.-A. Aller, N. Arias, I. Prieto, S. Agudo, C. Gilsanz, L. Lorente, J.-L. Arias and J. Arias, "A half century (1961-2011) of applying microsurgery to experimental liver research," *World Journal of Hepatology* 4(7), 199 (2012)
21. D. W. Lin, S. Johnson and C. A. Hunt, "Modeling liver physiology: combining fractals, imaging and animation," in *Engineering in Medicine and Biology Society. IEMBS'04. 26th Annual International Conference of the IEEE*, pp. 3120-3123, IEEE (2004).
22. C. C. Cunningham and C. G. Van Horn, "Energy availability and alcohol-related liver pathology," *Alcohol Research & Health* 27(4), 291-299 (2003)
23. S. L. Friedman, "Liver fibrosis—from bench to bedside," *Journal of Hepatolology* 38 (S1), S38-53 (2003)
24. P. Ginès, A. Cárdenas, V. Arroyo and J. Rodés, "Management of cirrhosis and ascites," *New England Journal of Medicine* 350(16), 1646-1654 (2004)
25. T. Poynard, P. Bedossa and P. Opolon, "Natural history of liver fibrosis progression in patients with chronic hepatitis C," *The Lancet* 349(9055), 825-832 (1997)
26. V. Mazzaferro, E. Regalia, R. Doci, S. Andreola, A. Pulvirenti, F. Bozzetti, F. Montalto, M. Ammatuna, A. Morabito and L. Gennari, "Liver transplantation for the treatment of small hepatocellular carcinomas in patients with cirrhosis," *New England Journal of Medicine* 334(11), 693-700 (1996)
27. G. Fattovich, T. Stroffolini, I. Zagni and F. Donato, "Hepatocellular carcinoma in cirrhosis: incidence and risk factors," *Gastroenterology* 127(5), S35-S50 (2004)

28. J. Llovet, X. Mas, J. Aponte, J. Fuster, M. Navasa, E. Christensen, J. Rodes and J. Bruix, "Cost effectiveness of adjuvant therapy for hepatocellular carcinoma during the waiting list for liver transplantation," *Gut* 50(1), 123-128 (2002)
29. E. Hahn, G. Wick, D. Pencev and R. Timpl, "Distribution of basement membrane proteins in normal and fibrotic human liver: collagen type IV, laminin, and fibronectin," *Gut* 21(1), 63-71 (1980)
30. S. L. Friedman, F. J. Roll, J. Boyles and D. M. Bissell, "Hepatic lipocytes: the principal collagen-producing cells of normal rat liver," *Proceedings of the National Academy of Sciences* 82(24), 8681-8685 (1985)
31. D. Li and S. Friedman, "Liver fibrogenesis and the role of hepatic stellate cells: new insights and prospects for therapy," *Journal of Gastroenterology and Hepatology* 14(7), 618-633 (1999)
32. T. Knittel, D. Kobold, B. Saile, A. Grundmann, K. Neubauer, F. Piscaglia and G. Ramadori, "Rat liver myofibroblasts and hepatic stellate cells: different cell populations of the fibroblast lineage with fibrogenic potential," *Gastroenterology* 117(5), 1205-1221 (1999)
33. J. J. Maher, *Interactions between hepatic stellate cells and the immune system*, Thieme Medical Publishers, Inc. (2001).
34. R. Benyon and J. Iredale, "Is liver fibrosis reversible?," *Gut* 46(4), 443-446 (2000)
35. S. L. Friedman, "Reversibility of hepatic fibrosis and cirrhosis—is it all hype?," *Nature Clinical Practice Gastroenterology & Hepatology* 4(5), 236-237 (2007)
36. S. L. Friedman and M. B. Bansal, "Reversal of hepatic fibrosis—fact or fantasy?," *Hepatology* 43(S1), S82-S88 (2006)
37. R. Issa, X. Zhou, C. M. Constandinou, J. Fallowfield, H. Millward-Sadler, M. D. Gaca, E. Sands, I. Suliman, N. Trim and A. Knorr, "Spontaneous recovery from micronodular cirrhosis: evidence for incomplete resolution associated with matrix cross-linking," *Gastroenterology* 126(7), 1795-1808 (2004)
38. P. Hammel, A. Couvelard, D. O'Toole, A. Ratouis, A. Sauvanet, J. F. Fléjou, C. Degott, J. Belghiti, P. Bernades and D. Valla, "Regression of liver fibrosis after biliary drainage in patients with chronic pancreatitis and stenosis of the common bile duct," *New England Journal of Medicine* 344(6), 418-423 (2001)
39. S. Pol, F. Carnot, B. Nalpas, J.-L. Lagneau, H. Fontaine, J. Serpaggi, L. Serfaty, P. Bedossa and C. Bréchot, "Reversibility of hepatitis C virus-related cirrhosis," *Human Pathology* 35(1), 107-112 (2004)
40. J. B. Dixon, P. S. Bhathal, N. R. Hughes and P. E. O'Brien, "Nonalcoholic fatty liver disease: improvement in liver histological analysis with weight loss," *Hepatology* 39(6), 1647-1654 (2004)
41. L. Falize, A. Guillygomarc'h, M. Perrin, F. Lainé, D. Guyader, P. Brissot, B. Turlin and Y. Deugnier, "Reversibility of hepatic fibrosis in treated genetic hemochromatosis: a study of 36 cases," *Hepatology* 44(2), 472-477 (2006)

42. M. Arthur, "Matrix degradation in liver: a role in injury and repair," *Hepatology* 26(4), 1069-1071 (1997)
43. J. P. Iredale, R. C. Benyon, M. Arthur, W. F. Ferris, R. Alcolado, P. J. Winwood, N. Clark and G. Murphy, "Tissue inhibitor of metalloproteinase‐1 messenger RNA expression is enhanced relative to interstitial collagenase messenger RNA in experimental liver injury and fibrosis," *Hepatology* 24(1), 176-184 (1996)
44. A. Elsharkawy, F. Oakley and D. Mann, "The role and regulation of hepatic stellate cell apoptosis in reversal of liver fibrosis," *Apoptosis* 10(5), 927-939 (2005)
45. D. N. Amarapurkar, E. Hashimoto, L. A. Lesmana, J. D. Sollano, P. J. Chen and K. L. Goh, "How common is non-alcoholic fatty liver disease in the Asia-Pacific region and are there local differences," *Journal of Gastroenterology and Hepatology* 22(6), 788-793 (2007)
46. J. M. Page and S. A. Harrison, "NASH and HCC," *Clinics in Liver Disease* 13(4), 631-647 (2009)
47. E. E. Calle, C. Rodriguez, K. Walker-Thurmond and M. J. Thun, "Overweight, obesity, and mortality from cancer in a prospectively studied cohort of US adults," *New England Journal of Medicine* 348(17), 1625-1638 (2003)
48. H. B. El-serag, T. Tran and J. E. Everhart, "Diabetes increases the risk of chronic liver disease and hepatocellular carcinoma," *Gastroenterology* 126(2), 460-468 (2004)
49. K. Yasui, E. Hashimoto, K. Tokushige, K. Koike, T. Shima, Y. Kanbara, T. Saibara, H. Uto, S. Takami and M. Kawanaka, "Clinical and pathological progression of non-alcoholic steatohepatitis to hepatocellular carcinoma," *Hepatology Research* 42(8), 767-773 (2012)
50. G. Guzman, E. M. Brunt, L. M. Petrovic, G. Chejfec, T. J. Layden and S. J. Cotler, "Does nonalcoholic fatty liver disease predispose patients to hepatocellular carcinoma in the absence of cirrhosis," *Archives of Pathology & Laboratory Medicine* 132(11), 1761-1766 (2008)
51. V. Paradis, S. Zalinski, E. Chelbi, N. Guedj, F. Degos, V. Vilgrain, P. Bedossa and J. Belghiti, "Hepatocellular carcinomas in patients with metabolic syndrome often develop without significant liver fibrosis: a pathological analysis," *Hepatology* 49(3), 851-859 (2009)
52. S. Nair, A. Mason, J. Eason, G. Loss and R. P. Perrillo, "Is obesity an independent risk factor for hepatocellular carcinoma in cirrhosis?," *Hepatology* 36(1), 150-155 (2002)
53. M. W. Yu, W. L. Shih, C. L. Lin, C. J. Liu, J. W. Jian, K. S. Tsai and C. J. Chen, "Body-mass index and progression of hepatitis B: a population-based cohort study in men," *Journal of Clinical Oncology* 26(34), 5576-5582 (2008)
54. G. N'Kontchou, J. Paries, M. T. T. Htar, N. Ganne–Carrie, L. Costentin, V. Grando–Lemaire, J. C. Trinchet and M. Beaugrand, "Risk factors for hepatocellular carcinoma in patients with alcoholic or viral C cirrhosis," *Clinical Gastroenterology and Hepatology* 4(8), 1062-1068 (2006)

55. H. F. Chen, P. Chen and C. Y. Li, "Risk of malignant neoplasms of liver and biliary tract in diabetic patients with different age and sex stratifications," *Hepatology* 52(1), 155-163 (2010)
56. W. Koh, R. Wang, A. Jin, M. Yu and J. Yuan, "Diabetes mellitus and risk of hepatocellular carcinoma: findings from the Singapore Chinese Health Study," *British Journal of Cancer* 108(5), 1182-1188 (2013)
57. C. L. Chen, H. I. Yang, W. S. Yang, C. J. Liu, P. J. Chen, S. L. You, L. Y. Wang, C. A. Sun, S. N. Lu and D. S. Chen, "Metabolic factors and risk of hepatocellular carcinoma by chronic hepatitis B/C infection: a follow-up study in Taiwan," *Gastroenterology* 135(1), 111-121 (2008)
58. M. M. Hassan, S. A. Curley, D. Li, A. Kaseb, M. Davila, E. K. Abdalla, M. Javle, D. M. Moghazy, R. D. Lozano and J. L. Abbruzzese, "Association of diabetes duration and diabetes treatment with the risk of hepatocellular carcinoma," *Cancer* 116(8), 1938-1946 (2010)
59. F. H. Epstein, P. J. Barnes and M. Karin, "Nuclear factor-κB—a pivotal transcription factor in chronic inflammatory diseases," *New England Journal of Medicine* 336(15), 1066-1071 (1997)
60. J. Napetschnig and H. Wu, "Molecular basis of NF-κB signaling," *Annual Review of Biophysics* 42(443 (2013)
61. R. G. Baker, M. S. Hayden and S. Ghosh, "NF-κB, inflammation, and metabolic disease," *Cell Metabolism* 13(1), 11-22 (2011)
62. L. Romics, K. Kodys, A. Dolganiuc, L. Graham, A. Velayudham, P. Mandrekar and G. Szabo, "Diverse regulation of NF-κB and peroxisome proliferator-activated receptors in murine nonalcoholic fatty liver," *Hepatology* 40(2), 376-385 (2004)
63. G. A. Michelotti, M. V. Machado and A. M. Diehl, "NAFLD, NASH and liver cancer," *Nature Reviews Gastroenterology and Hepatology* 10(11), 656-665 (2013)
64. P. Bedossa and T. Poynard, "An algorithm for the grading of activity in chronic hepatitis C," *Hepatology* 24(2), 289-293 (1996)
65. K. Ishak, A. Baptista, L. Bianchi, F. Callea, J. De Groote, F. Gudat, H. Denk, V. Desmet, G. Korb and R. N. MacSween, "Histological grading and staging of chronic hepatitis," *Journal of Hepatology* 22(6), 696-699 (1995)
66. P. Thampanitchawong and T. Piratvisuth, "Liver biopsy: complications and risk factors," *World Journal of Gastroenterology* 5(1), 301-304 (1999)
67. B. Maharaj, W. Leary, A. Naran, R. Maharaj, R. Cooppan, D. Pirie and D. Pudifin, "Sampling variability and its influence on the diagnostic yield of percutaneous needle biopsy of the liver," *The Lancet* 327(8480), 523-525 (1986)
68. R. J. Fontana and A. S. Lok, "Noninvasive monitoring of patients with chronic hepatitis C," *Hepatology* 36(5B), S57-S64 (2002)
69. D. S. Manning and N. H. Afdhal, "Diagnosis and quantitation of fibrosis," *Gastroenterology* 134(6), 1670-1681 (2008)
70. N. H. Afdhal, "Fibroscan (transient elastography) for the measurement of liver fibrosis," *Gastroenterology & Hepatology* 8(9), 605 (2012)

71. L. Castéra, J. Vergniol, J. Foucher, B. Le Bail, E. Chanteloup, M. Haaser, M. Darriet, P. Couzigou and V. de Lédinghen, "Prospective comparison of transient elastography, Fibrotest, APRI, and liver biopsy for the assessment of fibrosis in chronic hepatitis C," *Gastroenterology* 128(2), 343-350 (2005)
72. L. Huwart, C. Sempoux, E. Vicaut, N. Salameh, L. Annet, E. Danse, F. Peeters, L. C. ter Beek, J. Rahier and R. Sinkus, "Magnetic resonance elastography for the noninvasive staging of liver fibrosis," *Gastroenterology* 135(1), 32-40 (2008)
73. S. D. Taylor‐Robinson, J. Sargentoni, J. D. Bell, N. Saeed, K. K. Changani, B. R. Davidson, K. Rolles, A. K. Burroughs, H. J. Hodgson and C. S. Foster, "In vivo and in vitro hepatic 31P magnetic resonance spectroscopy and electron microscopy of the cirrhotic liver," *Liver* 17(4), 198-209 (1997)
74. V. Ntziachristos, "Going deeper than microscopy: the optical imaging frontier in biology," *Nature Methods* 7(8), 603-614 (2010)
75. Y. Hosoyamada, H. Kurihara and T. Sakai, "Ultrastructural localisation and size distribution of collagen fibrils in Glisson's sheath of rat liver: implications for mechanical environment and possible producing cells," *Journal of Anatomy* 196(03), 327-340 (2000)
76. R. J. Buschmann and J. W. Ryoo, "Hepatic structural correlates of liver fibrosis: a morphometric analysis," *Experimental and Molecular Pathology* 50(1), 114-124 (1989)
77. Y. He, C. H. Kang, S. Xu, X. Tuo, S. Trasti, D. C. Tai, A. M. Raja, Q. Peng, P. T. So and J. C. Rajapakse, "Toward surface quantification of liver fibrosis progression," *Journal of Biomed Optics* 15(5), 056007 (2010)
78. A. C. Croce, U. De Simone, M. Vairetti, A. Ferrigno, E. Boncompagni, I. Freitas and G. Bottiroli, "Liver autofluorescence properties in animal model under altered nutritional conditions," *Photochemical & Photobiological Sciences* 7(9), 1046-1053 (2008)
79. H. Senoo, N. Kojima and M. Sato, "Vitamin A‐Storing Cells (Stellate Cells)," *Vitamins & Hormones* 75(1), 131-159 (2007)
80. B. Vollmar, P. F. Conzen, T. Kerner, H. Habazettl, M. Vierl, H. Waldner and K. Peter, "Blood Flow and Tissue Oxygen Pressures of Liver and Pancreas in Rats Effects of Volatile Anesthetics and of Hemorrhage," *Anesthesia & Analgesia* 75(3), 421-430 (1992)
81. B. Vollmar and M. D. Menger, "The hepatic microcirculation: mechanistic contributions and therapeutic targets in liver injury and repair," *Physiological Reviews* 89(4), 1269-1339 (2009)
82. E. Wisse, "An electron microscopic study of the fenestrated endothelial lining of rat liver sinusoids," *Journal of Ultrastructure Research* 31(1), 125-150 (1970)
83. I. R. Wanless and K. Shiota, "The pathogenesis of nonalcoholic steatohepatitis and other fatty liver diseases: a four-step model including the role of lipid release and hepatic venular obstruction in the progression to cirrhosis," in *Seminars in liver disease*, pp. 99-106 (2004).

84. B. I. Choi, K. H. Lee, J. K. Han and J. M. Lee, "Hepatic arterioportal shunts: dynamic CT and MR features," *Korean Journal of Radiology* 3(1), 1-15 (2002)
85. J. Adler, M. Goodgold, H. Mitty, D. Gordon and M. Kinkhabwala, "Arteriovenous Shunts Involving the Liver 1," *Radiology* 129(2), 315-322 (1978)
86. A. K. Dunn, H. Bolay, M. A. Moskowitz and D. A. Boas, "Dynamic imaging of cerebral blood flow using laser speckle," *Journal of Cerebral Blood Flow & Metabolism* 21(3), 195-201 (2001)
87. Z. Wang, W. Luo, P. Li, J. Qiu and Q. Luo, "Acute hyperglycemia compromises cerebral blood flow following cortical spreading depression in rats monitored by laser speckle imaging," *Journal of Biomedical Optics* 13(6), 064023 (2008)
88. N. Feng, J. Qiu, P. Li, X. Sun, C. Yin, W. Luo, S. Chen and Q. Luo, "Simultaneous automatic arteries-veins separation and cerebral blood flow imaging with single-wavelength laser speckle imaging," *Optical Express* 19(17), 15777-15791 (2011)
89. A. Fercher and J. Briers, "Flow visualization by means of single-exposure speckle photography," *Optics Communications* 37(5), 326-330 (1981)
90. R. Bandyopadhyay, A. Gittings, S. Suh, P. Dixon and D. Durian, "Speckle-visibility spectroscopy: A tool to study time-varying dynamics," *Review of Scientific Instruments* 76(9), 093110 (2005)
91. B. J. Berne and R. Pecora, *Dynamic light scattering: with applications to chemistry, biology, and physics*, Courier Dover Publications (2000).
92. P. A. Lemieux and D. Durian, "Investigating non-Gaussian scattering processes by using nth-order intensity correlation functions," *JOSA A* 16(7), 1651-1664 (1999)
93. T. Sugiyama, Y. Mashima, Y. Yoshioka, H. Oku and T. Ikeda, "Effect of unoprostone on topographic and blood flow changes in the ischemic optic nerve head of rabbits," *Archives of Ophthalmology* 127(4), 454-459 (2009)
94. N. Koseki, M. Araie, A. Tomidokoro, M. Nagahara, T. Hasegawa, Y. Tamaki and S. Yamamoto, "A placebo-controlled 3-year study of a calcium blocker on visual field and ocular circulation in glaucoma with low-normal pressure," *Ophthalmology* 115(11), 2049-2057 (2008)
95. K. Yaoeda, M. Shirakashi, S. Funaki, H. Funaki, T. Nakatsue and H. Abe, "Measurement of microcirculation in the optic nerve head by laser speckle flowgraphy and scanning laser Doppler flowmetry," *American Journal of Ophthalmology* 129(6), 734-739 (2000)
96. A. K. Dunn, A. Devor, A. M. Dale and D. A. Boas, "Spatial extent of oxygen metabolism and hemodynamic changes during functional activation of the rat somatosensory cortex," *Neuroimage* 27(2), 279-290 (2005)
97. M. Li, P. Miao, J. Yu, Y. Qiu, Y. Zhu and S. Tong, "Influences of hypothermia on the cortical blood supply by laser speckle imaging," *Neural Systems and Rehabilitation Engineering* 17(2), 128-134 (2009)

98. Y. C. Huang, T. L. Ringold, J. S. Nelson and B. Choi, "Noninvasive blood flow imaging for real‐time feedback during laser therapy of port wine stain birthmarks," *Lasers in Surgery and Medicine* 40(3), 167-173 (2008)
99. J. B. Birks, *Photophysics of Aromatic Molecules*, Wiley-Interscience, New York (1975).
100. W. Denk, J. H. Strickler and W. W. Webb, "Two-photon laser scanning fluorescence microscopy," *Science* 248(4951), 73-76 (1990)
101. P. Franken, A. Hill, C. Peters and G. Weinreich, "Generation of optical harmonics," *Physical Review Letters* 7(4), 118-119 (1961)
102. E. Yew and C. Sheppard, "Effects of axial field components on second harmonic generation microscopy," *Optical Express* 14(3), 1167-1174 (2006)
103. F. Helmchen and W. Denk, "Deep tissue two-photon microscopy," *Nature Methods* 2(12), 932-940 (2005)
104. R. K. Jain, L. L. Munn and D. Fukumura, "Dissecting tumour pathophysiology using intravital microscopy," *Nature Reviews Cancer* 2(4), 266-276 (2002)
105. R. Christie, B. Bacskai, W. Zipfel, R. Williams, S. Kajdasz, W. Webb and B. Hyman, "Growth arrest of individual senile plaques in a model of Alzheimer's disease observed by in vivo multiphoton microscopy," *The Journal of Neuroscience* 21(3), 858-864 (2001)
106. E. J. Yoder and D. Kleinfeld, "Cortical imaging through the intact mouse skull using two-photon excitation laser scanning microscopy," *Microscopy Research and Technique* 56(4), 304-305 (2002)
107. J. M. Squirrell, D. L. Wokosin, J. G. White and B. D. Bavister, "Long-term two-photon fluorescence imaging of mammalian embryos without compromising viability," *Nature Biotechnology* 17(8), 763-767 (1999)
108. S. Isogai, N. D. Lawson, S. Torrealday, M. Horiguchi and B. M. Weinstein, "Angiogenic network formation in the developing vertebrate trunk," *Development* 130(21), 5281-5290 (2003)
109. J. G. White, J. M. Squirrell and K. W. Eliceiri, "Applying multiphoton imaging to the study of membrane dynamics in living cells," *Traffic* 2(11), 775-780 (2001)
110. Y. Imanishi, M. L. Batten, D. W. Piston, W. Baehr and K. Palczewski, "Noninvasive two-photon imaging reveals retinyl ester storage structures in the eye," *The Journal of Cell Biology* 164(3), 373-383 (2004)
111. K. Ohki, S. Chung, Y. H. Ch'ng, P. Kara and R. C. Reid, "Functional imaging with cellular resolution reveals precise micro-architecture in visual cortex," *Nature* 433(7026), 597-603 (2005)
112. C. A. Thorling, X. Liu, F. J. Burczynski, L. M. Fletcher, G. C. Gobe and M. S. Roberts, "Multiphoton microscopy can visualize zonal damage and decreased cellular metabolic activity in hepatic ischemia-reperfusion injury in rats," *Journal of Biomedical Optics* 16(11), 116011 (2011)
113. C. A. Thorling, Y. Dancik, C. W. Hupple, G. Medley, X. Liu, A. V. Zvyagin, T. A. Robertson, F. J. Burczynski and M. S. Roberts, "Multiphoton microscopy and

fluorescence lifetime imaging provide a novel method in studying drug distribution and metabolism in the rat liver in vivo," *Journal of Biomedical Optics* 16(8), 086013 (2011)
114. T. Hirschfeld and B. Chase, "FT-Raman spectroscopy: development and justification," *Applied Spectroscopy* 40(2), 133-137 (1986)
115. C.-H. Liu, B. Das, W. Glassman, G. Tang, K. Yoo, H. Zhu, D. Akins, S. Lubicz, J. Cleary and R. Prudente, "Raman, fluorescence, and time-resolved light scattering as optical diagnostic techniques to separate diseased and normal biomedical media," *Journal of Photochemistry and Photobiology B: Biology* 16(2), 187-209 (1992)
116. K. E. Shafer‐Peltier, A. S. Haka, M. Fitzmaurice, J. Crowe, J. Myles, R. R. Dasari and M. S. Feld, "Raman microspectroscopic model of human breast tissue: implications for breast cancer diagnosis in vivo," *Journal of Raman Spectroscopy* 33(7), 552-563 (2002)
117. M. S. Feld, R. Manoharan, J. Salenius, J. Orenstein-Carndona, T. J. Roemer, J. F. Brennan III, R. R. Dasari and Y. Wang, "Detection and characterization of human tissue lesions with near-infrared Raman spectroscopy," in *Photonics West'95*, pp. 99-104, International Society for Optics and Photonics (1995).
118. T. J. Römer, J. F. Brennan, M. Fitzmaurice, M. L. Feldstein, G. Deinum, J. L. Myles, J. R. Kramer, R. S. Lees and M. S. Feld, "Histopathology of human coronary atherosclerosis by quantifying its chemical composition with Raman spectroscopy," *Circulation* 97(9), 878-885 (1998)
119. A. Mizuno, H. Kitajima, K. Kawauchi, S. Muraishi and Y. Ozaki, "Near‐infrared Fourier transform Raman spectroscopic study of human brain tissues and tumours," *Journal of Raman Spectroscopy* 25(1), 25-29 (1994)
120. R. Manoharan, Y. Wang, N. N. Boustany, J. F. Brennan III, J. J. Baraga, R. R. Dasari, J. Van Dam, S. Singer and M. S. Feld, "Raman spectroscopy for cancer detection: instrument development and tissue diagnosis," in *International Symposium on Biomedical Optics Europe'94*, pp. 128-132, International Society for Optics and Photonics (1994).
121. I. R. Wanless and K. Shiota, "The pathogenesis of nonalcoholic steatohepatitis and other fatty liver diseases: a four-step model including the role of lipid release and hepatic venular obstruction in the progression to cirrhosis," in *Seminars in liver disease*, pp. 99-106, Thieme Medical Publishers, Inc. (2004).
122. R. Bauer, B. Walter, E. Würker, H. Kluge and U. Zwiener, "Colored microsphere technique as a new method for quantitative-multiple estimation of regional hepatic and portal blood flow," *Experimental and Toxicologic Pathology* 48(5), 415-420 (1996)
123. R. Mackenzie, D. Leiberman, R. Mathie, G. Rice, A. Harper and L. Blumgart, "Liver blood flow measurement the interpretation of xenon133 clearance curves," *Acta chirurgica Scandinavica* 142(7), 519 (1976)
124. A. El‐Desoky, A. Seifalian, M. Cope, D. Delpy and B. Davidson, "Experimental study of liver dysfunction evaluated by direct indocyanine green

clearance using near infrared spectroscopy," *British Journal of Surgery* 86(8), 1005-1011 (1999)
125. H. Komatsu, A. Koo and P. H. Guth, "Leukocyte flow dynamics in the rat liver microcirculation," *Microvascular Research* 40(1), 1-13 (1990)
126. B. Vollmar, M. Burkhardt, T. Minor, H. Klauke and M. D. Menger, "High-Resolution Microscopic Determination of Hepatic NADH Fluorescence for in Vivo Monitoring of Tissue Oxygenation during Hemorrhagic Shock and Resuscitation," *Microvascular Research* 54(2), 164-173 (1997)
127. N. Almond and A. Wheatley, "Measurement of hepatic perfusion in rats by laser Doppler flowmetry," *American Journal of Physiology-Gastrointestinal and Liver Physiology* 262(2), G203-G209 (1992)
128. D. Arvidsson, H. Svensson and U. Haglund, "Laser-Doppler flowmetry for estimating liver blood flow," *American Journal of Physiology-Gastrointestinal and Liver Physiology* 254(4), G471-G476 (1988)
129. K. W. Walton, "Investigation of the toxicity of a series of dextran sulphates of varying molecular weight," *British Journal of Pharmacology and Chemotherapy* 9(1), 1-14 (1954)
130. G. A. Lutty, "The acute intravenous toxicity of biological stains, dyes, and other fluorescent substances," *Toxicology and Applied Pharmacolology* 44(2), 225-249 (1978)
131. S. M. Daly and M. J. Leahy, "'Go with the flow': A review of methods and advancements in blood flow imaging," *Journal of Biophotonics* 6(3), 217-255 (2013)
132. A. C. Croce, A. Ferrigno, M. Vairetti, R. Bertone, I. Freitas and G. Bottiroli, "Autofluorescence properties of isolated rat hepatocytes under different metabolic conditions," *Photochemical & Photobiological Sciences* 3(10), 920-926 (2004)
133. D. A. Boas and A. K. Dunn, "Laser speckle contrast imaging in biomedical optics," *Journal of Biomedical Optics* 15(1), 011109 (2010)
134. J. D. Briers, G. Richards and X. W. He, "Capillary blood flow monitoring using laser speckle contrast analysis (LASCA)," *Journal of Biomedical Optics* 4(1), 164-175 (1999)
135. M. Li, P. Miao, Y. Zhu and S. Tong, "Functional laser speckle imaging of cerebral blood flow under hypothermia," *Journal of Biomedical Optics* 16(8), 086011 (2011)
136. V. Kalchenko, A. Brill, M. Bayewitch, I. Fine, V. Zharov, E. Galanzha, V. Tuchin and A. Harmelin, "In vivo dynamic light scattering imaging of blood coagulation," *Journal of Biomedical Optics* 12(5), 052002 (2007)
137. A. Kharlamov, B. R. Brown, K. A. Easley and S. C. Jones, "Heterogeneous response of cerebral blood flow to hypotension demonstrated by laser speckle imaging flowmetry in rats," *Neuroscience Letters* 368(2), 151-156 (2004)
138. B. Choi, N. M. Kang and J. S. Nelson, "Laser speckle imaging for monitoring blood flow dynamics in the in vivo rodent dorsal skin fold model," *Microvascular Research* 68(2), 143-146 (2004)

139. J. Briers and A. Fercher, "Retinal blood-flow visualization by means of laser speckle photography," *Investigative Ophthalmology & Visual Science* 22(2), 255-259 (1982)
140. A. I. Srienc, Z. L. Kurth-Nelson and E. A. Newman, "Imaging retinal blood flow with laser speckle flowmetry," in *Frontiers in Neuroenergetics* (2010).
141. N. Hecht, J. Woitzik, J. P. Dreier and P. Vajkoczy, "Intraoperative monitoring of cerebral blood flow by laser speckle contrast analysis," *Neurosurgical Focus* 27(4), E11 (2009)
142. A. B. Parthasarathy, E. L. Weber, L. M. Richards, D. J. Fox and A. K. Dunn, "Laser speckle contrast imaging of cerebral blood flow in humans during neurosurgery: a pilot clinical study," *Journal of Biomedical Optics* 15(6), 066030 (2010)
143. E. Klijn, H. C. Hulscher, R. K. Balvers, W. P. Holland, J. Bakker, A. J. Vincent, C. M. Dirven and C. Ince, "Laser speckle imaging identification of increases in cortical microcirculatory blood flow induced by motor activity during awake craniotomy: clinical article," *Journal of Neurosurgery* 118(2), 280-286 (2013)
144. P. Georgiev, W. Jochum, S. Heinrich, J. Jang, A. Nocito, F. Dahm and P. A. Clavien, "Characterization of time‐related changes after experimental bile duct ligation," *British Journal of Surgery* 95(5), 646-656 (2008)
145. O. Tarcin, M. Basaranoglu, V. Tahan, G. Tahan, I. Sücüllü, N. Yilmaz, G. Sood, N. Snyder, G. Hilman and C. Celikel, "Time course of collagen peak in bile duct-ligated rats," *BMC Gastroenterology* 11(1), 45 (2011)
146. J. Kountouras, B. H. Billing and P. J. Scheuer, "Prolonged bile duct obstruction: a new experimental model for cirrhosis in the rat," *British Journal of Experimental Pathology* 65(3), 305 (1984)
147. Y. Liu, H.-C. Chen, T.-L. Sun, L.-L. Chiou, C.-Y. Dong, H.-S. Lee, G. T. Huang, W. Lo and S.-M. Yang, "Visualization of hepatobiliary excretory function by intravital multiphoton microscopy," *Journal of Biomedical Optics* 12(1), 014014 (2007)
148. L. Van Pelt, "Ketamine and xylazine for surgical anesthesia in rats," *Journal of the American Veterinary Medical Association* 171(9), 842-844 (1977)
149. M.-A. Aller, J.-L. Arias, I. Prieto and J. Arias, "A suitable microsurgical method for obstructive cholestasis in the rat," *Protocol Exchange* (2010)
150. M. A. Aller, J. L. Arias, J. Garcia-Dominguez, J. I. Arias, M. Duran and J. Arias, "Experimental obstructive cholestasis: the wound-like inflammatory liver response," *Fibrogenesis & Tissue Repair* 1(1), 6 (2008)
151. D.-J. Kroon, "Hessian based Frangi Vesselness filter (http://www.mathworks.com/matlabcentral/fileexchange/24409-hessian-based-frangi-vesselness-filter)," in *MATLAB Central File Exchange, Retrieved 02-Mar-2010* (2009).
152. A. F. Frangi, W. J. Niessen, K. L. Vincken and M. A. Viergever, "Multiscale vessel enhancement filtering," in *Medical Image Computing and Computer-Assisted Interventation—MICCAI'98*, pp. 130-137, Springer (1998).

153. L. L. Ong, J. Dauwels, M. H. Ang, Jr. and H. H. Asada, "A Bayesian filtering approach to incorporate 2D/3D time-lapse confocal images for tracking angiogenic sprouting cells interacting with the gel matrix," *Medical Image Analalysis* 18(1), 211-227 (2014)
154. M. J. Ruwart, K. F. Wilkinson, B. D. Rush, T. J. Vidmar, K. M. Peters, K. S. Henley, H. D. Appelman, K. Y. Kim, D. Schuppan and E. G. Hahn, "The integrated value of serum procollagen III peptide over time predicts hepatic hydroxyproline content and stainable collagen in a model of dietary cirrhosis in the rat," *Hepatology* 10(5), 801-806 (1989)
155. G. Boigk, L. Stroedter, H. Herbst, J. Waldschmidt, E. O. Riecken and D. Schuppan, "Silymarin retards collagen accumulation in early and advanced biliary fibrosis secondary to complete bile duct obliteration in rats," *Hepatology* 26(3), 643-649 (1997)
156. R. G. Knodell, K. G. Ishak, W. C. Black, T. S. Chen, R. Craig, N. Kaplowitz, T. W. Kiernan and J. Wollman, "Formulation and application of a numerical scoring system for assessing histological activity in asymptomatic chronic active hepatitis," *Hepatology* 1(5), 431-435 (1981)
157. O. Thompson, M. Andrews and E. Hirst, "Correction for spatial averaging in laser speckle contrast analysis," *Biomedical Optical Express* 2(4), 1021-1029 (2011)
158. J. D. Briers and X.-W. He, "Laser speckle contrast analysis (LASCA) for blood flow visualization: improved image processing," in *BiOS'98 International Biomedical Optics Symposium*, pp. 26-33, International Society for Optics and Photonics (1998).
159. I. A. Sherman, S. C. Pappas and M. M. Fisher, "Hepatic microvascular changes associated with development of liver fibrosis and cirrhosis," *The American Journal of Physiology* 258(2 Pt 2), H460-465 (1990)
160. K. Allen, H. Jaeschke and B. L. Copple, "Bile acids induce inflammatory genes in hepatocytes: a novel mechanism of inflammation during obstructive cholestasis," *The American Journal of Pathology* 178(1), 175-186 (2011)
161. E. Vanheule, A. M. Geerts, J. Van Huysse, D. Schelfhout, M. Praet, H. Van Vlierberghe, M. De Vos and I. Colle, "An intravital microscopic study of the hepatic microcirculation in cirrhotic mice models: relationship between fibrosis and angiogenesis," *International Journal of Experimental Pathology* 89(6), 419-432 (2008)
162. D. Kedrin, B. Gligorijevic, J. Wyckoff, V. V. Verkhusha, J. Condeelis, J. E. Segall and J. van Rheenen, "Intravital imaging of metastatic behavior through a mammary imaging window," *Nature Methods* 5(12), 1019 (2008)
163. M. J. Levene, D. A. Dombeck, K. A. Kasischke, R. P. Molloy and W. W. Webb, "In Vivo Multiphoton Microscopy of Deep Brain Tissue," *Journal of Neurophysiology* 91(4), 1908-1912 (2004).
164. J. Y. Perentes, T. D. McKee, C. D. Ley, H. Mathiew, M. Dawson, T. P. Padera, L. L. Munn, R. K. Jain and Y. Boucher, "In vivo imaging of extracellular matrix remodeling by tumor-associated fibroblasts," *Nature Methods* 6(2), 143 (2009)

165. D. Fukumura and R. K. Jain, "Imaging angiogenesis and the microenvironment," *Apmis* 116(7–8), 695-715 (2008)
166. L. S. Friedman and E. B. Keeffe, *Handbook of liver disease*, Elsevier Health Sciences (2011).
167. R. Weissleder and M. J. Pittet, "Imaging in the era of molecular oncology," *Nature* 452(7187), 580-589 (2008)
168. M. Goetz and R. Kiesslich, "Advances of endomicroscopy for gastrointestinal physiology and diseases," *American Journal of Physiology-Gastrointestinal and Liver Physiology* 298(6), G797-G806 (2010)
169. D. Kobat, M. E. Durst, N. Nishimura, A. W. Wong, C. B. Schaffer and C. Xu, "Deep tissue multiphoton microscopy using longer wavelength excitation," *Optics Express* 17(16), 13354-13364 (2009)
170. W. R. Zipfel, R. M. Williams, R. Christie, A. Y. Nikitin, B. T. Hyman and W. W. Webb, "Live tissue intrinsic emission microscopy using multiphoton-excited native fluorescence and second harmonic generation," *Proceedings of the National Academy of Sciences* 100(12), 7075-7080 (2003)
171. J. N. Rogart, J. Nagata, C. S. Loeser, R. D. Roorda, H. Aslanian, M. E. Robert, W. R. Zipfel and M. H. Nathanson, "Multiphoton imaging can be used for microscopic examination of intact human gastrointestinal mucosa ex vivo," *Clinical Gastroenterology and Hepatology* 6(1), 95-101 (2008)
172. S. Zhuo, J. Chen, T. Luo, D. Zou and J. Zhao, "Multimode nonlinear optical imaging of the dermis in ex vivo human skin based on the combination of multichannel mode and Lambda mode," *Optics Express* 14(17), 7810-7820 (2006)
173. S. Zhuo, J. Yan, G. Chen, J. Chen, Y. Liu, J. Lu, X. Zhu, X. Jiang and S. Xie, "Label-free monitoring of colonic cancer progression using multiphoton microscopy," *Biomedical Optics Express* 2(3), 615-619 (2011)
174. V. A. Hovhannisyan, P.-J. Su, S.-J. Lin and C.-Y. Dong, "Quantifying thermodynamics of collagen thermal denaturation by second harmonic generation imaging," *Applied Physics Letters* 94(23), 233902 (2009)
175. P. J. Campagnola and L. M. Loew, "Second-harmonic imaging microscopy for visualizing biomolecular arrays in cells, tissues and organisms," *Nature Biotechnology* 21(11), 1356-1360 (2003)
176. E. Brown and T. McKee, "Dynamic imaging of collagen and its modulation in tumors in vivo using second-harmonic generation," *Nature Medicine* 9(6), 796-800 (2003)
177. R. N. McCoy, K. E. Hill, M. A. Ayon, J. H. Stein and R. F. Burk, "Oxidant stress following renal ischemia: changes in the glutathione redox ratio," *Kidney Int* 33(4), 812-817 (1988)
178. N. D. Kirkpatrick, J. A. Weiss, U. Utzinger, J. B. Hoying and S. K. Botting, "In vitro model for endogenous optical signatures of collagen," *Journal of Biomedical Optics* 11(5), 054021 (2006)

179. P. Theer, M. T. Hasan and W. Denk, "Two-photon imaging to a depth of 1000 microm in living brains by use of a Ti:Al2O3 regenerative amplifier," *Optics Letters* 28(12), 1022-1024 (2003)
180. G. Cox, E. Kable, A. Jones, I. Fraser, F. Manconi and M. D. Gorrell, "3-dimensional imaging of collagen using second harmonic generation," *Journal of Structural Biology* 141(1), 53-62 (2003)
181. A. C. Croce, A. Ferrigno, G. Santin, V. M. Piccolini, G. Bottiroli and M. Vairetti, "Autofluorescence of liver tissue and bile: Organ functionality monitoring during ischemia and reoxygenation," *Lasers in Surgery and Medicine* (2014)
182. J. Foucher, E. Chanteloup, J. Vergniol, L. Castera, B. Le Bail, X. Adhoute, J. Bertet, P. Couzigou and V. de Ledinghen, "Diagnosis of cirrhosis by transient elastography (FibroScan): a prospective study," *Gut* 55(3), 403-408 (2006)
183. S.-J. Lin, S.-H. Jee, C.-J. Kuo, R. Wu Jr, W.-C. Lin, J.-S. Chen, Y.-H. Liao, C.-J. Hsu, T.-F. Tsai and Y.-F. Chen, "Discrimination of basal cell carcinoma from normal dermal stroma by quantitative multiphoton imaging," *Optics Letters* 31(18), 2756-2758 (2006)
184. C. Guyot, C. Combe and A. Desmoulière, "The common bile duct ligation in rat: a relevant in vivo model to study the role of mechanical stress on cell and matrix behaviour," *Histochemistry and Cell Biology* 126(4), 517-523 (2006)
185. M. C. Skala, K. M. Riching, A. Gendron-Fitzpatrick, J. Eickhoff, K. W. Eliceiri, J. G. White and N. Ramanujam, "In vivo multiphoton microscopy of NADH and FAD redox states, fluorescence lifetimes, and cellular morphology in precancerous epithelia," *Proceedings of the National Academy of Sciences* 104(49), 19494-19499 (2007)
186. J. S. Gujral, A. Farhood, M. L. Bajt and H. Jaeschke, "Neutrophils aggravate acute liver injury during obstructive cholestasis in bile duct–ligated mice," *Hepatology* 38(2), 355-363 (2003)
187. H. Miyoshi, C. Rust, P. J. Roberts, L. J. Burgart and G. J. Gores, "Hepatocyte apoptosis after bile duct ligation in the mouse involves Fas," *Gastroenterology* 117(3), 669-677 (1999)
188. Y. Zhang, M. L. Akins, K. Murari, J. Xi, M.-J. Li, K. Luby-Phelps, M. Mahendroo and X. Li, "A compact fiber-optic SHG scanning endomicroscope and its application to visualize cervical remodeling during pregnancy," *Proceedings of the National Academy of Sciences* 109(32), 12878-12883 (2012)
189. M. Gu, H. C. Bao and J. L. Li, "Cancer-cell microsurgery using nonlinear optical endomicroscopy," *Journal of Biomedical Optics* 15(5), 050502 (2010)
190. D. R. Rivera, C. M. Brown, D. G. Ouzounov, I. Pavlova, D. Kobat, W. W. Webb and C. Xu, "Compact and flexible raster scanning multiphoton endoscope capable of imaging unstained tissue," *Proceedings of the National Academy of Sciences* 108(43), 17598-17603 (2011)

191. K. König, A. Ehlers, I. Riemann, S. Schenkl, R. Bückle and M. Kaatz, "Clinical two‐photon microendoscopy," *Microscopy Research and Technique* 70(5), 398-402 (2007)
192. A. Nijssen, T. C. B. Schut, F. Heule, P. J. Caspers, D. P. Hayes, M. H. Neumann and G. J. Puppels, "Discriminating basal cell carcinoma from its surrounding tissue by Raman spectroscopy," *Journal of Investigative Dermatology* 119(1), 64-69 (2002)
193. Z. Huang, A. McWilliams, H. Lui, D. I. McLean, S. Lam and H. Zeng, "Near‐infrared Raman spectroscopy for optical diagnosis of lung cancer," *International Journal of Cancer* 107(6), 1047-1052 (2003)
194. A. Cao, A. K. Pandya, G. K. Serhatkulu, R. E. Weber, H. Dai, J. S. Thakur, V. M. Naik, R. Naik, G. W. Auner and R. Rabah, "A robust method for automated background subtraction of tissue fluorescence," *Journal of Raman Spectroscopy* 38(9), 1199-1205 (2007)
195. C. A. Lieber and A. Mahadevan-Jansen, "Automated method for subtraction of fluorescence from biological Raman spectra," *Applied Spectroscopy* 57(11), 1363-1367 (2003)
196. N. Kunapareddy, J. P. Freyer and J. R. Mourant, "Raman spectroscopic characterization of necrotic cell death," *Journal of Biomedical Optics* 13(5), 054002 (2008)
197. I. Boere, T. Bakker Schut, J. van Den Boogert, R. De Bruin and G. Puppels, "Use of fibre optic probes for detection of Barrett's epithelium in the rat oesophagus by Raman spectroscopy," *Vibrational Spectroscopy* 32(1), 47-55 (2003)
198. S. Teh, W. Zheng, K. Ho, M. Teh, K. Yeoh and Z. Huang, "Diagnostic potential of near-infrared Raman spectroscopy in the stomach: differentiating dysplasia from normal tissue," *British Journal of Cancer* 98(2), 457-465 (2008)
199. H. Yao, Z. Tao, M. Ai, L. Peng, G. Wang, B. He and Y.-q. Li, "Raman spectroscopic analysis of apoptosis of single human gastric cancer cells," *Vibrational Spectroscopy* 50(2), 193-197 (2009)
200. B. G. Vandeginste and D. L. Massart, *Handbook of chemometrics and qualimetrics*, Elsevier Science (1998).
201. V. Baeten, "Raman spectroscopy in lipid analysis," *Lipid Technology* 22(2), 36-38 (2010)
202. B. J. Rajkumar and V. Ramakrishnan, "Infrared and laser Raman studies of l-phenylalanine l-phenylalaninium perchlorate and bis (dl-phenylalaninium) sulphate monohydrate," *Spectrochimica Acta Part A: Molecular and Biomolecular Spectroscopy* 58(9), 1923-1934 (2002)
203. H. I. Lee, M. S. Kim and S. W. Suh, "Raman spectroscopy of L-phenylalanine, L-tyrosine, and their peptides adsorbed on silver surface," *Bulletin of the Korean Chemical Society* 9(4), 218-223 (1988)
204. I. Rahman, S. K. Biswas and P. A. Kirkham, "Regulation of inflammation and redox signaling by dietary polyphenols," *Biochemical Pharmacology* 72(11), 1439-1452 (2006)

205. T. A. Koeppel, M. Trauner, J. C. Baas, J. C. Thies, S. F. Schlosser, S. Post, M. Gebhard, C. Herfarth, J. L. Boyer and G. Otto, "Extrahepatic biliary obstruction impairs microvascular perfusion and increases leukocyte adhesion in rat liver," *Hepatology* 26(5), 1085-1091 (1997)
206. J. M. Saito and J. J. Maher, "Bile duct ligation in rats induces biliary expression of cytokine-induced neutrophil chemoattractant," *Gastroenterology* 118(6), 1157-1168 (2000)
207. M. Bemelmans, D. Gouma, J. Greve and W. Buurman, "Cytokines tumor necrosis factor and interleukin‐6 in experimental biliary obstruction in mice," *Hepatology* 15(6), 1132-1136 (1992)
208. W. Zhou, W. Chao, B. A. Levine and M. S. Olson, "Role of platelet-activating factor in hepatic responses after bile duct ligation in rats," *American Journal Of Physiology* 263,G587-G587 (1992)
209. Y. Ito, N. W. Bethea, G. L. Baker, M. K. Mccuskey, R. Urbaschek and R. S. Mccuskey, "Hepatic microcirculatory dysfunction during cholestatic liver injury in rats," *Microcirculation* 10(5), 421-432 (2003)